CHALMERS
UNIVERSITY OF TECHNOLOGY

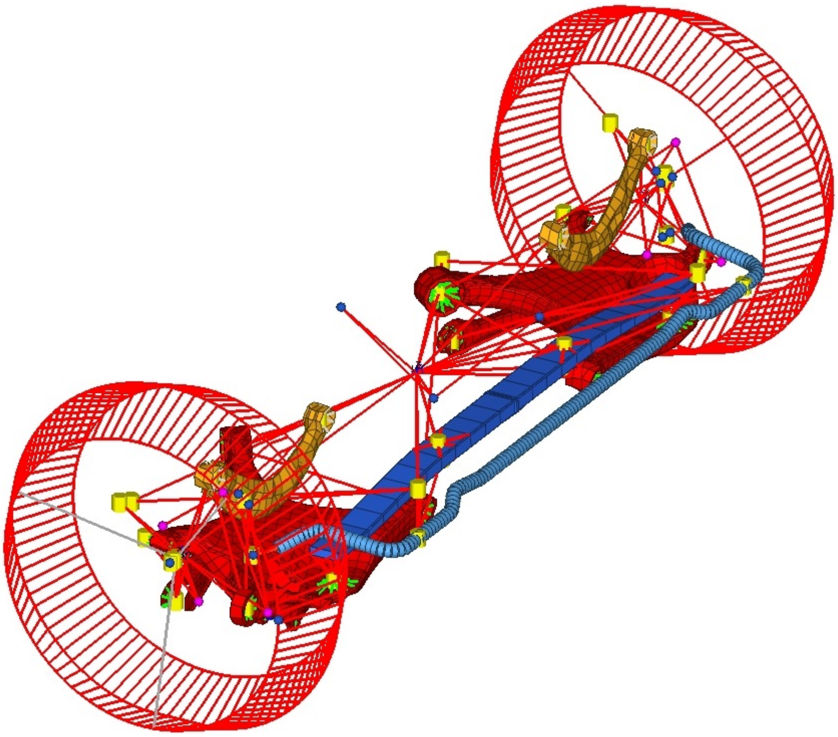

Assembly of a tire and a vehicle model to predict vibrations at the bushings

Application of a Frequency Based Substructuring method

Master's thesis in Sound and Vibration

Johan Rosholm and Michael Westers

Department of Architecture and Civil Engineering
Chalmers University of Technology
Gothenburg, Sweden 2018

Master's thesis BOMX02-17-105

Assembly of a tire and a vehicle model to predict vibrations at the bushings

Application of a Frequency Based Substructuring method

Johan Rosholm and Michael Westers

Department of Architecture and Civil Engineering
Division of Applied Acoustics
Chalmers University of Technology
Gothenburg, Sweden 2018

Assembly of a tire and a vehicle model to predict vibrations at the bushings - Application of a Frequency Based Substructuring method
JOHAN ROSHOLM and MICHAEL WESTERS

Supervisor: M.Sc. Magnus Olsson, Volvo Car Group
Supervisor: Dr. Jonathan Westlund, Volvo Car Group
Supervisor: Dr. Charles Boston, Continental AG
Supervisor: Dr. Achillefs Tsotras, Continental AG
Supervisor: Prof. Wolfgang Kropp, Chalmers University of Technology
Examiner: Prof. Wolfgang Kropp, Chalmers University of Technology

Master's Thesis BOMX02-17-105
Department of Architecture and Civil Engineering
Division of Applied Acoustics
Chalmers University of Technology
SE-412 96 Gothenburg
Telephone +46 31 772 1000

Cover: Vehicle chassis and tire model

Typeset in LaTeX
Gothenburg, Sweden 2018

Assembly of a tire and a vehicle model to predict vibrations at the bushings - Application of a Frequency Based Substructuring method

JOHAN ROSHOLM and MICHAEL WESTERS

Division of Applied Acoustics
Department of Architecture and Civil Engineering
Chalmers University of Technology

Abstract

This Master's thesis targets the prediction of vibrations at the bushings of vehicle rear chassis due to an excitation at the tire patch for early analysis in the development stage at the Volvo Car Group. In the past a hybrid model has been used, which included a FEM model of a new vehicle design proposal and through measurements obtained spindle forces of an existing tire vehicle combination. However it is reasonable that these forces are different for a new tire vehicle coupling. In this thesis the measurement data is replaced by a modal tire model, which is provided by Continental AG, to become independent of testing existing vehicles. Receptance Coupling is used to assemble one tire to the vehicle in the frequency domain. Thereby the vibration levels at a chosen bushing are obtained due to an excitation at the tire patch for seven different harmonic excitation cases. In addition, a great focus is set on the sensitivity of the coupled solution to modal truncation errors in the tire model. Therefore an error metric is developed, which assesses the similarity between two FRFs using a floating bandwidth. As a result a minimum number of modes required for a desired frequency range and excitation case is given. In a second investigation uniform distributed random noise between ± 10 percent is added to the transfer functions of the tire and the vehicle model. The results show a deviation up to around 5 dB above the non-polluted case, for the major part of the frequency range, for some frequencies the coupled result show a greater sensitivity with deviation up to 20 dB for certain noise matrices.

Keywords: Dynamic Substructuring, Frequency Based Substructuring, Tire, Receptance Coupling Method, Generalized Receptance Coupling Method

Acknowledgements

We want to express our warmest thanks for the greatful help from the Technical Acoustic department at Chalmers and especially to our mentor Wolfgang Kropp having been on our side along this project and also along the whole Master's programme. Also special thanks is given to Magnus Olsson and Jonathan Westlund, who have been supervising this project by the Volvo Car Group. We also appreciate the great help from Charles Boston and Achillefs Tsotras as discussion partners having answered many questions regarding the provided tire model. Lastly also thanks to all other people we had discussions with on the topic and also for the friendliness from the staff from all sides.

Johan Rosholm and Michael Westers   Gothenburg, February 2018

Contents

Nomenclature **xiii**

List of Figures **xv**

List of Tables **xvii**

1 Introduction **1**
1.1 Background 1
1.2 Problem description 1
1.3 Objective and scope 2
1.4 Outline 2

2 Theory **5**
2.1 Calculations of Frequency Response Functions 5
2.2 Substructure synthesis methods 7
2.2.1 Overview 8
2.2.2 Impedance Coupling for two substructures 10
2.2.3 Receptance Coupling for two substructures 13
2.2.4 Generalized Receptance Coupling for several substructures . . 16

3 Coupling of simple beam models **21**
3.1 Method 21
3.2 Results and discussion 22

4 Coupling of tire and chassis model **23**
4.1 Method 23
4.1.1 Chassis model 23
4.1.2 Tire model 25
4.2 Results and discussion 27

5 Sensitivity study on coupled solution **29**
5.1 Modal truncation errors introduced into tire model 29
5.1.1 Method 30
5.1.2 Results and discussion 36
5.2 Random noise introduced to tire and chassis model 41
5.2.1 Method 42
5.2.2 Results and discussion 42

6 Conclusion **47**

7 Suggestions of future studies **49**

Bibliography **49**

A Prediction of vibrations at the bushing - Reference **I**

B Sensitivity study - Modal truncation error introduced in the tire model **IX**

C Sensitivity study - Random noise **XVII**

Nomenclature

Abbreviation

DOF, DOFs	Degree of Freedom, Degrees of Freedom
FRF	Frequency Response Function
FBS	Frequency Based Substructuring
CMS	Component Mode Synthesis
NVH	Noise Vibration Harshness
LM FBS	Lagrange Multiplier Frequency Based Substructuring Method
FEM	Finite Element Method
GRC	Generalized Receptance Coupling
CAE	Computer Aided Engineering
SDOF	Single Degree of Freedom

Variables

$\mathbf{F}$	Vector of external forces and moments
$\mathbf{Y}$	Mobility matrix
$\mathbf{Z}$	Mechanical impedance matrix
$\mathbf{x}$,$\mathbf{v}$,$\mathbf{a}$	Vector of DOFs regarding displacement, velocity and acceleration
$\mathbf{M}$	Mass matrix
$\mathbf{C}$	Damping matrix
$\mathbf{K}$	Stiffness matrix
j	Complex unit, $j = \sqrt{-1}$
t	Time
f	Frequency
ω	Angular frequency
n	Number of DOFs
N	Number of modes included in the tire model

Subscript and superscript

A,...,D	Subsystem of tire A, B, C, D respectively
E	Subsystem vehicle E
*	Coupled system
a,...,e	Internal DOFs of subsystem A, B, C, D, E respectively
α	Sets of internal DOFs of the subsystems
γ	Sets of interface DOFs of the subsystems
j,...,m	Interface DOFs at the intersections J,...,M

List of Figures

2.1 Modal summation 7
2.2 Domains of Dynamic Substructuring [17] 9
2.3 Frequency Based Substructuring methods overview 10
2.4 Subsystems A and E to be coupled in a node with one DOF 10
2.5 Subsystems A and E to be coupled in a node with six DOFs 12
2.6 Five subsystems to be coupled at four different points. 17

3.1 Three subsystems coupled in Hypermesh 22
3.2 Transfer function from point 5 to point 307 related to fig. 3.1 22

4.1 Simple chassis model with the chosen spindle and bushing position . . 23
4.2 Mobility spindle to bushing, translational DOFs, 1st harmonic, uncoupled vehicle 24
4.3 Mobility spindle to bushing, rotational DOFs, 1st harmonic, uncoupled vehicle 24
4.4 Harmonic excitation cases, speed-frequency dependence. 25
4.5 Coordinate system of tire and the vehicle model, top view. 26
4.6 Translational response at rim due to excitation at tire patch, 1st harmonic, uncoupled tire 26
4.7 Rotational response at rim due to excitation at tire patch, 1st harmonic, uncoupled tire 27
4.8 Translational response at the bushing due to excitation at the tire patch, 1st harmonic 28
4.9 Rotational response at the bushing due to excitation at the tire patch, 1st harmonic 28

5.1 Mismatch of power related power of reference response function. . . . 32
5.2 Floating frequency bands. 32
5.3 Error map for response at the bushing in z direction, 5th harmonic . 34
5.4 Response in z direction at the bushing for different modes included, 5th harmonic 35
5.5 Error in z direction at the bushing for different modes included, 5th harmonic 35
5.6 Maximum truncation error in $\mathbf{v}^*_{ea}$ for different harmonics. 38
5.7 Truncation error for z DOF in $\mathbf{v}^*_{ea}$ for different harmonics 39
5.8 Belonging eigenfrequencies to number of modes. 40
5.9 Scatter band for noise in tire and vehicle model between 0 and ±10 % 43

5.10 Possible prediction inside scatter band caused by frequency independent scaled FRFs and response functions 44
5.11 Possible prediction inside scatter band caused by frequency dependent scaled FRFs and response functions 45

A.1 Translational response at the bushing, 1st harmonic I
A.2 Rotational response at the bushing, 1st harmonic II
A.3 Translational response at the bushing, 2nd harmonic II
A.4 Rotational response at the bushing, 2nd harmonic III
A.5 Translational response at the bushing, 3rd harmonic III
A.6 Rotational response at the bushing, 3rd harmonic IV
A.7 Translational response at the bushing, 4th harmonic IV
A.8 Rotational response at the bushing, 4th harmonic V
A.9 Translational response at the bushing, 5th harmonic V
A.10 Rotational response at the bushing, 5th harmonic VI
A.11 Translational response at the bushing, 6th harmonic VI
A.12 Rotational response at the bushing, 6th harmonic VII
A.13 Translational response at the bushing, 7th harmonic VII
A.14 Rotational response at the bushing, 7th harmonic VIII

B.1 Response in z direction at the bushing for different modes included, 1st harmonic IX
B.2 Response in z direction at the bushing for different modes included, 2nd harmonic X
B.3 Response in z direction at the bushing for different modes included, 3rd harmonic X
B.4 Response in z direction at the bushing for different modes included, 4th harmonic XI
B.5 Response in z direction at the bushing for different modes included, 5th harmonic XI
B.6 Response in z direction at the bushing for different modes included, 6th harmonic XII
B.7 Response in z direction at the bushing for different modes included, 7th harmonic XII
B.8 Truncation error for z DOF in $\mathbf{v}^{*}_{\mathrm{ea}}$ XIII
B.9 Maximum truncation error in $\mathbf{Y}^{\mathrm{A}}_{\mathrm{ja}}\mathbf{F}^{\mathrm{A}}_{\mathrm{a}}$, tire uncoupled XIV
B.10 Maximum truncation error in $\mathbf{Y}^{\mathrm{A}}_{\mathrm{jj}}$, tire uncoupled XV

C.1 Response in z direciton at the bushing, 4th harmonic, noise introduced to tire model, 2000 calculation rounds. XVII
C.2 Response in z direction at the bushing, 4th harmonic, noise introduce to chassis model, 2000 calculations rounds. XVII

List of Tables

2.1 Definition and names of FRFs and inverse FRFs 6

5.1 Suggested number of modes for different excitation cases. 41

1
Introduction

1.1 Background

Exposure to noise can affect a humans task performance [9] [12]. When the task is to drive a car it is of interest to control the noise levels inside the car cabin for safety reasons. Furthermore, decreased noise levels are linked to a higher quality perception of the car [16]. Road noise is one important load case, which might be a keen interest for the design of electric cars, in which the combustion engine as a sound source is not present anymore. There are several road noise generation mechanism but in this thesis structure borne introduced noise at the tire patch will be investigated. Thereby the tire is excited by the surface roughness of the road. These vibrations are transmitted from the tire through the rim to the wheel suspension and from there to surface areas inside the car cabin. Finally, vibrations in these areas lead to sound radiation inside the car. In order to optimize the whole structure regarding the Noise Vibration and Harshness (NVH) attributes in the early stage of development, predictions needs to be performed.

1.2 Problem description

Currently, the development of a new car chassis at the Volvo Car Group depends on tests of an existing vehicle and tires. Since prototypes are only available in the late stage of the development the following approach has been chosen in the past to give preliminary estimations. Hereby the through measurements obtained spindle forces[1] of a existing vehicle tire configuration is set as a load for the optimization of the new car chassis proposal. However the spindle forces are very likely to be different when a new chassis instead of a previous version of the chassis is connected to the tires. Another drawback is that the tire manufacture is designing the tires independently of the new design approach of the car manufacture. At the time when the vehicle prototypes exist, very little time is left to adjust the tire design to the new vehicle generation.

[1]Accelerations are measured at different points next to the spindle. Knowing the FRFs from a CAE model allows to calculate the forces, which have caused these vibrations [6].

1.3 Objective and scope

From the initial problem defined in section 1.2 the overall goal is set to replace the measurement data with a tire model provided by tire manufacturers. This allows the optimization of the assembly consisting of both a new tire and a new chassis, in a joint project by the tire and vehicle manufacturer. This might increase the accuracy of the prediction and finally give a better understanding of the tire - vehicle interaction in the long run.

In this Master's thesis a modal tire model, provided from Continental AG, will be coupled to the rear vehicle chassis provided by the Volvo Car Group, in order to predict the vibrations at the chassis' bushing due to an artificial excitation at the tire with seven different harmonics. For the assembly of the tire and the vehicle model the rim is not considered as a own subsystem but its mass and inertia is taken into account. The rim is assumed to be infinite stiff. The hub of the wheel suspension will be the one and only coupling point, which allows three translational and three rotational degrees of freedom (DOFs). Since the subsystem data from both Volvo Car Group and Continental AG is provided in the frequency domain, a coupling method in the same domain shall be used. Final coupling results will be focused to one case scenario in where only one tire is coupled to the rear chassis and the response is evaluated at a single chosen bushing node.

Apart from predicting the coupled solution of the tire vehicle combination the second objective is to test the performed predictions regarding truncation errors in the modal tire model. The higher order modes in the tire model are very difficult to accurately predict. By excluding them step by step in the modal summation solution and looking at the coupled results in the frequency range up to 160 Hz[2], conclusions can be made whether or not certain higher order modes[3] are important for that defined frequency range. These results are very meaningful for the tire engineers, since they know if they need to spend more time on increasing the accuracy of higher order modes or not.

The last goal is to investigate how errors introduced in the frequency response functions of the subsystems tire and chassis affect the coupled solution.

1.4 Outline

This thesis is structured as follows. After this chapter an introduction to the description of dynamic systems is given. The next part deals with how dynamic subsystems can be coupled in the frequency domain to obtain a description of the synthesized system. This theory is then applied to a test case in which three beams are coupled.

[2]Limit of the tire model due to course discretization inter alia

[3]Modes that have their eigenfrequency outside the target frequency range from 0 Hz to 160 Hz

The coupling is made with both the software Hypermesh solved for the direct solution with the solver Optistruct and also in a developed Matlab script. In this way the developed coupling script is validated. Moving on to the tire - vehicle case, the provided data for the tire model and the vehicle model are explained. From coupling these systems results are obtained and discussed in the next step. In addition, the sensitivity of modal truncation errors introduced into the tire model is discussed for the coupled solution. Further more, errors in the individual subsystems are investigated by scaling all elements of the FRF matrices with random noise. Lastly an overall conclusion is drawn and recommendations for future investigations are given.

2

Theory

2.1 Calculations of Frequency Response Functions

Two approaches will be presented in order to calculate FRFs. One in which the Fourier transform is used and another in which FRFs are synthesized with the modal approach.

In order to model the dynamic behaviour of a system, a given structure can be separated into its mass, stiffness and damping properties. The information about the distribution of these can be stored in mass $\mathbf{M}$, damping $\mathbf{C}$ and stiffness matrices $\mathbf{K}$ [10].

The equation of motion is:

$$\mathbf{M}\ddot{\mathbf{x}}(t) + \mathbf{C}\dot{\mathbf{x}}(t) + \mathbf{K}\mathbf{x}(t) = \mathbf{F}(t) \tag{2.1}$$

where $\mathbf{x}(t), \dot{\mathbf{x}}(t), \ddot{\mathbf{x}}(t)$ are the displacement, velocity and acceleration vectors respectively in dependency of the time, t. The time depending excitation is introduced with $\mathbf{F}(t)$.

The latter equation can be transformed to the frequency domain using the Fourier transform [10]:

$$(-\omega^2\mathbf{M} + j\omega\mathbf{C} + \mathbf{K})\mathbf{x}(\omega) = \mathbf{F}(\omega) \tag{2.2}$$

with the angular frequency, $\omega = 2\pi f$. Equation (2.2) can be expressed in terms of velocity:

$$\left(j\omega\mathbf{M} + \mathbf{C} + \frac{1}{j\omega}\mathbf{K}\right)\mathbf{v}(\omega) = \mathbf{F}(\omega) \tag{2.3}$$

The mechanic impedance is:

$$\mathbf{Z}(\omega) = j\omega\mathbf{M} + \mathbf{C} + \frac{1}{j\omega}\mathbf{K} \tag{2.4}$$

The inverse of the mechanical impedance matrix $\mathbf{Z}(\omega)$ is called the mobility matrix $\mathbf{Y}(\omega)$ and is an FRF, which relates the output (velocity) to the input (force). The definition and names of other FRFs and inverse FRFs are explained in table 2.1 according to [11].

$$\mathbf{Y}(\omega) = \mathbf{Z}(\omega)^{-1} = (j\omega\mathbf{M} + \mathbf{C} + \frac{1}{j\omega}\mathbf{K})^{-1} \tag{2.5}$$

The mobility can be used to calculate the system response due to an excitation:

$$\mathbf{Y}(\omega)\mathbf{F}(\omega) = \mathbf{v}(\omega) \tag{2.6}$$

Table 2.1: Definition and names of FRFs and inverse FRFs

	Dimension		Name
	Displacement / force	$\alpha(\omega) = \frac{x(\omega)}{F(\omega)}$	Compliance, receptance
FRF	Velocity / force	$Y(\omega) = \frac{v(\omega)}{F(\omega)}$	Mobility
	Acceleration /force	$A(\omega) = \frac{a(\omega)}{F(\omega)}$	Accelerance, inertance
Inverse	Force / Displacement	$\frac{1}{\alpha(\omega)} = \frac{F(\omega)}{x(\omega)}$	Dynamic stiffness
FRF	Force / velocity	$Z(\omega) = \frac{F(\omega)}{v(\omega)}$	Mechanical impedance
	Force / acceleration	$\frac{1}{A(\omega)} = \frac{F(\omega)}{a(\omega)}$	Dynamic mass, apparent mass

However the matrix inversion of the impedance in eq. (2.5) can lead to heavy and time consuming calculations, especially if many DOFs and frequencies are taken into account [8]. A more computationally efficient way of calculating FRFs is to perform an eigenvalue analysis, in which the natural frequencies, mode shapes and modal damping are obtained. The FRF between two DOFs q and r can be synthesized for a proportionally and structurally damped system with:

$$Y_{\mathrm{qr}}(\omega) = j\omega \sum_{i=1}^{N} \frac{\Psi_{\mathrm{q(i)}}\Psi_{\mathrm{r(i)}}}{-\omega^2 + j\eta_{\mathrm{i}}\omega_{0\mathrm{(i)}}^2 + \omega_{0\mathrm{(i)}}^2} \tag{2.7}$$

which can be seen as a superposition of N numbers of Single Degree of Freedom (SDOF) systems. An individual SDOF system with the index i has its own loss factor and a natural angular frequency named as η_{i} and $\omega_{0\mathrm{(i)}}$ respectively. Finally the numerator is called modal amplitude and is determined by $\Psi_{\mathrm{q(i)}}$ and $\Psi_{\mathrm{r(i)}}$, which correspond to the DOFs q and r respectively in the mass normalized eigenvector of the i^{th} mode [11]. In fig. 2.1 the real and imaginary part of a FRF is synthesized with three FRFs of SDOF systems, having the eigenfrequencies 30 Hz, 75 Hz and 225 Hz. It can be seen, that the third SDOF system has very little influence on the calculation of the modal summation solution in the frequency range near the first two natural frequencies. In addition it can be mentioned that the real part is positive at and nearby the first two resonances and negative around the third resonance due to the fact that positive and negative modal amplitudes have been used respectively to generate the SDOF FRFs.

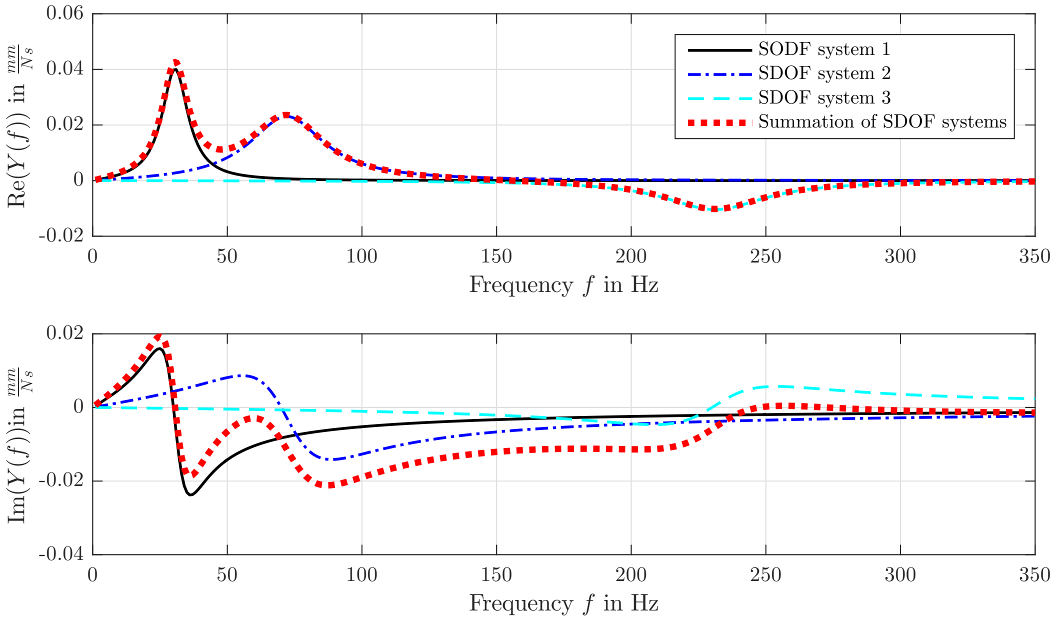

Figure 2.1: Modal summation

From now on the transfer function, force and response variables $\mathbf{Y}(\omega)$,$\mathbf{F}(\omega)$ and $\mathbf{v}(\omega)$ will be in written as $\mathbf{Y}$,$\mathbf{F}$ and $\mathbf{v}$. Thereby it is assumed, that they are dependent on the angular frequency.

2.2 Substructure synthesis methods

After getting familiar with the description of a dynamic system in terms of FRFs the question arises how several subsystems, that are connected to each other, can be assembled to one structure. In the first part of this section a brief overview about different coupling techniques is given, underlining advantages and disadvantages. In the next step the chosen methods used in this thesis are explained. This includes the Impedance Coupling Method and the Receptance Coupling Method for two substructures. Although this thesis aims to couple one tire to the rear chassis the Generalized Receptance Coupling Method is also explained, which gives a formulation for coupling several substructures. This might get important for the assembly of two or four wheels to the vehicle.

2.2.1 Overview

The methods for coupling structures can be divided in three main categories with respect to the domain in which they accomplished: These are the physical domain, the frequency domain and the modal domain. This can be seen in fig. 2.2 as well as how to switch between different domains. For instance Fourier analysis is used to transform from the physical domain to the frequency domain. All approaches are based on equilibrium condition and compatibility condition in the coupling point. Thus, all methods yield the same result, if the input information is equivalent. The solution is unique, however different results can be obtained when computation errors take place, such as rounding errors [19]. The dynamic substructuring methods can be used with analytically and experimental data origin. When using experimental data it is called experimental substructuring. Depending on which data origin is used different methods do have certain benefits.

In the first category the coupling is made in the time domain with physical quantities such as mass, stiffness and damping. This technique is called Direct Coupling and is used in standard FE-modelling [22]. However it is usually not used in experimental substructuring, since it is unfeasible to measure directly the mass, stiffness and damping properties of the substructure elements [17].

Methods that belong to the second category are known as modal coupling techniques or Component Mode Synthesis (CMS). Here a limited number of modes is used to approximate the system behaviour. Since the number of physical coordinates is reduced to a smaller amount of generalized coordinates, the calculation time is hereby reduced. The results can be different from the other methods, when too few modes are taken into account. This error is then called modal truncation error. If all modes are included in the modelling no truncation error is expected. In order to apply this method to experimental FRF data, the modal parameters needs to be determined by a curve fitting algorithm[1]. Thereby the quality of information about the system can be increased or decreased. On the one hand the contribution of spiky measurement noise on top of the FRFs can be reduced through the modal parameter estimation, which results in smooth curves [21]. On the other hand the measurements can contain certain non-linear behaviour of the structure, that is not captured or misinterpreted through the modal parameter identification [10]. One drawback in experimental substructuring with CMS is that modal truncation error can not be avoided. To represent a certain frequency range of a dynamic system with modal parameters, the contribution of modes, that are outside that considered frequency range, need to be known. This means in practise that the measurement frequency range is higher than the frequency range of interest to reduce the effect of modal truncation. Not minding which data origin is used, a clear advantage of CMS should be pointed out. The eigenvectors of the coupled system are know directly after the coupling process and can be used to visualize the mode shapes of the coupled structure.

[1]The mathematical unknowns of a mathematical description of a structure are obtained by fitting the mathematical model to the measurement data in a way that they match the best.

An assembly in the frequency domain is called Frequency Based Substructuring (FBS). Here FRFs are used as input. Since at least one matrix inversion is needed for this coupling method, Urgueira [21] analyses the circumstance with this technique that linear dependencies and near linear dependencies can make the inversion fail. This problem can occur due to acquiring subsystem-FRFs from an inadequate modal data with e.g. more coordinates than modes which can make the matrix singular and the inversion would fail although a solution exists. The problem can also occur if FRF data have been measured on locally rigid points causing a linear dependency for some of the responses due to "redundant coordinates" [21]. Due to this fact, the method is "not a mathematical generalized one" according to reference [19]. Another drawback of using FBS is that the mode shapes of the coupled structure are not known directly. However there is the possibility to transform the FRF data back to the modal domain through modal parameter identification (see fig. 2.2). When using noise polluted experimental FRF as input, the coupled solution can show unwanted pseudo resonances, which are caused by amplified measurement noise peaks. This happens when the inverted matrix is ill conditioned [21].

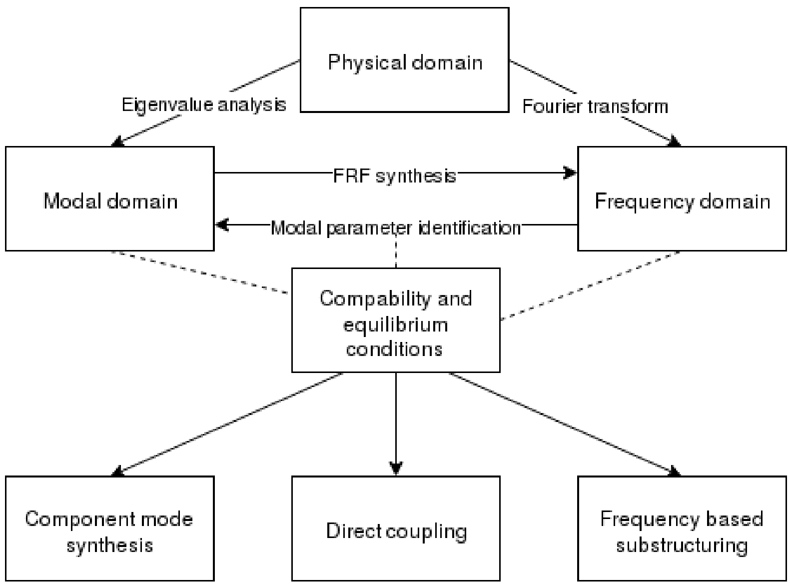

Figure 2.2: Domains of Dynamic Substructuring [17]

Since the data of the tire and the vehicle is provided as FRF data, the direct and uncomplicated way of applying FBS techniques is chosen. The assembly in the frequency domain can be accomplished by either coupling FRF data (receptance, mobility etc.) or inverse FRF data (dynamic stiffness, impedance etc.), which can be seen in fig. 2.3. In literature the terms Receptance Coupling and Impedance Coupling[2] are mainly used. The first approach has gained more popularity and has been reformulated and improved over time since it is computationally more efficient and is more robust against ill conditioning due to less and smaller matrices which

[2]Dynamic Stiffness Coupling and Impedance Coupling use basically the same coupling equation. The only difference is that stiffness instead of impedance matrices are used.

are inverted[3]. There is a formulation of the Receptance Coupling method for two structures for instance in [11]. Another is Jetmundsens formulation of the so called Gereralized Receptance Coupling (GRC), in reference [13]. The GRC technique uses graph theory to assemble several substructures. A well known reformulation of the dual assembly is the Lagrange Multiplier Frequency Based Substructuring Method (LM FBS) presented in reference [10]. The Impedance Coupling is explained for two substructures in reference [11], but Jetmundsens method can also be used to couple several substructures with inverse FRFs [18].

Frequency Based Substructuring

- Using FRFs (e.g. Receptance Coupling)
  - two subsystem [11]
  - several subsystems [13], [10]
- Using inverse FRFs (e.g. Impedance Coupling)
  - two subsystems[11]
  - several subsystems [18]

Figure 2.3: Frequency Based Substructuring methods overview

2.2.2 Impedance Coupling for two substructures

In order to explain the concept of Impedance Coupling a simple case is considered in the following. There are two subsystems A and E that shall be coupled. First it is assumed that each subsystem have only one DOF (see fig. 2.4). Thus the one and only DOF of A will be coupled to the DOF of E.

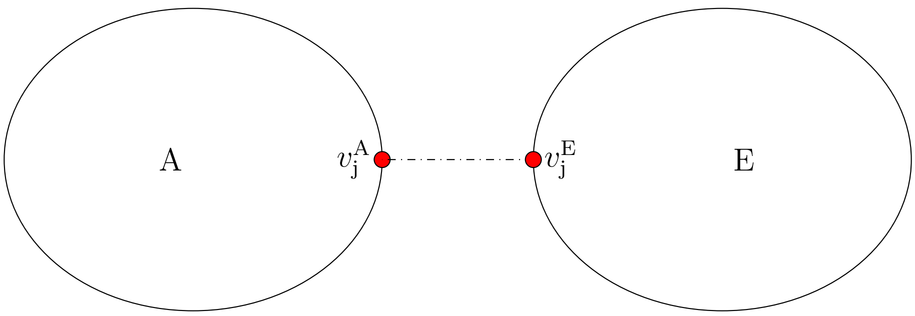

Figure 2.4: Subsystems A and E to be coupled in a node with one DOF

The response of a linear and time invariant system A and E can be calculated if the excitation and the mobility is known [11]:

$$v_{\mathrm{j}}^{\mathrm{A}} = Y_{\mathrm{jj}}^{\mathrm{A}} F_j^{\mathrm{A}} \qquad v_j^{\mathrm{E}} = Y_{\mathrm{jj}}^{\mathrm{E}} F_{\mathrm{j}}^{\mathrm{E}} \tag{2.8}$$

[3]Simulation and measurements are usually obtained as FRF data

In the coupling point the following two condition must be fullfilled with respect to the forces and velocities in the subsystems (superscript A and E) and in the coupled system (superscript *):

$$v_{\mathrm{j}}^{*} = v_{\mathrm{j}}^{\mathrm{A}} = v_{\mathrm{j}}^{\mathrm{E}} \qquad \text{(compatibility)} \tag{2.9}$$

$$F_{\mathrm{j}}^{*} = F_{\mathrm{j}}^{\mathrm{A}} + F_{\mathrm{j}}^{\mathrm{E}} \qquad \text{(equilibrium)} \tag{2.10}$$

From eq. (2.9) and eq. (2.10) the following relation can be composed:

$$\frac{1}{Y_{\mathrm{jj}}^{*}} = \frac{1}{Y_{\mathrm{jj}}^{\mathrm{A}}} + \frac{1}{Y_{\mathrm{jj}}^{\mathrm{E}}} \tag{2.11}$$

Expressing this in terms of the mechanical impedance gives:

$$Z_{\mathrm{jj}}^{*} = Z_{\mathrm{jj}}^{\mathrm{A}} + Z_{\mathrm{jj}}^{\mathrm{E}} \tag{2.12}$$

The mobility of the coupled system is then:

$$Y_{\mathrm{jj}}^{*} = \left[(Y_{\mathrm{jj}}^{\mathrm{A}})^{-1} + (Y_{\mathrm{jj}}^{\mathrm{E}})^{-1}\right]^{-1} \tag{2.13}$$

From eq. (2.13) it can be seen that for this case three inverse matrices need to be calculated [11].

The theory will be extended now to a more general case allowing three translational (x, y, z) and three rotational DOFs (α, β, γ) [5]. The matrix equation system between node 1 and 2 becomes:

$$\mathbf{v}_2 = \mathbf{Y}_{21}\mathbf{F}_1 \tag{2.14}$$

This means in detail:

$$\begin{bmatrix} v_{\mathrm{x}} \\ v_{\mathrm{y}} \\ v_{\mathrm{z}} \\ v_{\alpha} \\ v_{\beta} \\ v_{\gamma} \end{bmatrix} = \begin{bmatrix} Y_{\mathrm{xx}} & Y_{\mathrm{xy}} & Y_{\mathrm{xz}} & Y_{\mathrm{x}\alpha} & Y_{\mathrm{x}\beta} & Y_{\mathrm{x}\gamma} \\ Y_{\mathrm{yx}} & Y_{\mathrm{yy}} & Y_{\mathrm{yz}} & Y_{\mathrm{y}\alpha} & Y_{\mathrm{y}\beta} & Y_{\mathrm{y}\gamma} \\ Y_{\mathrm{zx}} & Y_{\mathrm{zy}} & Y_{\mathrm{zz}} & Y_{\mathrm{z}\alpha} & Y_{\mathrm{z}\beta} & Y_{\mathrm{z}\gamma} \\ Y_{\alpha\mathrm{x}} & Y_{\alpha\mathrm{y}} & Y_{\alpha\mathrm{z}} & Y_{\alpha\alpha} & Y_{\alpha\beta} & Y_{\alpha\gamma} \\ Y_{\beta\mathrm{x}} & Y_{\beta\mathrm{y}} & Y_{\beta\mathrm{z}} & Y_{\beta\alpha} & Y_{\beta\beta} & Y_{\beta\gamma} \\ Y_{\gamma\mathrm{x}} & Y_{\gamma\mathrm{y}} & Y_{\gamma\mathrm{z}} & Y_{\gamma\alpha} & Y_{\gamma\beta} & Y_{\gamma\gamma} \end{bmatrix} \cdot \begin{bmatrix} F_{\mathrm{x}} \\ F_{\mathrm{y}} \\ F_{\mathrm{z}} \\ M_{\alpha} \\ M_{\beta} \\ M_{\gamma} \end{bmatrix} \tag{2.15}$$

A total system can be described by several FRFs between different nodes and by so called driving point functions. The latter one represent the special case in which excitation and response is evaluated at the same node. Thus the size of total transfer function matix, which includes the mobility from N nodes to each other will be a 6N x 6N matrix assuming 6 DOFs per node.

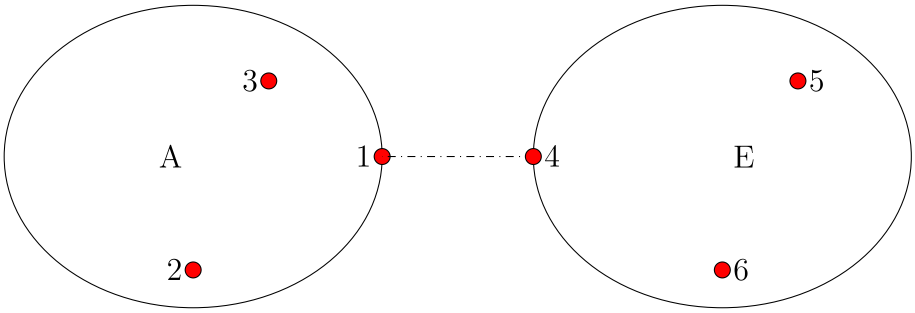

Figure 2.5: Subsystems A and E to be coupled in a node with six DOFs

The mobility matrix of subsystem A and E in fig. 2.5 can be partitioned with respect to internal DOFs a and e respectively and coupling DOFs j for each subsystem [11]:

$$\mathbf{Y}^{\mathrm{A}} = \left[\begin{array}{c|c} \mathbf{Y}^{\mathrm{A}}_{\mathrm{aa}} & \mathbf{Y}^{\mathrm{A}}_{\mathrm{aj}} \\ \hline \mathbf{Y}^{\mathrm{A}}_{\mathrm{ja}} & \mathbf{Y}^{\mathrm{A}}_{\mathrm{jj}} \end{array}\right] \qquad \mathbf{Y}^{\mathrm{E}} = \left[\begin{array}{c|c} \mathbf{Y}^{\mathrm{E}}_{\mathrm{ee}} & \mathbf{Y}^{\mathrm{E}}_{\mathrm{ej}} \\ \hline \mathbf{Y}^{\mathrm{E}}_{\mathrm{je}} & \mathbf{Y}^{\mathrm{E}}_{\mathrm{jj}} \end{array}\right] \tag{2.16}$$

In fig. 2.5 subsystem A has the interal DOFs of node 2 and node 3 and the coupling DOFs of node 1:

$$\mathbf{Y}^{\mathrm{A}} = \begin{bmatrix} \mathbf{Y}_{11} & \mathbf{Y}_{12} & \mathbf{Y}_{13} \\ \mathbf{Y}_{21} & \mathbf{Y}_{22} & \mathbf{Y}_{23} \\ \mathbf{Y}_{31} & \mathbf{Y}_{32} & \mathbf{Y}_{33} \end{bmatrix} \quad \text{partioned to} \quad \mathbf{Y}^{\mathrm{A}} = \left[\begin{array}{cc|c} \mathbf{Y}_{22} & \mathbf{Y}_{23} & \mathbf{Y}_{21} \\ \mathbf{Y}_{32} & \mathbf{Y}_{33} & \mathbf{Y}_{31} \\ \hline \mathbf{Y}_{12} & \mathbf{Y}_{13} & \mathbf{Y}_{11} \end{array}\right] \tag{2.17}$$

After partitioning the mobility matrix, two matrix inversions are required to transform from mobility to the impedance for the subsystems A and E[4]. The size of the matrix being inverted is determined by the number of DOFs in the mobility matrix of the subsystems called n^{A} and n^{E} respectively. How many internal DOFs (e.g. a and e) are taken into account is up to the user and it is not required to include all DOFs of the whole substructure model. However the coupling results can only be obtained for those DOFs that are included in the mobility matrix of the subsystem. Regarding the coupling DOFs j it should be mentioned that all of them needs to be taken into account to correctly represent the coupling properties.

$$\mathbf{Z}^{\mathrm{A}} = \left[\begin{array}{c|c} \mathbf{Z}^{\mathrm{A}}_{\mathrm{aa}} & \mathbf{Z}^{\mathrm{A}}_{\mathrm{aj}} \\ \hline \mathbf{Z}^{\mathrm{A}}_{\mathrm{ja}} & \mathbf{Z}^{\mathrm{A}}_{\mathrm{jj}} \end{array}\right] = (\mathbf{Y}^{\mathrm{A}})^{-1} = \left[\begin{array}{c|c} \mathbf{Y}^{\mathrm{A}}_{\mathrm{aa}} & \mathbf{Y}^{\mathrm{A}}_{\mathrm{aj}} \\ \hline \mathbf{Y}^{\mathrm{A}}_{\mathrm{ja}} & \mathbf{Y}^{\mathrm{A}}_{\mathrm{jj}} \end{array}\right]^{-1}_{n^{\mathrm{A}}\ \mathrm{x}\ n^{\mathrm{A}}} \tag{2.18}$$

By adding up the impedances in the coupling point, the mobility of the coupled system is then according to [5]:

$$\mathbf{Y}^{*} = \begin{bmatrix} \mathbf{Y}^{*}_{\mathrm{aa}} & \mathbf{Y}^{*}_{\mathrm{aj}} & \mathbf{Y}^{*}_{\mathrm{ae}} \\ \mathbf{Y}^{*}_{\mathrm{ja}} & \mathbf{Y}^{*}_{\mathrm{jj}} & \mathbf{Y}^{*}_{\mathrm{je}} \\ \mathbf{Y}^{*}_{\mathrm{ea}} & \mathbf{Y}^{*}_{\mathrm{ej}} & \mathbf{Y}^{*}_{\mathrm{ee}} \end{bmatrix} = \begin{bmatrix} \mathbf{Z}^{\mathrm{A}}_{\mathrm{aa}} & \mathbf{Z}^{\mathrm{A}}_{\mathrm{aj}} & 0 \\ \mathbf{Z}^{\mathrm{A}}_{\mathrm{ja}} & \mathbf{Z}^{\mathrm{A}}_{\mathrm{jj}} + \mathbf{Z}^{\mathrm{E}}_{\mathrm{jj}} & \mathbf{Z}^{\mathrm{E}}_{\mathrm{je}} \\ 0 & \mathbf{Z}^{\mathrm{E}}_{\mathrm{ej}} & \mathbf{Z}^{\mathrm{E}}_{\mathrm{ee}} \end{bmatrix}^{-1}_{n^{*}\ \mathrm{x}\ n^{*}} \tag{2.19}$$

[4] measurement data and predictions are usually obtained as FRF data

It can be seen, that the Impedance Coupling requires a third matrix inversion of the size $n^* = n^\mathrm{A} + n^\mathrm{E} - n^\mathrm{j}$, where n^j is the number of coupling DOFs between the two structures [4]. It should be mentioned that in eq. (2.19) the coupled mobilities are stored in $\mathbf{Y}^*$ in the order of the DOFs a, j, e. Ewins [11] uses a formulation in the order a, e, j which means that the inverted impedance matrix looks different from the one in eq. (2.19).

Calculation of the inverse of a matrix

In this section the calculation of the matrix inversion will be described briefly, in order to understand, how errors in the subsystems are spread into the whole system through the matrix inversion. Therefore a 2x2 matrix named as **A** is considered:

$$\mathbf{A} = \begin{bmatrix} a_{11} & a_{12} \\ a_{21} & a_{22} \end{bmatrix} \tag{2.20}$$

The resulting inverse is calculated as:

$$\mathbf{A}^{-1} = \frac{\mathrm{adj}(\mathbf{A})}{\det(\mathbf{A})} \tag{2.21}$$

The determinant of **A** is calculated as:

$$\det(A) = a_{11} \cdot a_{22} - a_{21} \cdot a_{12} \tag{2.22}$$

and the adjoint of A is:

$$\mathrm{adj}(\mathbf{A}) = \begin{bmatrix} a_{22} & -a_{21} \\ -a_{21} & a_{11} \end{bmatrix} \tag{2.23}$$

It can be seen, that if only one element in **A** is incorrect all elements in the inverted matrix will be affected.

2.2.3 Receptance Coupling for two substructures

In the following a method will be presented which needs only one matrix inversion. To be consistent to the previous chapter mobility instead of receptance FRFs are used. The description and derivation is equivalent but the response data is the velocity instead of the displacement.

Derivation Receptance Coupling

The derivation is oriented towards Scheel's work in reference [20]. The velocity vector, the mobility matrix and the force vector of the subsystems A and E can be partitioned with respect to internal and coupling coordinates as explained in section 2.2.2:

$$\begin{bmatrix}\mathbf{v}^{\mathrm{A}}_{\mathrm{a}}\\ \mathbf{v}^{\mathrm{A}}_{\mathrm{j}}\end{bmatrix} = \begin{bmatrix}\mathbf{Y}^{\mathrm{A}}_{\mathrm{aa}} & \mathbf{Y}^{\mathrm{A}}_{\mathrm{aj}}\\ \mathbf{Y}^{\mathrm{A}}_{\mathrm{ja}} & \mathbf{Y}^{\mathrm{A}}_{\mathrm{jj}}\end{bmatrix}\begin{bmatrix}\mathbf{F}^{\mathrm{A}}_{\mathrm{a}}\\ \mathbf{F}^{\mathrm{A}}_{\mathrm{j}}\end{bmatrix} \qquad \begin{bmatrix}\mathbf{v}^{\mathrm{E}}_{\mathrm{e}}\\ \mathbf{v}^{\mathrm{E}}_{\mathrm{j}}\end{bmatrix} = \begin{bmatrix}\mathbf{Y}^{\mathrm{E}}_{\mathrm{ee}} & \mathbf{Y}^{\mathrm{E}}_{\mathrm{ej}}\\ \mathbf{Y}^{\mathrm{E}}_{\mathrm{je}} & \mathbf{Y}^{\mathrm{E}}_{\mathrm{jj}}\end{bmatrix}\begin{bmatrix}\mathbf{F}^{\mathrm{E}}_{\mathrm{e}}\\ \mathbf{F}^{\mathrm{E}}_{\mathrm{j}}\end{bmatrix} \tag{2.24}$$

The coupled system can be also partitioned regarding internal DOFs a and e and coupling DOFs j:

$$\begin{bmatrix}\mathbf{v}^{*}_{\mathrm{a}}\\ \mathbf{v}^{*}_{\mathrm{j}}\\ \mathbf{v}^{*}_{\mathrm{e}}\end{bmatrix} = \begin{bmatrix}\mathbf{Y}^{*}_{\mathrm{aa}} & \mathbf{Y}^{*}_{\mathrm{aj}} & \mathbf{Y}^{*}_{\mathrm{ae}}\\ \mathbf{Y}^{*}_{\mathrm{ja}} & \mathbf{Y}^{*}_{\mathrm{jj}} & \mathbf{Y}^{*}_{\mathrm{je}}\\ \mathbf{Y}^{*}_{\mathrm{ea}} & \mathbf{Y}^{*}_{\mathrm{ej}} & \mathbf{Y}^{*}_{\mathrm{ee}}\end{bmatrix} \cdot \begin{bmatrix}\mathbf{F}^{*}_{\mathrm{a}}\\ \mathbf{F}^{*}_{\mathrm{j}}\\ \mathbf{F}^{*}_{\mathrm{e}}\end{bmatrix} \tag{2.25}$$

If the two substructures A and E are coupled, the resulting force in the coupling point $\mathbf{F}^{*}_{\mathrm{j}}$ is calculated with the summation of internal forces of the subsystems $\mathbf{F}^{\mathrm{A}}_{\mathrm{j}}$ and $\mathbf{F}^{\mathrm{E}}_{\mathrm{j}}$.

$$\mathbf{F}^{*}_{\mathrm{j}} = \mathbf{F}^{\mathrm{A}}_{\mathrm{j}} + \mathbf{F}^{\mathrm{E}}_{\mathrm{j}} \qquad \mathbf{F}^{\mathrm{A}}_{\mathrm{j}} = \mathbf{F}^{*}_{\mathrm{j}} - \mathbf{F}^{\mathrm{E}}_{\mathrm{j}} \tag{2.26}$$

Due to the fixed connection of the subsystems the velocity needs to be the same:

$$\mathbf{v}^{\mathrm{A}}_{\mathrm{j}} = \mathbf{v}^{\mathrm{E}}_{\mathrm{j}} = \mathbf{v}^{*}_{\mathrm{j}} \tag{2.27}$$

The latter equilibrium can be rewritten using eq. (2.24):

$$\mathbf{Y}^{\mathrm{A}}_{\mathrm{ja}}\mathbf{F}^{\mathrm{A}}_{\mathrm{a}} + \mathbf{Y}^{\mathrm{A}}_{\mathrm{jj}}\mathbf{F}^{\mathrm{A}}_{\mathrm{j}} = \mathbf{Y}^{\mathrm{E}}_{\mathrm{je}}\mathbf{F}^{\mathrm{E}}_{\mathrm{e}} + \mathbf{Y}^{\mathrm{E}}_{\mathrm{jj}}\mathbf{F}^{\mathrm{E}}_{\mathrm{j}} \tag{2.28}$$

Inserting $\mathbf{F}^{\mathrm{A}}_{\mathrm{j}} = \mathbf{F}^{*}_{\mathrm{j}} - \mathbf{F}^{\mathrm{E}}_{\mathrm{j}}$ into eq. (2.28) and rearranging to $\mathbf{F}^{\mathrm{E}}_{\mathrm{j}}$ gives:

$$\mathbf{F}^{\mathrm{E}}_{\mathrm{j}} = (\mathbf{Y}^{\mathrm{A}}_{\mathrm{jj}} + \mathbf{Y}^{\mathrm{E}}_{\mathrm{jj}})^{-1}(\mathbf{Y}^{\mathrm{A}}_{\mathrm{ja}}\mathbf{F}^{\mathrm{A}}_{\mathrm{a}} + \mathbf{Y}^{\mathrm{A}}_{\mathrm{jj}}\mathbf{F}^{*}_{\mathrm{j}} - \mathbf{Y}^{\mathrm{E}}_{\mathrm{je}}\mathbf{F}^{\mathrm{E}}_{\mathrm{e}}) \tag{2.29}$$

And inserting eq. (2.29) into eq. (2.26) gives:

$$\mathbf{F}^{\mathrm{A}}_{\mathrm{j}} = \mathbf{F}^{*}_{\mathrm{j}} - (\mathbf{Y}^{\mathrm{A}}_{\mathrm{jj}} + \mathbf{Y}^{\mathrm{E}}_{\mathrm{jj}})^{-1}(\mathbf{Y}^{\mathrm{A}}_{\mathrm{ja}}\mathbf{F}^{\mathrm{A}}_{\mathrm{a}} + \mathbf{Y}^{\mathrm{A}}_{\mathrm{jj}}\mathbf{F}^{*}_{\mathrm{j}} - \mathbf{Y}^{\mathrm{E}}_{\mathrm{je}}\mathbf{F}^{\mathrm{E}}_{\mathrm{e}}) \tag{2.30}$$

From eq. (2.24) and eq. (2.25) it can be seen that:

$$\mathbf{v}^{\mathrm{A}}_{\mathrm{a}} = \mathbf{Y}^{\mathrm{A}}_{\mathrm{aa}}\mathbf{F}^{\mathrm{A}}_{\mathrm{a}} + \mathbf{Y}^{\mathrm{A}}_{\mathrm{aj}}\mathbf{F}^{\mathrm{A}}_{\mathrm{j}} \tag{2.31}$$

$$\mathbf{v}^{*}_{\mathrm{a}} = \mathbf{Y}^{*}_{\mathrm{aa}}\mathbf{F}^{*}_{\mathrm{a}} + \mathbf{Y}^{*}_{\mathrm{aj}}\mathbf{F}^{*}_{\mathrm{j}} + \mathbf{Y}^{*}_{\mathrm{ae}}\mathbf{F}^{*}_{\mathrm{e}} \tag{2.32}$$

Inserting eq. (2.30) into eq. (2.31):

$$\begin{aligned}\mathbf{v}^{\mathrm{A}}_{\mathrm{a}} =& (\mathbf{Y}^{\mathrm{A}}_{\mathrm{aa}} - \mathbf{Y}^{\mathrm{A}}_{\mathrm{aj}}(\mathbf{Y}^{\mathrm{A}}_{\mathrm{jj}}\mathbf{Y}^{\mathrm{E}}_{\mathrm{jj}})^{-1}\mathbf{Y}^{\mathrm{A}}_{\mathrm{ja}})\mathbf{F}^{\mathrm{A}}_{\mathrm{a}}\\ &+ (\mathbf{Y}^{\mathrm{A}}_{\mathrm{aj}} - \mathbf{Y}^{\mathrm{A}}_{\mathrm{aj}}(\mathbf{Y}^{\mathrm{A}}_{\mathrm{jj}} + \mathbf{Y}^{\mathrm{E}}_{\mathrm{jj}})^{-1}\mathbf{Y}^{\mathrm{A}}_{\mathrm{jj}})\mathbf{F}^{*}_{\mathrm{j}}\\ &+ (\mathbf{Y}^{\mathrm{A}}_{\mathrm{aj}}(\mathbf{Y}^{\mathrm{A}}_{\mathrm{jj}} + \mathbf{Y}^{\mathrm{E}}_{\mathrm{jj}})^{-1}\mathbf{Y}^{\mathrm{E}}_{\mathrm{je}})\mathbf{F}^{\mathrm{E}}_{\mathrm{e}}\end{aligned} \tag{2.33}$$

By comparing eq. (2.33) and eq. (2.32) the following transfer functions of the coupled system can be derived [5]:

$$\mathbf{Y}^*_{\mathrm{aa}} = \mathbf{Y}^{\mathrm{A}}_{\mathrm{aj}} - \mathbf{Y}^{\mathrm{A}}_{\mathrm{aa}}(\mathbf{Y}^{\mathrm{A}}_{\mathrm{jj}} + \mathbf{Y}^{\mathrm{E}}_{\mathrm{jj}})^{-1}\mathbf{Y}^{\mathrm{A}}_{\mathrm{ja}} \tag{2.34}$$
$$\mathbf{Y}^*_{\mathrm{aj}} = \mathbf{Y}^{\mathrm{A}}_{\mathrm{aj}} - \mathbf{Y}^{\mathrm{A}}_{\mathrm{aj}}(\mathbf{Y}^{\mathrm{A}}_{\mathrm{aj}} + \mathbf{Y}^{\mathrm{E}}_{\mathrm{jj}})^{-1}\mathbf{Y}^{\mathrm{A}}_{\mathrm{jj}} \tag{2.35}$$
$$\mathbf{Y}^*_{\mathrm{ae}} = \mathbf{Y}^{\mathrm{A}}_{\mathrm{aj}}(\mathbf{Y}^{\mathrm{A}}_{\mathrm{jj}} + \mathbf{Y}^{\mathrm{E}}_{\mathrm{jj}})^{-1}\mathbf{Y}^{\mathrm{E}}_{\mathrm{je}} \tag{2.36}$$

Analogically, $\mathbf{v}^{\mathrm{E}}_{\mathrm{e}} = \mathbf{Y}^{\mathrm{E}}_{\mathrm{ee}}\mathbf{F}^{\mathrm{E}}_{\mathrm{e}} + \mathbf{Y}^{\mathrm{E}}_{\mathrm{ej}}\mathbf{F}^{\mathrm{E}}_{\mathrm{j}}$ from eq. (2.24) can be used with eq. (2.29) to compare to $\mathbf{v}^*_{\mathrm{e}} = \mathbf{Y}^*_{\mathrm{ea}}\mathbf{F}^*_{\mathrm{a}} + \mathbf{Y}^*_{\mathrm{ej}}\mathbf{F}^*_{\mathrm{j}} + \mathbf{Y}^*_{\mathrm{ee}}\mathbf{F}^*_{\mathrm{e}}$ originating from the third row in eq. (2.25):

$$\mathbf{Y}^*_{\mathrm{ea}} = \mathbf{Y}^{\mathrm{E}}_{\mathrm{ej}}(\mathbf{Y}^{\mathrm{A}}_{\mathrm{jj}} + \mathbf{Y}^{\mathrm{E}}_{\mathrm{jj}})^{-1}\mathbf{Y}^{\mathrm{A}}_{\mathrm{ja}} \tag{2.37}$$
$$\mathbf{Y}^*_{\mathrm{ej}} = \mathbf{Y}^{\mathrm{E}}_{\mathrm{ej}}(\mathbf{Y}^{\mathrm{A}}_{\mathrm{aj}} + \mathbf{Y}^{\mathrm{E}}_{\mathrm{jj}})^{-1}\mathbf{Y}^{\mathrm{A}}_{\mathrm{jj}} \tag{2.38}$$
$$\mathbf{Y}^*_{\mathrm{ee}} = \mathbf{Y}^{\mathrm{E}}_{\mathrm{ee}} - \mathbf{Y}^{\mathrm{E}}_{\mathrm{ej}}(\mathbf{Y}^{\mathrm{A}}_{\mathrm{jj}} + \mathbf{Y}^{\mathrm{E}}_{\mathrm{jj}})^{-1}\mathbf{Y}^{\mathrm{E}}_{\mathrm{je}} \tag{2.39}$$

Inserting eq. (2.30) into $\mathbf{v}^{\mathrm{A}}_{\mathrm{j}} = \mathbf{Y}^{\mathrm{A}}_{\mathrm{ja}}\mathbf{F}^{\mathrm{A}}_{\mathrm{a}} + \mathbf{Y}^{\mathrm{A}}_{\mathrm{jj}}\mathbf{F}^{\mathrm{A}}_{\mathrm{j}}$ and comparing to $\mathbf{v}^*_{\mathrm{j}} = \mathbf{Y}^*_{\mathrm{ja}}\mathbf{F}^*_{\mathrm{a}} + \mathbf{Y}^*_{\mathrm{jj}}\mathbf{F}^*_{\mathrm{j}} + \mathbf{Y}^*_{\mathrm{je}}\mathbf{F}^*_{\mathrm{e}}$ gives:

$$\mathbf{Y}^*_{\mathrm{ja}} = \mathbf{Y}^{\mathrm{A}}_{\mathrm{ja}} - \mathbf{Y}^{\mathrm{A}}_{\mathrm{jj}}(\mathbf{Y}^{\mathrm{A}}_{\mathrm{jj}} + \mathbf{Y}^{\mathrm{E}}_{\mathrm{jj}})^{-1}\mathbf{Y}^{\mathrm{A}}_{\mathrm{ja}} \tag{2.40}$$
$$\mathbf{Y}^*_{\mathrm{jj}} = \mathbf{Y}^{\mathrm{A}}_{\mathrm{jj}} - \mathbf{Y}^{\mathrm{A}}_{\mathrm{jj}}(\mathbf{Y}^{\mathrm{A}}_{\mathrm{aj}} + \mathbf{Y}^{\mathrm{E}}_{\mathrm{jj}})^{-1}\mathbf{Y}^{\mathrm{A}}_{\mathrm{jj}} \tag{2.41}$$
$$\mathbf{Y}^*_{\mathrm{je}} = \mathbf{Y}^{\mathrm{A}}_{\mathrm{jj}}(\mathbf{Y}^{\mathrm{A}}_{\mathrm{jj}} + \mathbf{Y}^{\mathrm{E}}_{\mathrm{jj}})^{-1}\mathbf{Y}^{\mathrm{E}}_{\mathrm{je}} \tag{2.42}$$

Finally the equations (2.34) to (2.42) can be stored in the mobility matrix of the coupled system in the order of the DOFs a, j, e:

$$\mathbf{Y}^* = \begin{bmatrix} \mathbf{Y}^*_{\mathrm{aa}} & \mathbf{Y}^*_{\mathrm{aj}} & \mathbf{Y}^*_{\mathrm{ae}} \\ \mathbf{Y}^*_{\mathrm{ja}} & \mathbf{Y}^*_{\mathrm{jj}} & \mathbf{Y}^*_{\mathrm{je}} \\ \mathbf{Y}^*_{\mathrm{ea}} & \mathbf{Y}^*_{\mathrm{ej}} & \mathbf{Y}^*_{\mathrm{ee}} \end{bmatrix}_{n* \text{ x } n*} \tag{2.43}$$

$$\mathbf{Y}^* = \begin{bmatrix} \mathbf{Y}^{\mathrm{A}}_{\mathrm{aa}} & \mathbf{Y}^{\mathrm{A}}_{\mathrm{aj}} & 0 \\ \mathbf{Y}^{\mathrm{A}}_{\mathrm{ja}} & \mathbf{Y}^{\mathrm{A}}_{\mathrm{jj}} & 0 \\ 0 & 0 & \mathbf{Y}^{\mathrm{E}}_{\mathrm{ee}} \end{bmatrix} - \begin{bmatrix} \mathbf{Y}^{\mathrm{A}}_{\mathrm{aj}} \\ \mathbf{Y}^{\mathrm{A}}_{\mathrm{jj}} \\ \mathbf{Y}^{\mathrm{E}}_{\mathrm{ej}} \end{bmatrix} \cdot \left[\mathbf{Y}^{\mathrm{A}}_{\mathrm{jj}} + \mathbf{Y}^{\mathrm{E}}_{\mathrm{jj}}\right]^{-1}_{n^{\mathrm{j}} \text{ x } n^{\mathrm{j}}} \cdot \left[\mathbf{Y}^{\mathrm{A}}_{\mathrm{ja}}\mathbf{Y}^{\mathrm{A}}_{\mathrm{jj}}(-\mathbf{Y}^{\mathrm{E}}_{\mathrm{je}})\right] \tag{2.44}$$

If reciprocal behaviour is assumed eq. (2.44) can be simplified as follows [20]:

$$\left[\mathbf{Y}^{\mathrm{A}}_{\mathrm{aj}}\mathbf{Y}^{\mathrm{A}}_{\mathrm{jj}}(-\mathbf{Y}^{\mathrm{E}}_{\mathrm{ej}})\right] = \begin{bmatrix} \mathbf{Y}^{\mathrm{A}}_{\mathrm{aj}} \\ \mathbf{Y}^{\mathrm{A}}_{\mathrm{jj}} \\ (-\mathbf{Y}^{\mathrm{E}}_{\mathrm{ej}}) \end{bmatrix}^{\mathrm{T}} \tag{2.45}$$

It can be seen the Receptance Coupling needs only one matrix inversion and its dimension is determined by the coupling DOFs n^{j}. This matrix is usually smaller than the three inverted matrices with the dimensions n^{A}, n^{E} and $n^* = n^{\mathrm{A}} + n^{\mathrm{E}} - n^{\mathrm{j}}$ presented in the Impedance Coupling Method in section 2.2.2.

[5] The external force acting on the subsystems is the same as the external forces in the assembly, which means that $\mathbf{F}^{\mathrm{A}}_{\mathrm{a}} = \mathbf{F}^*_{\mathrm{a}}$ and $\mathbf{F}^{\mathrm{E}}_{\mathrm{e}} = \mathbf{F}^*_{\mathrm{e}}$.

2.2.4 Generalized Receptance Coupling for several substructures

The four subsystems A,B,C and D in fig. 2.6 shall be coupled to the subsystem E. Resulting FRFs for the total coupled solution could be achieved by using the Receptance Coupling Method for two substructures in sequence. After coupling system A with system E, this assembled system can be coupled to system B etc. By doing so one needs to keep track of which DOFs are internal and which are coupling DOFs. For instance the DOFs in the intersection J between subsystem A and E become in the second step internal DOFs, whereas they are coupling DOFs in the first step of the coupling procedure. Thus, when coupling quite a few subsystems it might be convenient to use a generalized coupling procedure. The Receptance Coupling for two substructures in the previous section can be extended to the so called Generalized Receptance Coupling (GRC) for cases with any number of subsystems. The GRC was formulated by B. Jetmundsen in reference [14]. This method makes use of graph theory and a boolean mapping matrix, that maps the interfaces of the system to the connected subsystems. The Generalized Receptance Coupling can be used with receptance, mobility or accelerance in the same manner. In this thesis the coupled solution is presented with respect to the mobility:

$$\mathbf{Y}^* = \mathbf{Y}_{\alpha\alpha} - \mathbf{M} \otimes \mathbf{Y}_{\alpha\gamma} \cdot \left[\sum_{i=1}^{N} \mathbf{M}_i^T \mathbf{M}_i \otimes \mathbf{Y}_{\gamma\gamma}^i \right]^{-1} \mathbf{M} \otimes \mathbf{Y}_{\alpha\gamma}^T \tag{2.46}$$

Where:

α: Sets of internal DOFs of the subsystems.

γ: Sets of interface DOFs of the subsystems.

$\mathbf{Y}^*$: Total coupled mobility matrix.

$\mathbf{Y}_{\alpha\alpha}$: The mobility matrix of the uncoupled subsystem relative to α, including one retained set of the coupling DOFs if results there are wanted.

$\mathbf{M}$: Boolean mapping matrix.

$\mathbf{M}_i$: The i:th row of the boolean mapping matrix (belonging to the i:th subsystem).

$\mathbf{Y}_{\alpha\gamma}$: Mobility matrix of the interface to internal DOFs.

$\mathbf{Y}_{\gamma\gamma}^i$: Mobility matrix for the transfer and point relations for the interface DOF of the i:th substructure.

$\otimes$: Element by element matrix product. [14]

Example of four wheels coupling to chassis

For the case with four wheels coupled to a wheel suspensions (could be two, for front and rear chassis) a system can be set-up with graph theory (including a chosen sign convention) as fig. 2.6.

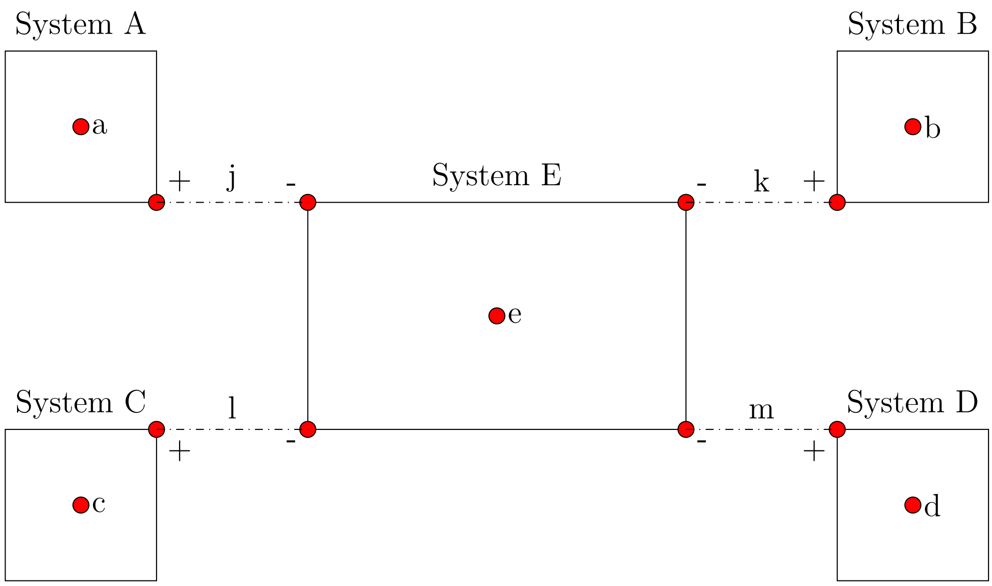

Figure 2.6: Five subsystems to be coupled at four different points.

$\mathbf{Y}_{\alpha\alpha}$ stores the uncoupled FRFs with respect to their internal DOFs for all subsystems diagonally in a matrix.

$$\mathbf{Y}_{\alpha\alpha} = \begin{bmatrix} \mathbf{Y}^{\mathrm{A}}_{\mathrm{aa}} & 0 & 0 & 0 & 0 \\ 0 & \mathbf{Y}^{\mathrm{B}}_{\mathrm{bb}} & 0 & 0 & 0 \\ 0 & 0 & \mathbf{Y}^{\mathrm{C}}_{\mathrm{cc}} & 0 & 0 \\ 0 & 0 & 0 & \mathbf{Y}^{\mathrm{D}}_{\mathrm{dd}} & 0 \\ 0 & 0 & 0 & 0 & \mathbf{Y}^{\mathrm{E}}_{\mathrm{ee}} \end{bmatrix} \tag{2.47}$$

$\mathbf{Y}_{\alpha\gamma}$ and $\mathbf{Y}_{\gamma\alpha}$ are the FRFs between the internal set of DOF, $\alpha = \{\mathrm{a, b, c, d, e}\}$ and the set of interface DOF $\gamma = \{\mathrm{j, k, l, m}\}$ and vice versa.

$$\mathbf{Y}_{\alpha\gamma} = \begin{bmatrix} \mathbf{Y}^{\mathrm{A}}_{\mathrm{aj}} & \mathbf{Y}^{\mathrm{A}}_{\mathrm{ak}} & \mathbf{Y}^{\mathrm{A}}_{\mathrm{al}} & \mathbf{Y}^{\mathrm{A}}_{\mathrm{am}} \\ \mathbf{Y}^{\mathrm{B}}_{\mathrm{bj}} & \mathbf{Y}^{\mathrm{B}}_{\mathrm{bk}} & \mathbf{Y}^{\mathrm{B}}_{\mathrm{bl}} & \mathbf{Y}^{\mathrm{B}}_{\mathrm{bm}} \\ \mathbf{Y}^{\mathrm{C}}_{\mathrm{cj}} & \mathbf{Y}^{\mathrm{C}}_{\mathrm{ck}} & \mathbf{Y}^{\mathrm{C}}_{\mathrm{cl}} & \mathbf{Y}^{\mathrm{C}}_{\mathrm{cm}} \\ \mathbf{Y}^{\mathrm{D}}_{\mathrm{dj}} & \mathbf{Y}^{\mathrm{D}}_{\mathrm{dk}} & \mathbf{Y}^{\mathrm{D}}_{\mathrm{dl}} & \mathbf{Y}^{\mathrm{D}}_{\mathrm{dm}} \\ \mathbf{Y}^{\mathrm{E}}_{\mathrm{ej}} & \mathbf{Y}^{\mathrm{E}}_{\mathrm{ek}} & \mathbf{Y}^{\mathrm{E}}_{\mathrm{el}} & \mathbf{Y}^{\mathrm{E}}_{\mathrm{em}} \end{bmatrix} \tag{2.48}$$

In $\mathbf{Y}_{\alpha\gamma}$ each element of the matrix corresponds to the sets of FRFs from the the internal DOFs, α, to the interface DOFs, γ. Each row corresponds to a subsystem (A, B, C, D, E). $\mathbf{Y}_{\gamma\alpha}$ is the FRF in the opposite direction, from internal DOFs to inteface DOFs.

$\mathbf{Y}^{\mathrm{i}}_{\gamma\gamma}$ is the matrix for the FRFs between the interface DOFs. This matrix is generated for each subsystem i:

$$\mathbf{Y}^{\mathrm{i}}_{\gamma\gamma} = \begin{bmatrix} \mathbf{Y}^{\mathrm{i}}_{\mathrm{jj}} & \mathbf{Y}^{\mathrm{i}}_{\mathrm{jk}} & \mathbf{Y}^{\mathrm{i}}_{\mathrm{jl}} & \mathbf{Y}^{\mathrm{i}}_{\mathrm{jm}} \\ \mathbf{Y}^{\mathrm{i}}_{\mathrm{kj}} & \mathbf{Y}^{\mathrm{i}}_{\mathrm{kk}} & \mathbf{Y}^{\mathrm{i}}_{\mathrm{kl}} & \mathbf{Y}^{\mathrm{i}}_{\mathrm{km}} \\ \mathbf{Y}^{\mathrm{i}}_{\mathrm{lj}} & \mathbf{Y}^{\mathrm{i}}_{\mathrm{lk}} & \mathbf{Y}^{\mathrm{i}}_{\mathrm{ll}} & \mathbf{Y}^{\mathrm{i}}_{\mathrm{lm}} \\ \mathbf{Y}^{\mathrm{i}}_{\mathrm{mj}} & \mathbf{Y}^{\mathrm{i}}_{\mathrm{mk}} & \mathbf{Y}^{\mathrm{i}}_{\mathrm{ml}} & \mathbf{Y}^{\mathrm{i}}_{\mathrm{mm}} \end{bmatrix} \tag{2.49}$$

Boolean mapping matrix

In fig. 2.6 a system can be seen consisting of five subsystems (A, B, C, D, E) that are connected with four interfaces (J, K, L, M) having the interface DOFs j, k, l, m. These are connected in the figure according to graph theory, a sign convention is chosen and shown as "+" or "-". This is then used to determine a boolean mapping matrix, eq. (2.50). The columns represent the interfaces and the rows the subsystems. The element will be determined to a 1 or -1 depending on the chosen graph and sign convention in fig. 2.6. If a subsystem does not connect with a specific interface a zero will be placed at the element position in the matrix.

$$\mathbf{M} = \begin{array}{c c} \begin{array}{cccc} \mathrm{J} & \mathrm{K} & \mathrm{L} & \mathrm{M} \end{array} & \\ \begin{bmatrix} 1 & 0 & 0 & 0 \\ 0 & 1 & 0 & 0 \\ 0 & 0 & 1 & 0 \\ 0 & 0 & 0 & 1 \\ -1 & -1 & -1 & -1 \end{bmatrix} & \begin{array}{c} \mathrm{A} \\ \mathrm{B} \\ \mathrm{C} \\ \mathrm{D} \\ \mathrm{E} \end{array} \end{array} \tag{2.50}$$

Each column in $\mathbf{M}$ belongs to an interface (J, K, L , M). Each row belongs to a subsystem (A, B, C, D, E). An element filled with a 1 or -1 shows therefore if the subsystem has a set of DOFs coupled in the specific interface.

$\mathbf{M}_i^T \cdot \mathbf{M}_i$ gives a new mapping matrix where i is the i:th row of $\mathbf{M}$ which corresponds to the i:th substructure. This new mapping matrix "organizes the interface DOFs and their interconnections" for the transfer and point relations between the interface DOFs in eq. (2.46) [14]. This new mapping matrix can be multiplied with $\mathbf{Y}^{\mathrm{i}}_{\gamma\gamma}$. An example can be seen below for subsystem A and E.

$$\mathbf{M}_\mathrm{A}^\mathrm{T}\mathbf{M}_\mathrm{A} = \begin{bmatrix}1\\0\\0\\0\end{bmatrix}\begin{bmatrix}1 & 0 & 0 & 0\end{bmatrix} = \begin{bmatrix}1 & 0 & 0 & 0\\0 & 0 & 0 & 0\\0 & 0 & 0 & 0\\0 & 0 & 0 & 0\end{bmatrix} \tag{2.51}$$

$$\mathbf{M}_\mathrm{E}^\mathrm{T}\mathbf{M}_\mathrm{E} = \begin{bmatrix}-1\\-1\\-1\\-1\end{bmatrix}\begin{bmatrix}-1 & -1 & -1 & -1\end{bmatrix} = \begin{bmatrix}1 & 1 & 1 & 1\\1 & 1 & 1 & 1\\1 & 1 & 1 & 1\\1 & 1 & 1 & 1\end{bmatrix} \tag{2.52}$$

$$\mathbf{M}_\mathrm{A}^\mathrm{T}\mathbf{M}_\mathrm{A} \otimes \mathbf{Y}_{\gamma\gamma}^{A} = \begin{bmatrix}1 & 0 & 0 & 0\\0 & 0 & 0 & 0\\0 & 0 & 0 & 0\\0 & 0 & 0 & 0\end{bmatrix} \otimes \begin{bmatrix}\mathbf{Y}_\mathrm{jj}^\mathrm{A} & \mathbf{Y}_\mathrm{jk}^\mathrm{A} & \mathbf{Y}_\mathrm{jl}^\mathrm{A} & \mathbf{Y}_\mathrm{jm}^\mathrm{A}\\\mathbf{Y}_\mathrm{kj}^\mathrm{A} & \mathbf{Y}_\mathrm{kk}^\mathrm{A} & \mathbf{Y}_\mathrm{kl}^\mathrm{A} & \mathbf{Y}_\mathrm{km}^\mathrm{A}\\\mathbf{Y}_\mathrm{lj}^\mathrm{A} & \mathbf{Y}_\mathrm{lk}^\mathrm{A} & \mathbf{Y}_\mathrm{ll}^\mathrm{A} & \mathbf{Y}_\mathrm{lm}^\mathrm{A}\\\mathbf{Y}_\mathrm{mj}^\mathrm{A} & \mathbf{Y}_\mathrm{mk}^\mathrm{A} & \mathbf{Y}_\mathrm{ml}^\mathrm{A} & \mathbf{Y}_\mathrm{mm}^\mathrm{A}\end{bmatrix} \tag{2.53}$$

$$= \begin{bmatrix}\mathbf{Y}_\mathrm{jj}^\mathrm{A} & 0 & 0 & 0\\0 & 0 & 0 & 0\\0 & 0 & 0 & 0\\0 & 0 & 0 & 0\end{bmatrix} \tag{2.54}$$

$$\mathbf{M}_\mathrm{E}^\mathrm{T}\mathbf{M}_\mathrm{E} \otimes \mathbf{Y}_{\gamma\gamma}^{E} = \begin{bmatrix}1 & 1 & 1 & 1\\1 & 1 & 1 & 1\\1 & 1 & 1 & 1\\1 & 1 & 1 & 1\end{bmatrix} \otimes \begin{bmatrix}\mathbf{Y}_\mathrm{jj}^\mathrm{E} & \mathbf{Y}_\mathrm{jk}^\mathrm{E} & \mathbf{Y}_\mathrm{jl}^\mathrm{E} & \mathbf{Y}_\mathrm{jm}^\mathrm{E}\\\mathbf{Y}_\mathrm{kj}^\mathrm{E} & \mathbf{Y}_\mathrm{kk}^\mathrm{E} & \mathbf{Y}_\mathrm{kl}^\mathrm{E} & \mathbf{Y}_\mathrm{km}^\mathrm{E}\\\mathbf{Y}_\mathrm{lj}^\mathrm{E} & \mathbf{Y}_\mathrm{lk}^\mathrm{E} & \mathbf{Y}_\mathrm{ll}^\mathrm{E} & \mathbf{Y}_\mathrm{lm}^\mathrm{E}\\\mathbf{Y}_\mathrm{mj}^\mathrm{E} & \mathbf{Y}_\mathrm{mk}^\mathrm{E} & \mathbf{Y}_\mathrm{ml}^\mathrm{E} & \mathbf{Y}_\mathrm{mm}^\mathrm{E}\end{bmatrix} \tag{2.55}$$

$$= \begin{bmatrix}\mathbf{Y}_\mathrm{jj}^\mathrm{E} & \mathbf{Y}_\mathrm{jk}^\mathrm{E} & \mathbf{Y}_\mathrm{jl}^\mathrm{E} & \mathbf{Y}_\mathrm{jm}^\mathrm{E}\\\mathbf{Y}_\mathrm{kj}^\mathrm{E} & \mathbf{Y}_\mathrm{kk}^\mathrm{E} & \mathbf{Y}_\mathrm{kl}^\mathrm{E} & \mathbf{Y}_\mathrm{km}^\mathrm{E}\\\mathbf{Y}_\mathrm{lj}^\mathrm{E} & \mathbf{Y}_\mathrm{lk}^\mathrm{E} & \mathbf{Y}_\mathrm{ll}^\mathrm{E} & \mathbf{Y}_\mathrm{lm}^\mathrm{E}\\\mathbf{Y}_\mathrm{mj}^\mathrm{E} & \mathbf{Y}_\mathrm{mk}^\mathrm{E} & \mathbf{Y}_\mathrm{ml}^\mathrm{E} & \mathbf{Y}_\mathrm{mm}^\mathrm{E}\end{bmatrix} \tag{2.56}$$

2.57 can then be used to sum up the FRFs for the sets of interface DOFs for each subsystem [13]

$$\sum_{i=1}^{N} \mathbf{M}_\mathrm{i}^\mathrm{T}\mathbf{M}_\mathrm{i} \otimes \mathbf{Y}_{\gamma\gamma}^{i} \tag{2.57}$$

where N is the number of subsystems.

The FRFs of the coupled solution refering to fig. 2.6 can then be calculated using eq. (2.46):

$$
\begin{aligned}
\mathbf{Y}^* &= \begin{bmatrix}
\mathbf{Y}^*_{\mathrm{aa}} & \mathbf{Y}^*_{\mathrm{ab}} & \mathbf{Y}^*_{\mathrm{ac}} & \mathbf{Y}^*_{\mathrm{ad}} & \mathbf{Y}^*_{\mathrm{ae}} \\
\mathbf{Y}^*_{\mathrm{ba}} & \mathbf{Y}^*_{\mathrm{bb}} & \mathbf{Y}^*_{\mathrm{bc}} & \mathbf{Y}^*_{\mathrm{bd}} & \mathbf{Y}^*_{\mathrm{be}} \\
\mathbf{Y}^*_{\mathrm{ca}} & \mathbf{Y}^*_{\mathrm{cb}} & \mathbf{Y}^*_{\mathrm{cc}} & \mathbf{Y}^*_{\mathrm{cd}} & \mathbf{Y}^*_{\mathrm{ce}} \\
\mathbf{Y}^*_{\mathrm{da}} & \mathbf{Y}^*_{\mathrm{db}} & \mathbf{Y}^*_{\mathrm{dc}} & \mathbf{Y}^*_{\mathrm{dd}} & \mathbf{Y}^*_{\mathrm{de}} \\
\mathbf{Y}^*_{\mathrm{ea}} & \mathbf{Y}^*_{\mathrm{eb}} & \mathbf{Y}^*_{\mathrm{ec}} & \mathbf{Y}^*_{\mathrm{ed}} & \mathbf{Y}^*_{\mathrm{ee}}
\end{bmatrix} \\
&= \begin{bmatrix}
\mathbf{Y}_{\mathrm{aa}} & 0 & 0 & 0 & 0 \\
0 & \mathbf{Y}_{\mathrm{bb}} & 0 & 0 & 0 \\
0 & 0 & \mathbf{Y}_{\mathrm{cc}} & 0 & 0 \\
0 & 0 & 0 & \mathbf{Y}_{\mathrm{dd}} & 0 \\
0 & 0 & 0 & 0 & \mathbf{Y}_{\mathrm{ee}}
\end{bmatrix} - \begin{bmatrix}
\mathbf{Y}^{\mathrm{A}}_{\mathrm{aj}} & 0 & 0 & 0 \\
0 & \mathbf{Y}^{\mathrm{B}}_{\mathrm{bk}} & 0 & 0 \\
0 & 0 & \mathbf{Y}^{\mathrm{C}}_{\mathrm{cl}} & 0 \\
0 & 0 & 0 & \mathbf{Y}^{\mathrm{D}}_{\mathrm{dm}} \\
-\mathbf{Y}^{\mathrm{E}}_{\mathrm{ej}} & -\mathbf{Y}^{\mathrm{E}}_{\mathrm{ek}} & -\mathbf{Y}^{\mathrm{E}}_{\mathrm{el}} & -\mathbf{Y}^{\mathrm{E}}_{\mathrm{em}}
\end{bmatrix} \\
&\cdot \begin{bmatrix}
(\mathbf{Y}^{\mathrm{A}}_{\mathrm{jj}} + \mathbf{Y}^{\mathrm{E}}_{\mathrm{jj}}) & \mathbf{Y}^{\mathrm{E}}_{\mathrm{jk}} & \mathbf{Y}^{\mathrm{E}}_{\mathrm{jl}} & \mathbf{Y}^{\mathrm{E}}_{\mathrm{jm}} \\
\mathbf{Y}^{\mathrm{E}}_{\mathrm{kj}} & (\mathbf{Y}^{\mathrm{B}}_{\mathrm{kk}} + \mathbf{Y}^{\mathrm{E}}_{\mathrm{kk}}) & \mathbf{Y}^{\mathrm{E}}_{\mathrm{kl}} & \mathbf{Y}^{\mathrm{E}}_{\mathrm{km}} \\
\mathbf{Y}^{\mathrm{E}}_{\mathrm{lj}} & \mathbf{Y}^{\mathrm{E}}_{\mathrm{lk}} & (\mathbf{Y}^{\mathrm{C}}_{\mathrm{ll}} + \mathbf{Y}^{\mathrm{E}}_{\mathrm{ll}}) & \mathbf{Y}^{\mathrm{E}}_{\mathrm{lm}} \\
\mathbf{Y}^{\mathrm{E}}_{\mathrm{mj}} & \mathbf{Y}^{\mathrm{E}}_{\mathrm{mk}} & \mathbf{Y}^{\mathrm{E}}_{\mathrm{ml}} & (\mathbf{Y}^{\mathrm{D}}_{\mathrm{mm}} + \mathbf{Y}^{\mathrm{E}}_{\mathrm{mm}})
\end{bmatrix}^{-1} \\
&\cdot \begin{bmatrix}
\mathbf{Y}^{\mathrm{A}}_{\mathrm{ja}} & 0 & 0 & 0 & -\mathbf{Y}^{\mathrm{E}}_{\mathrm{je}} \\
0 & \mathbf{Y}^{\mathrm{B}}_{\mathrm{kb}} & 0 & 0 & -\mathbf{Y}^{\mathrm{E}}_{\mathrm{ke}} \\
0 & 0 & \mathbf{Y}^{\mathrm{C}}_{\mathrm{lc}} & 0 & -\mathbf{Y}^{\mathrm{E}}_{\mathrm{le}} \\
0 & 0 & 0 & \mathbf{Y}^{\mathrm{D}}_{\mathrm{md}} & -\mathbf{Y}^{\mathrm{E}}_{\mathrm{me}}
\end{bmatrix}
\end{aligned} \tag{2.58}
$$

3

Coupling of simple beam models

The previous described theory of the Impedance Coupling and Receptance Coupling method is implemented in Matlab. To validated the code a simple setup with three subsystems is chosen. The idea is to extract uncoupled FRFs and use them as an input to the coupling code. This result can then be compared to the direct solution in the simulation software. Hereby the the subsystems are connected and the FRFs are extracted. After describing the setup of this test, the obtained results will be discussed in this chapter.

3.1 Method

Three 1D-beams are modeled in the software Hypermesh from Altair, as can be seen in fig. 3.1. With properties according to:

- Cross-section width: 10 mm
- Cross-section height: 40 mm
- Length of green and pink beams: 2000 mm
- Length of red beam: 1000 mm
- Elasticity modulus: 210 GPa
- Poisson ratio: 0.3
- Density: 8000 $\frac{kg}{m^3}$
- Mesh size 10 mm per element

The beams are connected at the node 205 and 307 in fig. 3.1, with a shared node, therefore with equivalent displacement in that node for the beams. The FRFs for the coupled beams from node 5 to 490 is then calculated through the solver Optistruct with the solution type direct frequency response where the FRFs are calculated with a direct solution as can be seen in section 2.1. Simulations are made for the FRFs of the three separate beams from node 5 to 205 and 307 to 490 for the long beams and from 205 to 307 for the short beam. The FRFs are exported to Matlab and coupled with Impedance Coupling and Receptance Coupling technique seen in section 2.2.2 and 2.2.3.

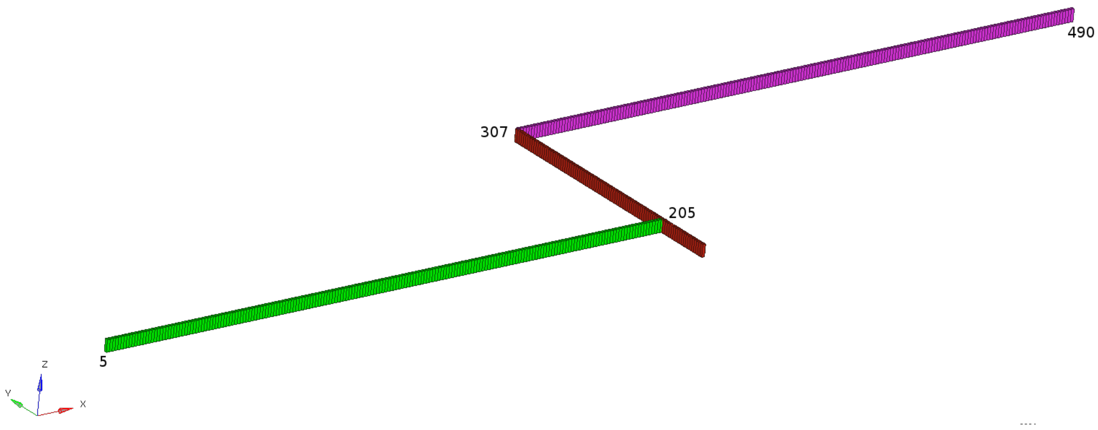

Figure 3.1: Three subsystems coupled in Hypermesh

3.2 Results and discussion

The results for the Receptance Coupling, Impedance Coupling and Direct Coupling Method are displayed in fig. 3.2. All curves match very well over the chosen frequency range which confirms that the coupling method works.

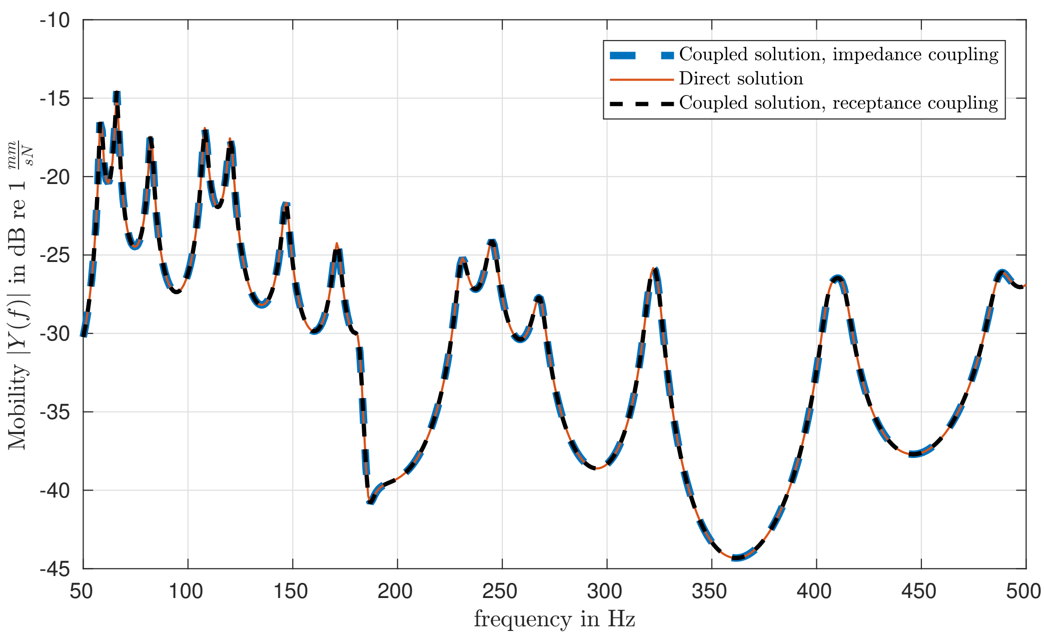

Figure 3.2: Transfer function from point 5 to point 307 related to fig. 3.1

4

Coupling of tire and chassis model

In this chapter the tire and the vehicle model are explained. Moving on, the Receptance Coupling Method is applied to the data set of the subsystems and the results are shown for the coupling of one tire to the rear chassis.

4.1 Method

4.1.1 Chassis model

The CAE rear chassis model as seen in fig. 4.1 is provided from the Volvo Car Group. The model is imported to the software Hypermesh. Calculations of the FRF for the chassis are concluded with the solver Optistruct. Later in the coupling process, the response at the rear chassis shall be obtained for the chosen bushing, which is marked in fig. 4.1. One tire will be connected to the spindle seen in fig. 4.1. The driving point and transfer functions are generated at and between the spindle and the bushing.

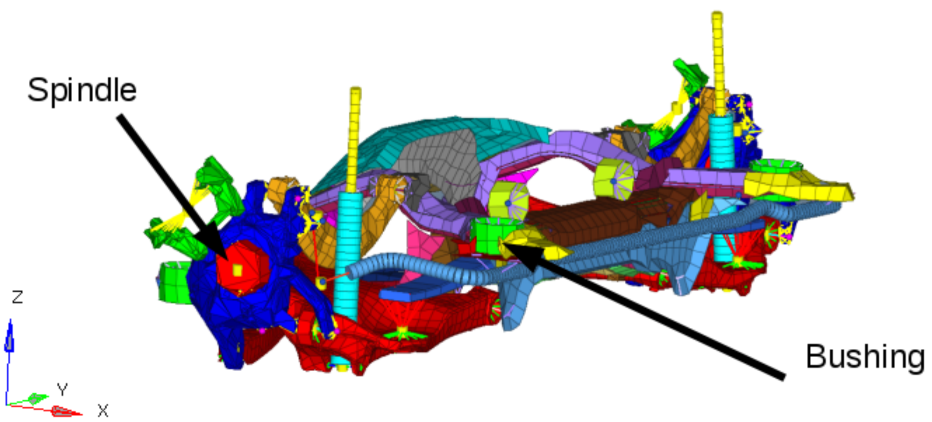

Figure 4.1: Simple chassis model with the chosen spindle and bushing position

In fig. 4.2 and 4.3 the response at the bushing in the chassis model is depicted for the translational and rotational DOFs respectively due to a uniform excitation in z direction at the hub (coupling point). The eigenfrequencies of the vehicle chassis can be spotted at 14 Hz, 37 Hz and at 47 Hz.

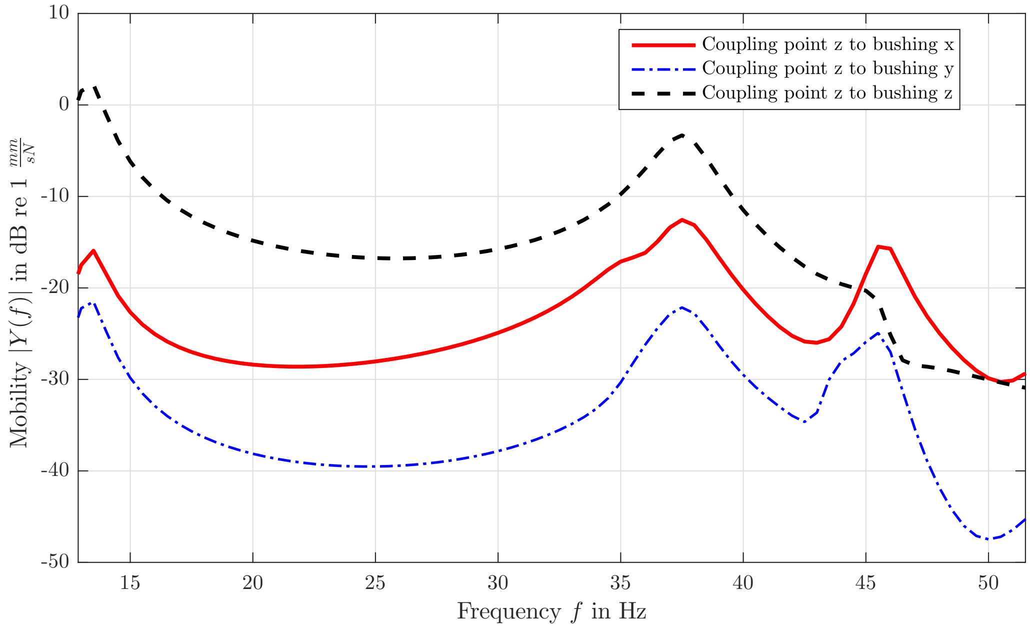

Figure 4.2: Mobility spindle to bushing, translational DOFs, 1st harmonic, uncoupled vehicle

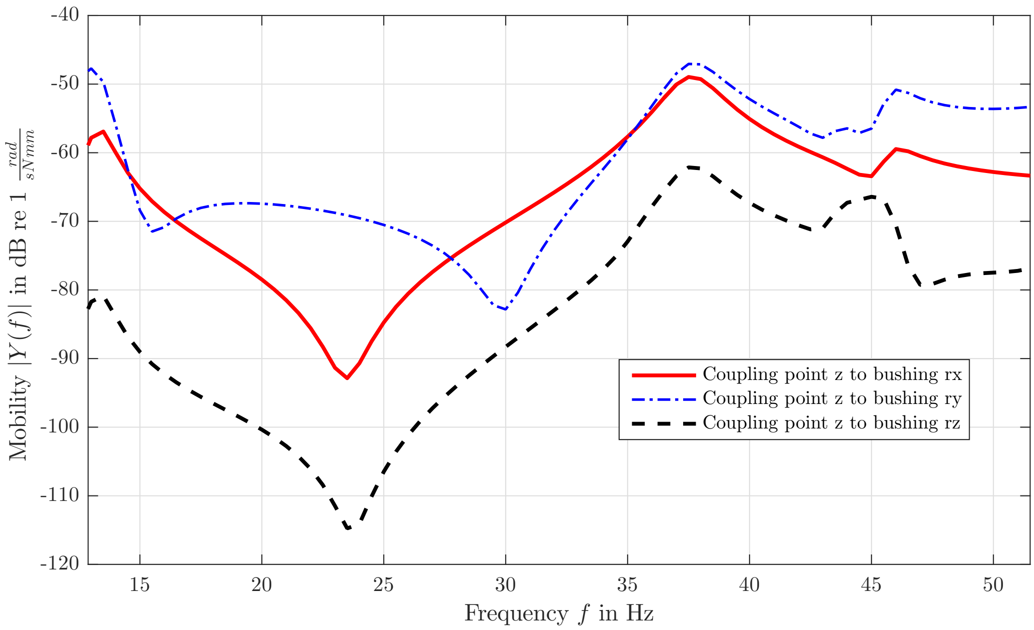

Figure 4.3: Mobility spindle to bushing, rotational DOFs, 1st harmonic, uncoupled vehicle

4.1.2 Tire model

For the purpose of this thesis a comparable simple tire model is used to ensure a feasible implementation. Due to an certain discretization of the structure the model is valid up to 160 Hz. This limitation should be kept in mind when looking at concerning plots in this report later. The modal tire model is synthesized with 400 modes belonging to 200 positive and 200 negative eigenfrequencies. The highest eigenfrequency is about 800 Hz. Due to gyroscopic forces of the rotating tire, the mode shapes become complex. Seven different excitation cases as depicted in fig. 4.4 are considered in the tire model. This plot shows the dependency between speed and excitation frequency of each harmonic load case. It should be mentioned that the names of the harmonics: 1st. harmonic, 2nd harmonic etc.) does not correspond to the number of events per revolution. With increased vehicle speed the excitation frequency of the tire due to the surface roughness of the underground increases. The dynamic properties of the tire are not the same for each speed. Therefore, in the modal model provided by the Continental AG six different operating points (20 km/h, 40 km/h, 60 km/h, 80 km/h, 100 km/h, 120 km/h) are calculated. These operating points are indicated as horizontal lines in fig. 4.4. In order to predict the response of the tire due to the given excitation, along with the harmonic line, the operating points are interpolated over the vehicle speed.

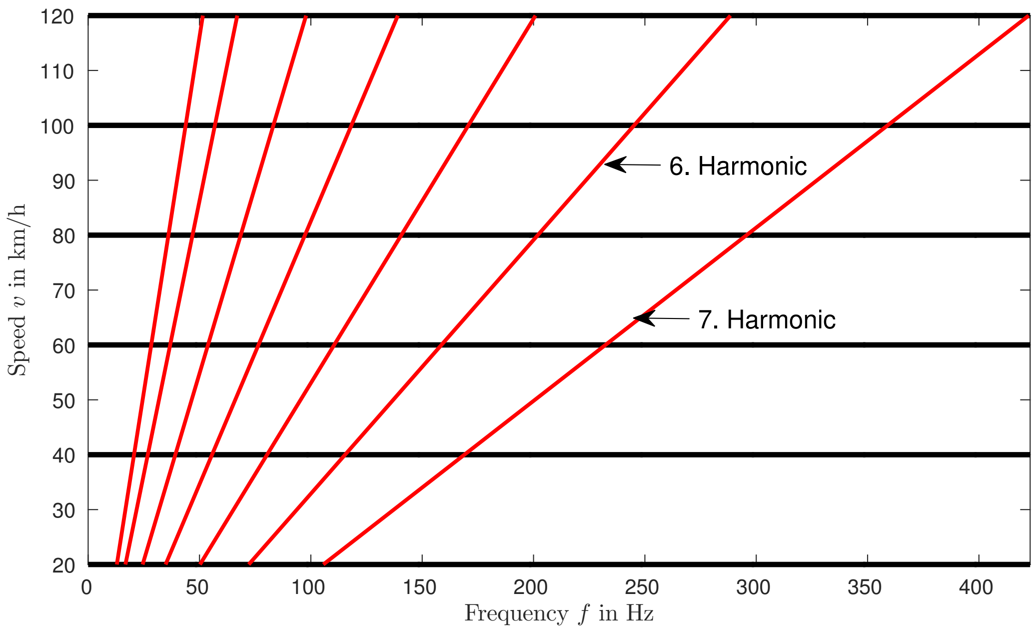

Figure 4.4: Harmonic excitation cases, speed-frequency dependence.

In order to calculate the response at the bushing, lets recapture how this is calculated with eq. (2.37) and eq. (2.25):

$$\mathbf{v}_{\mathrm{e}}^{*} = \mathbf{Y}_{\mathrm{ea}}^{*}\mathbf{F}_{\mathrm{a}} = \mathbf{Y}_{\mathrm{ej}}^{\mathrm{E}}(\mathbf{Y}_{\mathrm{jj}}^{\mathrm{A}} + \mathbf{Y}_{\mathrm{jj}}^{\mathrm{E}})^{-1}\mathbf{Y}_{\mathrm{ja}}^{\mathrm{A}}\mathbf{F}_{\mathrm{a}} \tag{4.1}$$

The excitation force $\mathbf{F}_{\mathrm{a}}$ at the tire patch and the FRF from the tire patch to the coupling point $\mathbf{Y}_{\mathrm{ja}}^{\mathrm{A}}$ could not be obtained from the provided Matlab script individually. But instead the response at the coupling point due to the excitation at the tire patch $\mathbf{Y}_{\mathrm{ja}}^{\mathrm{A}}\mathbf{F}_{\mathrm{a}}$ is known. This means that the coupling can be performed according to eq. (4.1) without knowing the force by itself.

Before using the Receptance Coupling Method the tire model is transformed to the coordinate system of the vehicle. The following plots for the three translational x, y, z directions are according the vehicle coordinate system in fig. 4.5. The rotational DOFs are named as rx, ry, rz for rotations around the x-, y- and z-axis.

In fig. 4.6 and fig. 4.7 the translational and rotational response DOFs due to an excitation at the tire patch are displayed for the first harmonic. It can be seen that eigenfrequencies are located at 17 Hz and 38 Hz for this excitation case in the tire model.

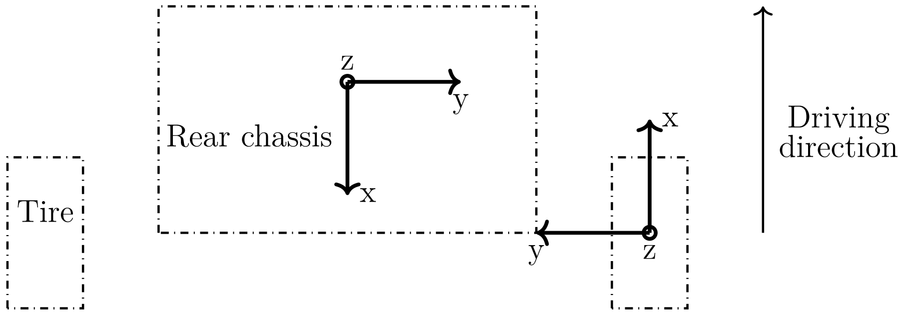

Figure 4.5: Coordinate system of tire and the vehicle model, top view.

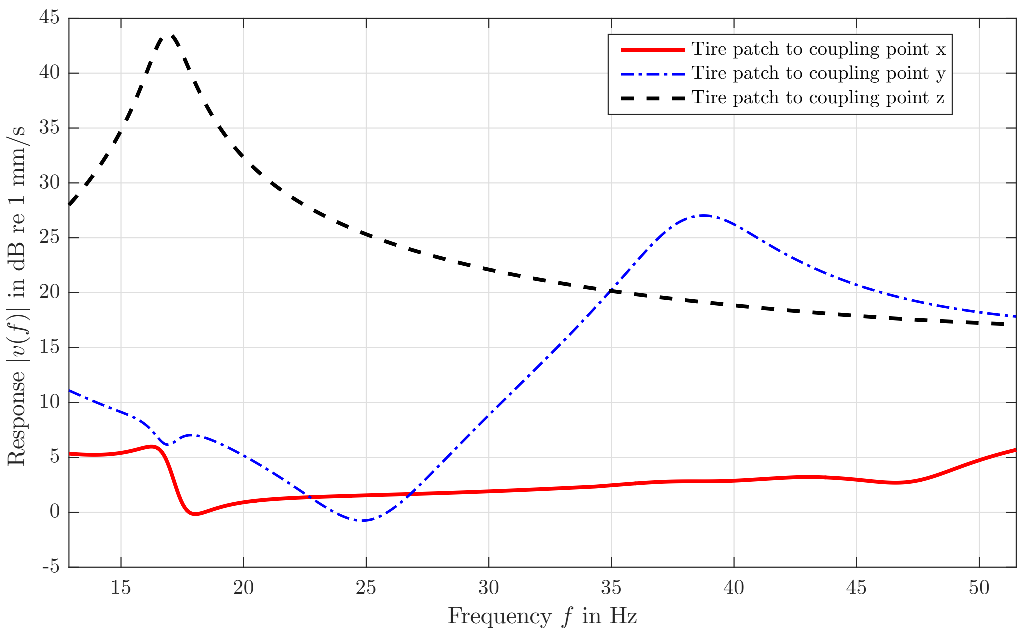

Figure 4.6: Translational response at rim due to excitation at tire patch, 1st harmonic, uncoupled tire

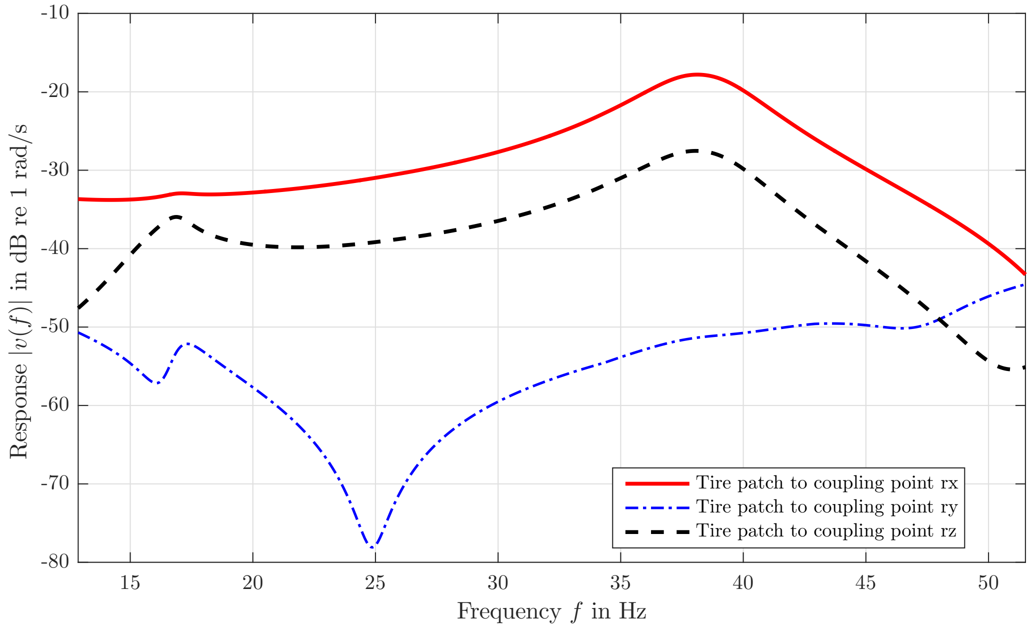

Figure 4.7: Rotational response at rim due to excitation at tire patch, 1st harmonic, uncoupled tire

4.2 Results and discussion

By looking at the translational responses at the bushing for the excitation case of the 1st harmonic in fig. 4.8 it can be seen, that the response in z direction is most prominent in the considered frequency range between 12 Hz and 52 Hz. This observation is not unexpected since the tire patch is excited in x and z direction and not in y direction. There are two striking resonances in the z direction at 14 Hz and 38 Hz. The rotational responses are depicted in fig. 4.9. The most noticable and broad resonance peak occurs at 37 Hz for the rotation around the x-axis. Before and after this resonance the rotations around the y-axis are the highest in the comparison of the translational DOFs. In contrast to that the rz DOF shows rather weak amplitudes in the whole frequency range up to 45 Hz.

Results of the remaining excitation cases can be found in appendix A and will not be discussed here.

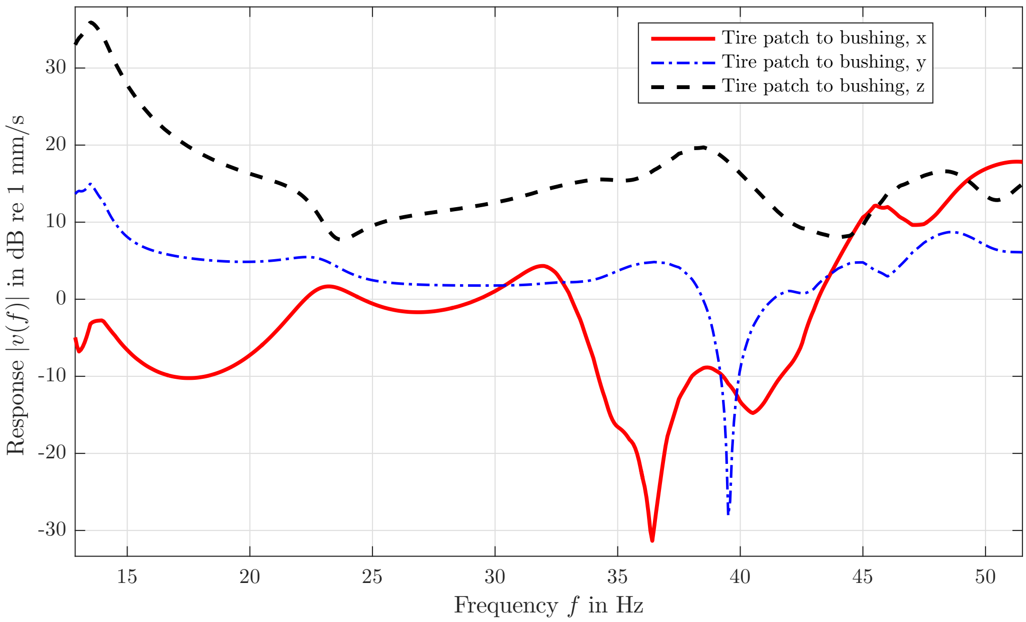

Figure 4.8: Translational response at the bushing due to excitation at the tire patch, 1st harmonic

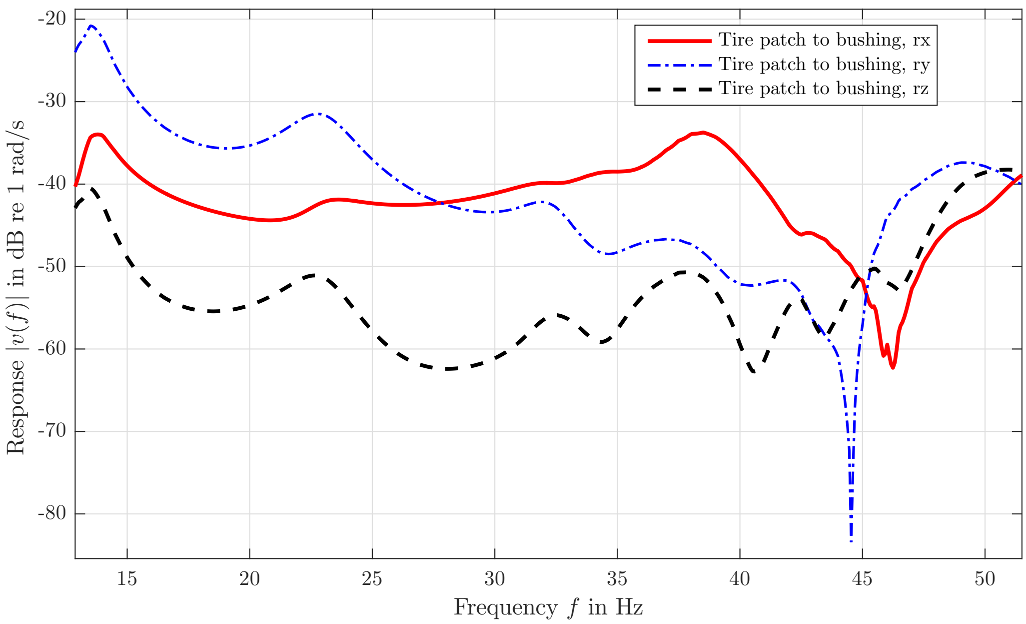

Figure 4.9: Rotational response at the bushing due to excitation at the tire patch, 1st harmonic

5

Sensitivity study on coupled solution

After finding the solution for the coupling of the tire and the vehicle model, the question rises how accurate the assembled prediction is. This is a broad question, which can not be answered in general. Two different tests in varying the input data are performed as example case studies. These are studies regarding modal truncation errors in the tire model and FRF pollution with random noise in both subsystems tire and vehicle. With these sensitivity case studies one has to assume, that the reference model is correct. If this is not the case this could lead to wrong interpretations since different sensitivities can be expected for different system properties [7].

5.1 Modal truncation errors introduced into tire model

The background to this first case study is, that the tire model is very complex and nonlinear and it means a lot of effort for the tire manufacture to develop accurate models. As discussed earlier, the tire model includes 400 modes and the highest eigenfrequency is about 800 Hz. From this point of view it is very meaningful to know how much influence do high order modes have on the prediction up to the desired frequency of 160 Hz[1]. If certain modes do not change the coupling results, then the tire manufacturer does not need to spend time on increasing the accuracy of certain mode patterns occurring at very high frequencies, outside the target frequency range. The truncation error shall be investigated by excluding modes in the summation solution with a step size of 10 modes cumulatively starting with the maximum number of modes (400 modes, 390 modes, 380 modes etc.). The modes are always included in pairs with positive and negative eigenfrequencies. When for example 100 modes are included it means that the 50 modes belong to the first 50 positive eigenfrequencies and the other 50 modes belong to the first 50 negative eigenfrequencies. Since no new model of the tire system is setup, which describes the dynamic system with for instance only 390 modes, no resonance shifts

[1]This upper frequency limit of 160 Hz is set with respect of the validity of the tire model.

are expected.

5.1.1 Method

To assess the truncation error a reference response function needs to be compared to a modified one, which includes less modes. Unfortunately there are about 16,000 combinations due to

- 7 harmonics
- 6 response DOFs at the bushing
- 400 modes

It would be rather inconvenient to visually compare and later present all combinations to the reference response data set. Therefore an error metric shall be used. By looking into literature one can classify the concepts of assessing a similarity or mismatch between FRFs in to two groups [15], [3]. The first one accesses the mismatch with respect of the mathematical model from which the FRFs were created. For instance in terms of shift of eigenfrequencies, damping properties and modeshapes. Well known is the modal assurance criterion (MAC) presented in [2]. However this approach cannot be applied straight away to data set in this thesis since these modal properties are not known for the coupled solution using a FBS technique. One would need to estimate these parameters trough curve fitting algorithms[2]. The second group of error metrics has no relation to the origin of the FRFs and can be used when dealing with for example measurement data. Within this group one can distinguish whether the error is evaluated at a single frequency or for a frequency band. When assessing the error at a single frequency it turns out that the error metric is very sensitive at minima. When calculating the relative error for instance a small absolute difference in amplitude can lead to a hugh relative error. In addition resonance shift would result in hugh relative errors. For the evaluation over a frequency range it is common practice in acoustics to compare the power inside frequency bands. This avoids problems at minima since the power is mainly determined by the maxima. A critical view to this is that one can have the same power but different curves. Having discussed the error metrics, which are commonly used, none was found without any drawbacks. This gave motivation for creating a new approach not knowing if this error metric will be superior or if there is an existing error metric which has not being found during during the small literature study.

[2] Eigenfrequency shifts could be identified easily by peak picking. However by excluding modes in the summation solution no shifts are expected.

Development of an error metric for assessment of truncation error

The first step for developing an own idea for an appropriate error metric, which should represent the similarity of two different response functions, is to question oneself how one visually come up with a conclusion if the two curves match well or not. By doing so, the following observations are made: First, it is reasonable that the engineer is rather comparing a frequency range, than looking at a single frequency. This is due to the fact that a slight shift of the resonance frequency results in huge errors close to the resonance frequency. In addition it would be too time consuming to compare each frequency. Second, the engineer might try to identify in which frequency ranges the two curves are not matching. This might be done by finding big areas (frequency dimension times magnitude) between two curves. Third, this area needs to be put into a certain relation, for instance to the power inside the considered frequency range of the reference curve. By doing so the data set can be compared to other combinations of reference and modified curves. This idea can be mathematically expressed with the following equation in which $v_\mathrm{T}(\omega)$ and $v_\mathrm{M}(\omega)$ are the frequency dependent velocities of the true and modified curve respectively:

$$\epsilon = \frac{\sum_{\omega=1}^{n} ||v_\mathrm{T}(\omega)|^2 - |v_\mathrm{M}(\omega)|^2|}{\sum_{\omega=1}^{n} |v_\mathrm{T}(\omega)|^2} \tag{5.1}$$

The numerator represents the power between the true and the modified curve, which is depicted with light blue in fig. 5.1. The denominator relates this value to the power of the reference curve, see red dashed lines in the same figure. If one would just conventionally compare the power inside a frequency range it could happen, that the reference curve and the modified curve have the same power although they are different.

The error metrics could be applied to a user defined frequency range. Another idea is to use a floating band. This is depicted in fig. 5.2. Thereby an error value is mapped for a center frequency of a frequency band. In the next step this band is then moved and the error is again evaluated for the center frequency of the new frequency band. The step size in Hz of moving the band determines the frequency resolution that will be obtained for different center frequencies. The interesting idea of this concept is that information before and after the frequency of interest (center frequency) is taken into account. The background to this is that also physically the magnitude of neighbouring frequencies do have a relation to each other or give a meaning. For instance in the mass region the magnitude is increasing and after the resonance frequency the stiffness region starts in which the amplitude is decreasing. With the information that the amplitude at for instance 110 Hz and 112 Hz is lower than at 111 Hz one can conclude that there is a resonance frequency at 111 Hz.

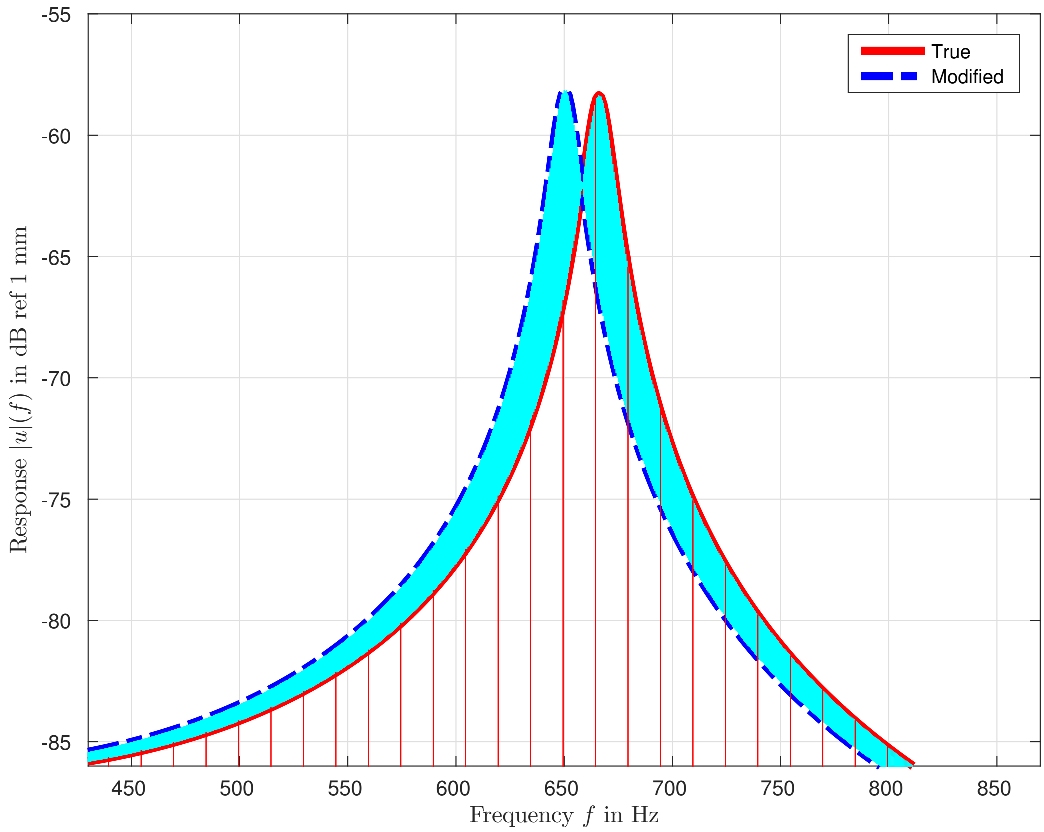

Figure 5.1: Mismatch of power related power of reference response function.

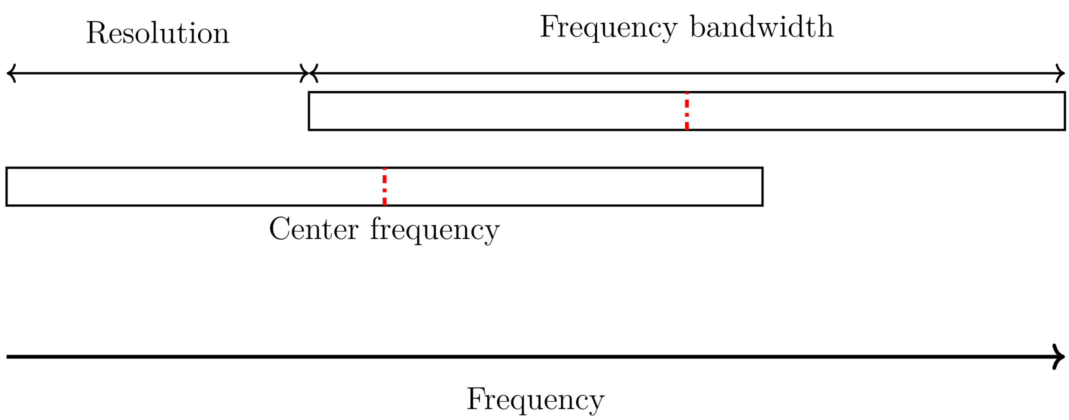

Figure 5.2: Floating frequency bands.

Applicability of error metric to the tire vehicle data set

The concept of the floating band and the error metric is applied on the tire vehicle case. Therefore a bandwidth and a frequency resolution needs to be defined. If the frequency resolution is too coarse, not all information will be included (picket fence effect). If the frequency band is too huge several eigenfrequencies are likely to be inside. It can furthermore happen that at the lower eigenfrequency the reference and modified curve fit perfectly and store a lot of vibration power. If the second natural frequency has a comparably small amplitude and the modified curve does not match adequately, the dissimilarity will not be identified by the error metric in eq. (5.1). This is due to the fact that the numerator relates the power mismatch, which only occurred at the second eigenfrequency, to the total power inside the band, which is mainly determined by the first natural frequency in this example. This ends up in a rather small error value, which does not indicate problems in the predictions near the second natural frequency. If the floating frequency band is rather small (e.g. 3 Hz) the error calculation is similar to the relative difference at a single frequency and the idea to evaluate in a frequency band is getting lost. In addition, one has to be aware of that the SDOF system FRFs of higher order modes are rather constant with small amplitudes at frequencies far below from its natural frequency (see fig. 2.1). Nevertheless at minima a rather high relative difference would be expected, if certain higher order modes are not included. By using a wider frequency band the error calculated in eq. (5.1) becomes smaller at minima, since the mismatch of power is only big very close to the minima but not at lower and higher frequencies, whose amplitudes are much higher. In addition the denominator in eq. (5.1) becomes greater if one evaluates the error around minima with a greater band. Thus, with having a wider frequency band a small sensitivity of the error metric at the anti resonances is expected. This is quite convenient for most applications since it is more interesting to know how accurate the predictions are at frequencies with maximal vibration levels in contrast to frequencies at which the the amplitudes are already small. Having all thoughts regarding the setup of the floating frequency band in mind for this case study a frequency resolution of 1 Hz and a bandwidth of 12 Hz has been chosen.

To demonstrate the practical applicability of the error metric an example is chosen for which the error is calculated for 20 modes to 390 modes increased by 10 modes. It should be mentioned that no error values are obtained in between the step size of 10 modes. An overview is given in fig. 5.3 representing the 5th harmonic in z direction as an example. The error can be seen for any combination of a center frequency and the number of modes. The color bar is limited to values of 0 percent and a maximum of 20 percent[3]. It can be seen that 150 modes are required to ensure that the error is below 20 percent for frequencies up to 160 Hz.

In order to come up with a rough indicator how many modes need to be taken into account to get reasonable vibration predictions for all response DOFs at the bushing the maximum error in the response vector $\mathbf{v}_{\mathrm{ea}}^{*}$ can be determined for each center frequency.

[3] Values above 20 percent are also shown black, the same color as 20 percent.

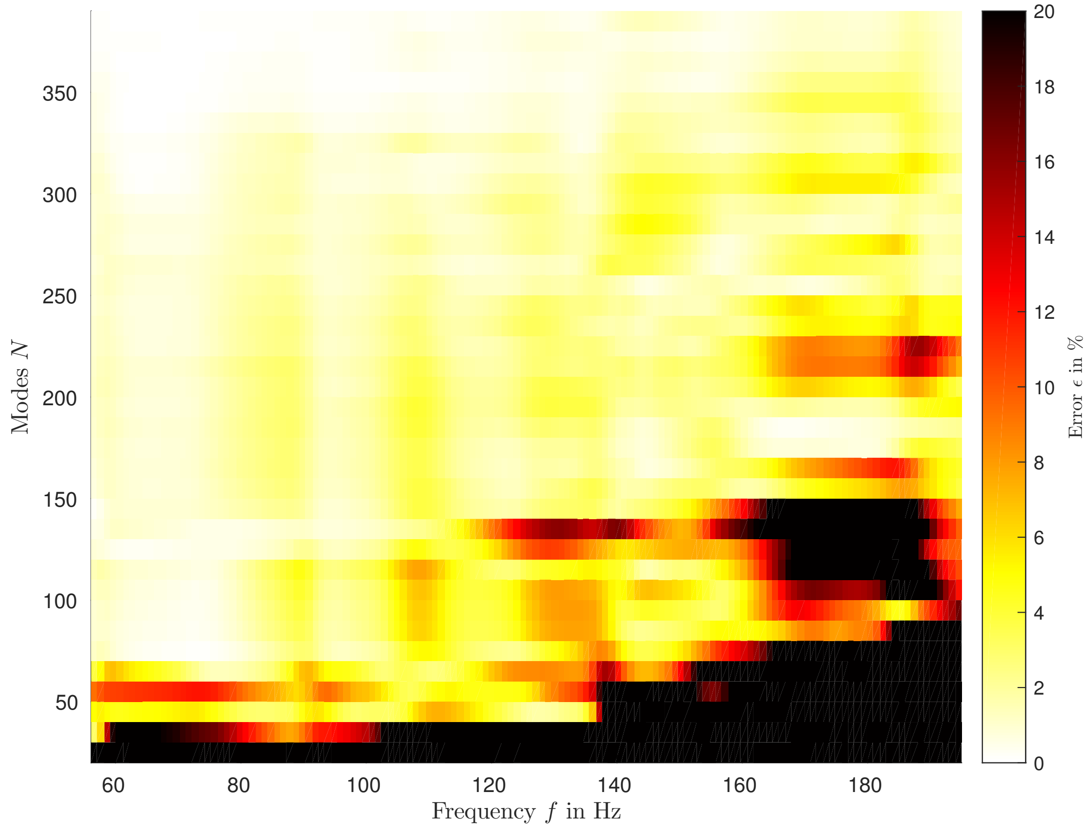

Figure 5.3: Error map for response at the bushing in z direction, 5th harmonic

Validation of error metric

In fig. 5.4 the translational response in z direction depending on the frequency is depicted for the 5th harmonic excitation case. 50 modes, 170 modes and the reference response, which include 400 modes, are depicted. It can be seen that there is no considerable differences between the reference curve and the case with 170 modes over the whole frequency range. By just taking 50 modes into account in the frequency range between 60 Hz and 80 Hz and near the minimum at 90 Hz slight changes can be observed. Related to this, the mismatch is increased from 130 Hz to 150 Hz. Even higher in frequency the two curves do not show much similarity. For instance the anti resonance at 183 Hz can not be seen anymore.

In fig. 5.5 the error depending on the frequency is calculated using the error metrics and the floating band, referring to the case 50 modes, 170 modes and 390 modes. For the case of 170 modes the error is between 1 percent and 3 percent. This is in alignment with the observations made in fig. 5.4. These small deviations will not be seen in a dB scale in the latter figure. By looking at the error for the 50 mode case it can be seen that the error is about 10 percent in the frequency range from 60 Hz to 80 Hz. There is also a peak at 90 Hz with the same value. From 130 Hz the error is increasing from 10 percent to 30 percent at 140 Hz and decreasing to 18 percent at 150 Hz. After 150 Hz the error is increasing up to 200 percent at 180 Hz.

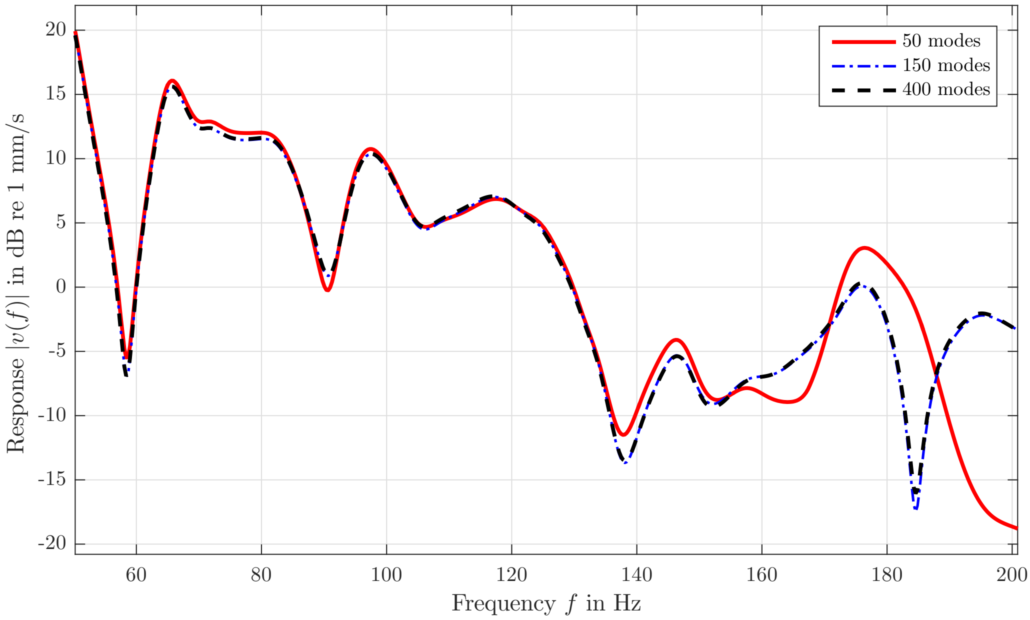

Figure 5.4: Response in z direction at the bushing for different modes included, 5th harmonic

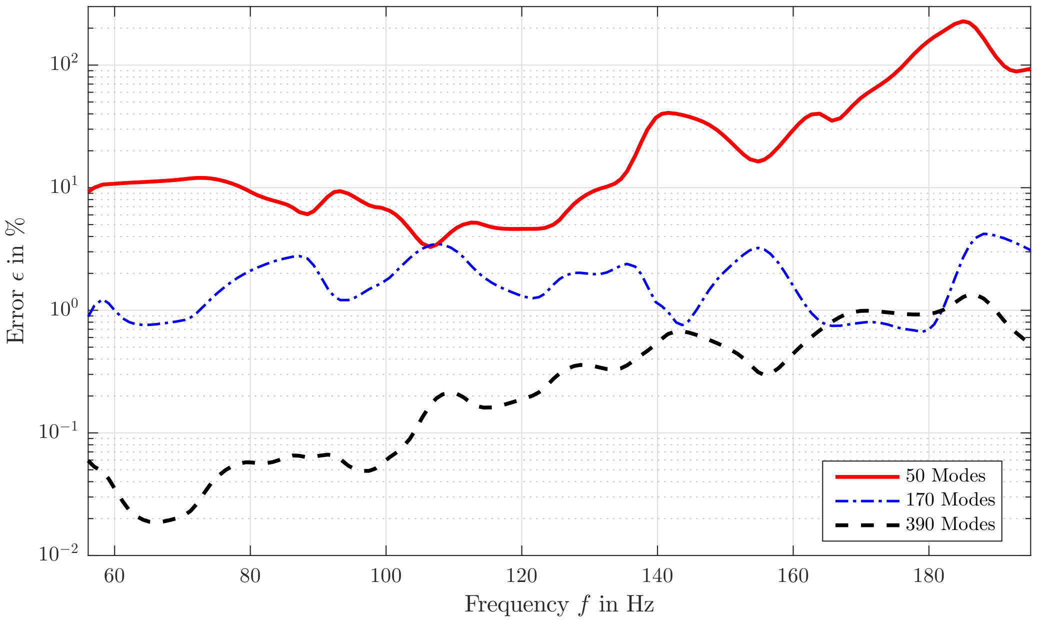

Figure 5.5: Error in z direction at the bushing for different modes included, 5th harmonic

By comparing the observations made from fig. 5.4 and fig. 5.5 it can be concluded that the applied error metric indicates quite well whether two curves are matching or not. In order to obtain reasonable results an error more than 20 percent should not be allowed. The results in z direction are obtained for other load cases can be seen in appendix B. Both the three dimensional error plots and the response predictions in z direction for a chosen number of modes are displayed to further validate the developed error metric (compare fig. B.8 with fig. B.1 to fig. B.7).

5.1.2 Results and discussion

In fig. 5.6 the maximum error in the response vector $\mathbf{v}_{\mathrm{ea}}^{*}$ in dependency of the frequency and the number of modes included in the tire model is displayed in seven sub-figures for all considered excitation cases. Looking at the 1st harmonic it can be seen that the error is at least 20 percent when including 20 modes or 30 modes. Thus these predictions are inaccurate according to previous interpretation of the error values related to fig. 5.4 and fig. 5.5. With 40 modes and more the error is mainly about 5 percent. Small exception can be discovered at around 40 Hz for the case of 70 modes, but the error is not exceeding more than 10 percent, which can be judged as acceptable predictions. From this observation it can be concluded, that the first 40 modes have a great influence in the modal summation solution of the tire model with respect to the 1st harmonic. In other words, if the modes 50 to 400 are not predicted precisely it would not effect the coupled result significantly. For the excitation cases of the 2nd, 3rd and 4th harmonic similar observations can be made, with the difference that the modes 40 to 70 also gain importance. It is not striking that more modes need to be taken into account, since the highest frequency in the frequency range of excitation is increased (see fig. 4.4).

Whereas the first four excitation cases could be modeled with about 70 modes, difficulties occur for the remaining ones. When using more than 70 modes for the 5th harmonic the frequencies up to 120 Hz can be modelled well allowing errors of 5 percent. Then at least 250 modes are required to represent the dynamic behaviour over 130 Hz. With 300 modes the error is finally smaller than 5 percent. This very remarkable and unexpected observation, which indicates, that a new physical effect gets important. It could be that the wavelength in the mode pattern of the tire reaches the dimension of the tire patch, where the excitation takes place. One should be aware of that the spatial distribution of the force determines which modes are excited or not. When the wavelength of the modes is very large in relation to the dimensions of the tire patch the spatial distribution is not that important and the excitation can be simply seen as a point excitation. In this case the behaviour can be modeled with a rather small amount of modes. However this might not be the case anymore when the dimensions of the tire patch reach the wavelength of modes. To capture this phenomenon many modes are required. Similar observations can be seen for the 6th and 7th harmonic where 70 modes can represent the dynamic behaviour up to 130 Hz and 160 Hz respectively. However 340 modes are required for higher frequencies in both cases.

Comparing the errors in the same frequency range for different harmonics in fig. 5.6, it can be seen that the errors are not necessary similar. This is due to the system properties of the tire that are speed dependent and different harmonics have different operating points at the same frequency (see fig. 4.4).

As another general remark it should be mentioned that by including more modes, the coupled result is not necessarily better. This occurs for instance in the frequency range from 40 Hz to 55 Hz by comparing the error between 120 modes and 130 modes referring to the 2nd harmonic seen in fig. 5.6. This is from the mathematical point of view not striking, if one recaptures that the FRF is synthesized through a bunch of SDOF systems (see fig. 2.1). The modal amplitude belonging to one SDOF system can have a positive or a negative value. It can happen that first a synthesized FRF from a certain number of modes is constructed in way that it represents the behaviour correctly. By adding another SDOF system FRF, which e.g. has a negative modal amplitude, an inaccurate synthesized FRF can be obtained. By including more SDOF system FRFs with positive modal amplitude the correct synthesized FRF is obtained again. Another less likely explanation is that the error metric only evaluates the magnitude and not the phase information. The same magnitude can be obtained for different combination of real and imaginary parts for instance.

Last but not least it should be pointed out that fig. 5.6 is a pessimistic guidance since it takes the maximum error for center frequency out of six response DOFs. When looking at a specific response DOF the error can be smaller. As an example the three dimensional error plot for the z direction can be seen in fig. 5.7 and compared to fig. 5.6. By e.g. looking at the 6th harmonic it can be seen, that 70 modes instead of 340 modes are needed to ensure an error below 20 % for frequencies below 160 Hz for the z DOF and for all DOFs respectively.

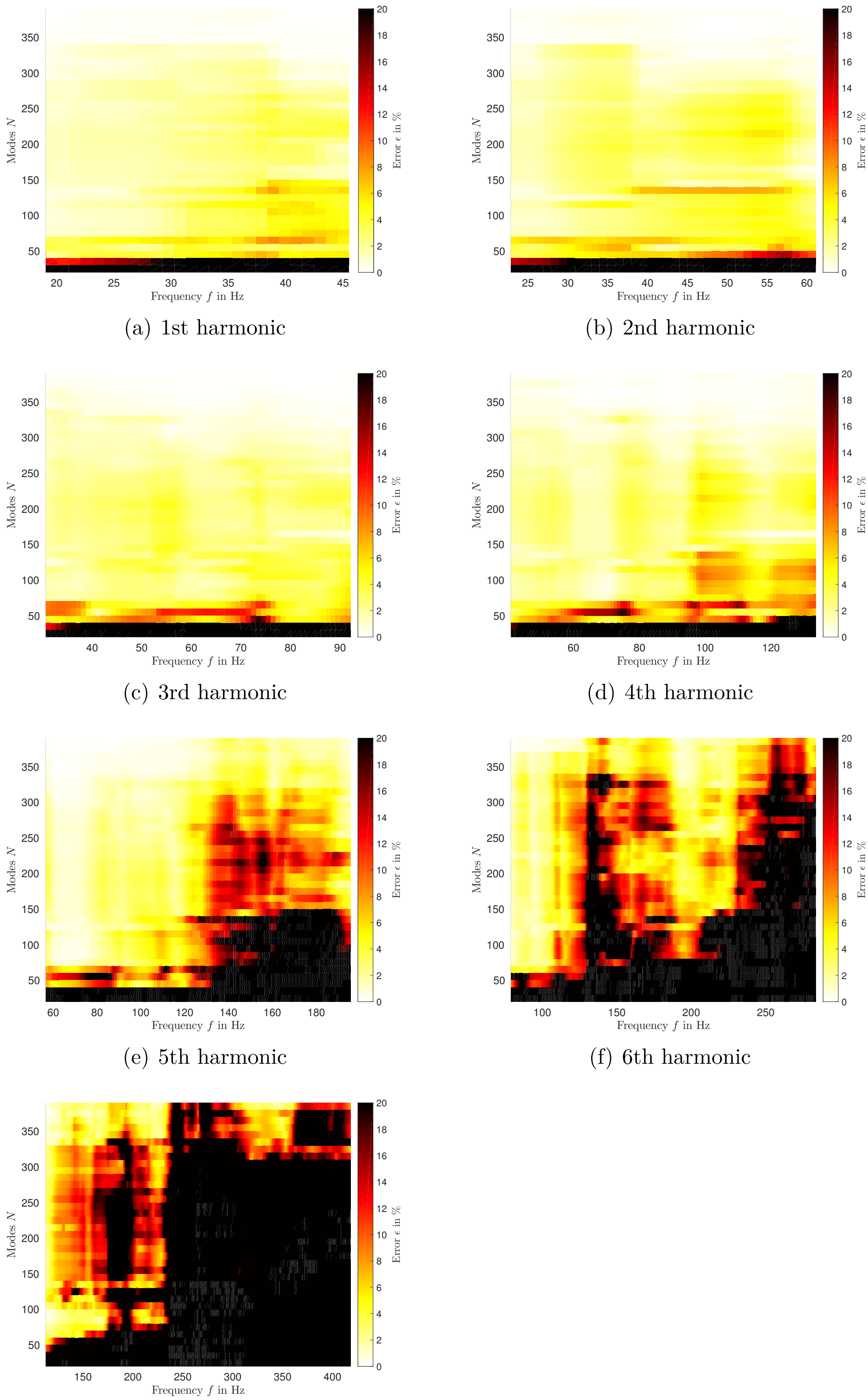

(a) 1st harmonic

(b) 2nd harmonic

(c) 3rd harmonic

(d) 4th harmonic

(e) 5th harmonic

(f) 6th harmonic

(g) 7th harmonic

Figure 5.6: Maximum truncation error in $\mathbf{v}_{\mathrm{ea}}^{*}$ for different harmonics.

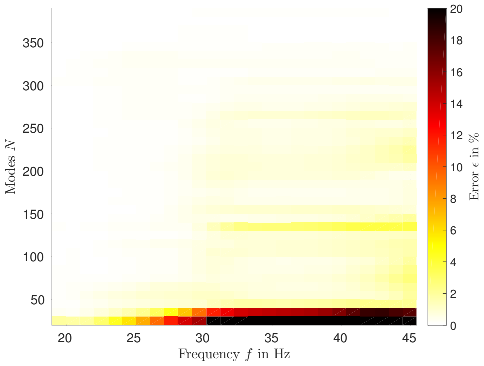

(a) 1st harmonic

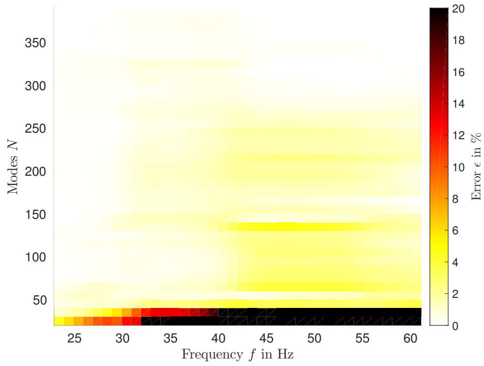

(b) 2nd harmonic

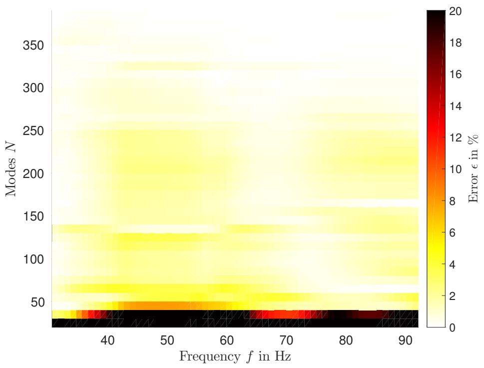

(c) 3rd harmonic

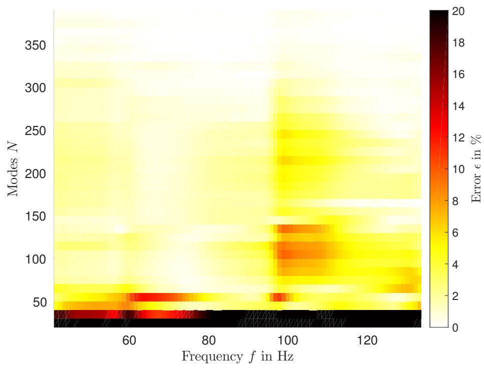

(d) 4th harmonic

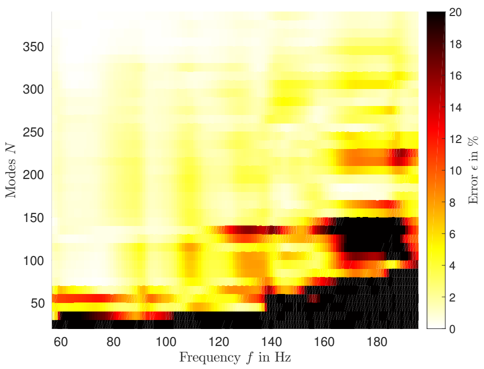

(e) 5th harmonic

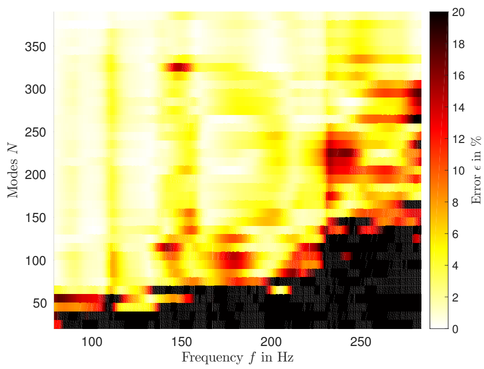

(f) 6th harmonic

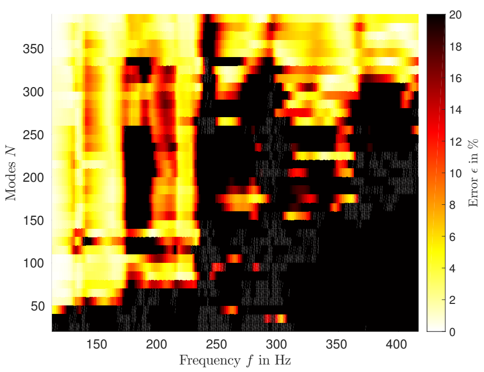

(g) 7th harmonic

Figure 5.7: Truncation error for z DOF in $\mathbf{v}^*_{\mathrm{ea}}$ for different harmonics

After obtaining the results of how many modes are required for each excitation case it is interesting to know how high is the belonging eigenfrequency of the suggested number of modes. Therefore the modes from 10 modes to 400 modes in the step size of 10 modes are related to the eigenfrequency in fig. 5.8. Since the dynamic properties of the tire model changes over speed the natural frequency belonging to a certain number of mode are displayed for the operating points of 20 km/h, 80 km/h and 120 km/h. In addition, from this figure the modal density can be roughly estimated. For instance the 10th natural frequency is at 20 Hz whereas the 20th one is at 90 Hz. This means on average that every 7 Hz a natural frequency is expected. Looking higher in frequency the modal density is increased, for instance two eigenfrequencies per Hz at the frequency range 200 Hz to 220 Hz. Interesting to observe is the fact that the eigenfrequencies belonging to the modes from 380 to 400 are spread out (roughly 500 Hz to 900 Hz). The modal density is very low. From the physical point of view it is not reasonable to expect this behaviour. The latter observation is rather explained with the coarse discretization in the FEM model of the tire.

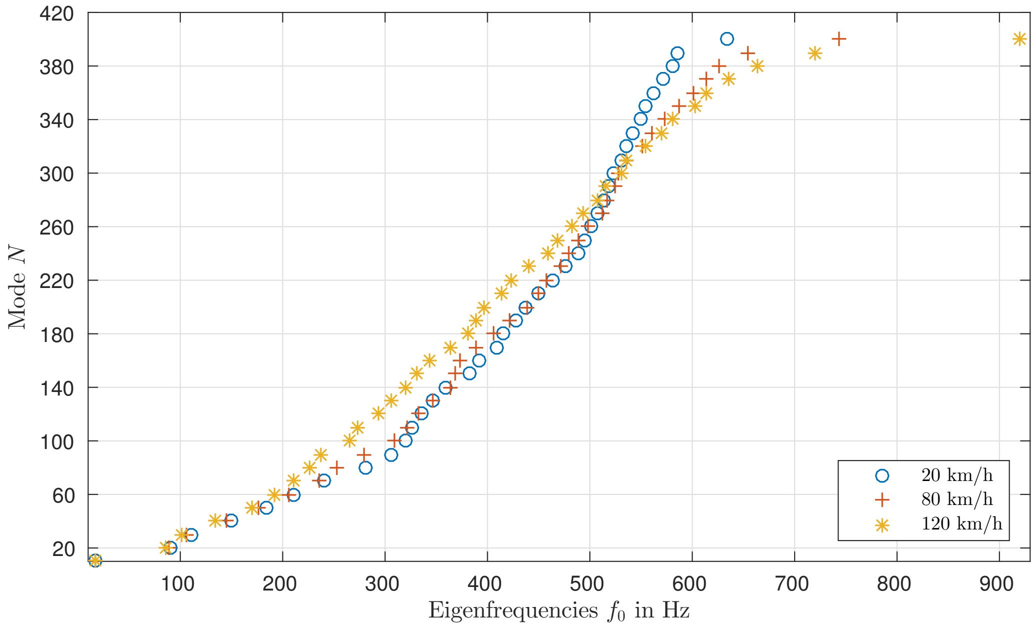

Figure 5.8: Belonging eigenfrequencies to number of modes.

In order to sum up the results of the modal truncation error investigation with seven different harmonic excitation cases, table 5.1 is created. The suggested number of modes and the highest eigenfrequency from the set of suggested modes are displayed for predictions up to 130 Hz and 160 Hz. In addition this information is set in context of the frequency range of the seven excitation cases. The following key observations can be made. First, the highest frequency in the frequency range of the first harmonic is 51.5 Hz. The corresponding highest natural frequency of the suggested number of 40 modes is 144 Hz. The latter number is almost three times higher than the upper border of the frequency range of interest with 51.5 Hz. Second, when using 70 modes predictions give good results for all considered excitation cases in the frequency range up to 130 Hz. Predictions up to 160 Hz demands a greater effort for the excitation cases of the 5th, 6th and 7th harmonic, here up to 340 modes are required. But at this point one should have the observations regarding the limitations of the tire model. The tire manufacture argues that the provided tire model is only trustful until 160 Hz. The highest frequency in the frequency range of the 5th harmonic is already 200 Hz. Thus the results of this sensitivity study of the 5th to 7th harmonics include uncertainties. It could be e.g. that the higher order modes do have actually a higher or lower amplitude, which would lead to different conclusions regarding the influence of them in the modal summation solution. Nevertheless it gives reasons to believe that for these excitation cases the vibrating wavelength in the tire reaches the scales of the excitation. In literature this problem is also addressed in reference [1].

Table 5.1: Suggested number of modes for different excitation cases.

Name of harmonic	1.	2.	3.	4.	5.	6.	7.
Excitation frequencies							
Lowest frequency in Hz	12.9	16.7	24.6	34.8	50.2.9	72.1	105.6
Highest frequency in Hz	51.5	67	97.9	139	200	288.1	422.3
Suggested number of modes							
up to 130 Hz	40	40	50	60	70	70	60
up to 160 Hz	40	40	50	60	270	340	130
Eigenfrequency in Hz.[4]							
up to 130 Hz	144	144	176	206	236	236	206
up to 160 Hz	144	144	176	206	511	573	347

5.2 Random noise introduced to tire and chassis model

This sensitivity study aims to give an example of how the coupled solution can be affected by random noise introduced to the uncoupled subsystems. Noise in measurement data is well known to cause problems when coupling subsystems. Another motivation for this study is that, there are so many systematic error sources in the tire and the vehicle model. At this point imprecision in the material, geometry of components and their connection can be mentioned as possible errors. Since any kind of combination of errors might happen, random noise shall be introduced to all DOFs in the FRF matrix of the subsystems. In the end a noise corridor or scatter band shall be obtained. With this stochastic approach predictions can be made

[4]Highest eigenfrequency from the set of suggested modes at the operation point of 80 kph.

in which range the results are expected, regardless which error source has caused a deviation in the FRFs. However one has to be aware of that no information is obtained with respect to which shape the FRF will have inside the noise corridor.

5.2.1 Method

This study introduces noise to the FRFs and responses functions through a scaling matrix with a random uniform distributed noise, $\mathbf{S}$, in the range of 0 % to ±10 % to all DOFs of either a single subsystem or both subsystems as follows:

Noise in the tire model:

$$\mathbf{v}_{\mathrm{e}}^{*} = \mathbf{Y}_{\mathrm{ea}}^{*}\mathbf{F}_{\mathrm{a}} = \mathbf{Y}_{\mathrm{ej}}^{\mathrm{E}}\left[\mathbf{S}\otimes\mathbf{Y}_{\mathrm{jj}}^{\mathrm{A}} + \mathbf{Y}_{\mathrm{jj}}^{\mathrm{E}}\right]^{-1}\mathbf{S}\otimes\left[\mathbf{Y}_{\mathrm{ja}}^{\mathrm{A}}\mathbf{F}_{\mathrm{a}}\right] \tag{5.2}$$

Noise in the vehicle model:

$$\mathbf{v}_{\mathrm{e}}^{*} = \mathbf{Y}_{\mathrm{ea}}^{*}\mathbf{F}_{\mathrm{a}} = \mathbf{S}\otimes\mathbf{Y}_{\mathrm{ej}}^{\mathrm{E}}\left[\mathbf{Y}_{\mathrm{jj}}^{\mathrm{A}} + \mathbf{S}\otimes\mathbf{Y}_{\mathrm{jj}}^{\mathrm{E}}\right]^{-1}\mathbf{Y}_{\mathrm{ja}}^{\mathrm{A}}\mathbf{F}_{\mathrm{a}} \tag{5.3}$$

Noise in both vehicle and tire model:

$$\mathbf{v}_{\mathrm{e}}^{*} = \mathbf{Y}_{\mathrm{ea}}^{*}\mathbf{F}_{\mathrm{a}} = \mathbf{S}\otimes\mathbf{Y}_{\mathrm{ej}}^{\mathrm{E}}\left[\mathbf{S}\otimes\mathbf{Y}_{\mathrm{jj}}^{\mathrm{A}} + \mathbf{S}\otimes\mathbf{Y}_{\mathrm{jj}}^{\mathrm{E}}\right]^{-1}\mathbf{S}\otimes\left[\mathbf{Y}_{\mathrm{ja}}^{\mathrm{A}}\mathbf{F}_{\mathrm{a}}\right] \tag{5.4}$$

The scaling matrix $\mathbf{S}$ is created with the dimension of the FRF matrix or response matrix of the considered subsystems and its values vary between 0.9 and 1.1. Each element in the original FRF or response matrix is then multiplied with a corresponding error element in the scaling matrix $\mathbf{S}$. The frequency dependent response at the bushing is calculated 10 000 times using randomly created scaling matrices. Out of these calculations the maximum and minimum values at each frequency are used to determine the upper and lower boarder of the noise corridor. The number of runs has been chosen in a way that the corridor borders stopped changing significantly. In order to get a rough idea of how a polluted coupling result could look inside the scatter band, two different calculations procedures are performed. In the first approach the scaling matrix is frequency independent. This means practically that the FRFs and response functions are shifted either upwards or downwards. In a second approach a different scaling matrix is used for each frequency. Especially the latter scenario could be very meaningful since this is imitating the case of measurement or numerical noise. The implemented Matlab code for the calculations allows to look at the chosen iteration and see how a single polluted response function lies in between the noise corridors borders with the previous described calculation procedures.

5.2.2 Results and discussion

Only the case where noise is introduced to both subsystems is discussed in the thesis. Graphs for the coupled system for noise introduced into the tire subsystem and the chassis subsystem separately can be seen in appendix C. In fig. 5.9 the noise corridor with introduced errors in both tire and vehicle model is displayed for the response in z-direction for the 4th harmonic. In between the maximum and minimum borders of the scatter band the original unpolluted coupling results are plotted as a reference. The scatter band boarders keeps at a rather steady level of ±5 dB from the non-polluted reference curve over the major part of the frequency range, except for frequency ranges that show a minima. Here, the border can deviate up to 33 dB below the reference curve. At 42 Hz a peak of +20 dB can be seen compared to the reference curve. It is quite surprising that small changes of 10 % can lead to a 20 dB difference. Explanations can be found from the mathematical point of view. When adding 10 % noise to each subsystem possible noise combinations allow already ±20 % in the inverted matrix. As discussed in section 2.2.2 an error in one element can spread errors to the whole matrix of the coupled solution. If errors are in several or even all elements of the inverted matrix huge errors can be seen in the coupling result.

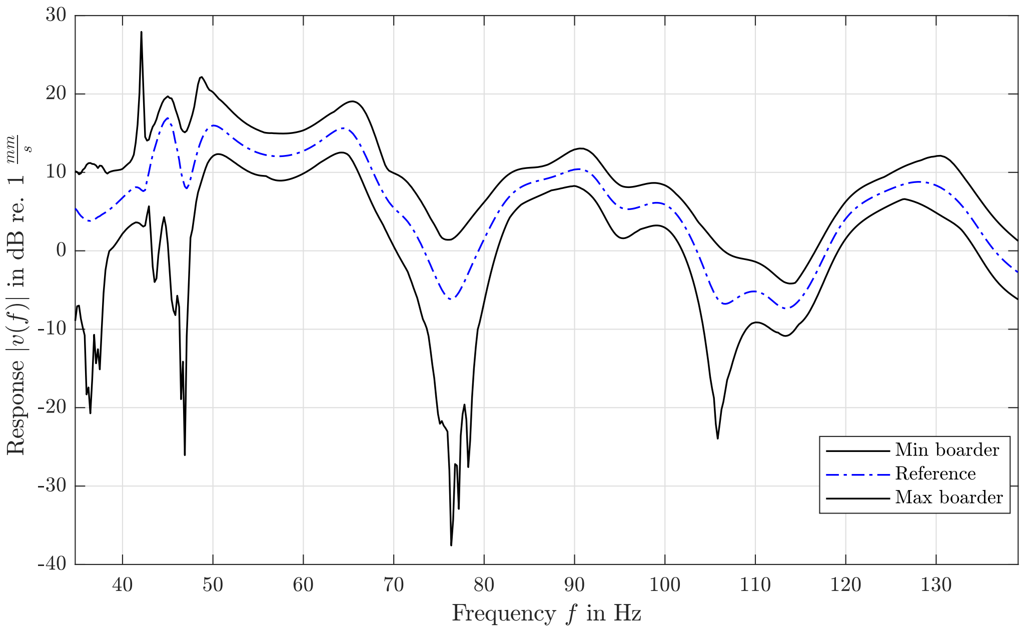

Figure 5.9: Scatter band for noise in tire and vehicle model between 0 and ±10 %

In fig. 5.10 a response function created by a single frequency independent scaling matrix is added to the setup in fig. 5.9. It is a specific response function, which belongs to the scaling matrix that has caused the huge peak at 42 Hz in fig. 5.9. The deviation to the reference curve is about +15 dB at 42 Hz and -18 dB at 45 Hz, since the eigenfrequency has been shifted from 45 Hz to 42 Hz. This peak at 42 Hz is much sharper than the one in the original setup at 45 Hz. Apart from the exception occurring between 40 Hz and 50 Hz the modified curve sticks rather close and smooth to the reference curve.

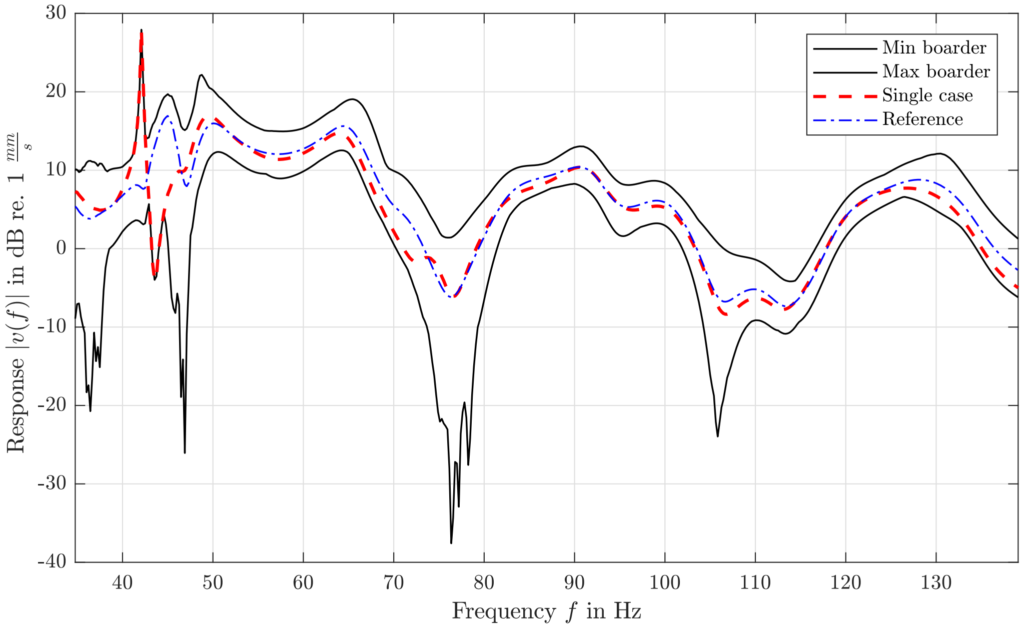

Figure 5.10: Possible prediction inside scatter band caused by frequency independent scaled FRFs and response functions

In fig. 5.11 the second calculation procedure with having a frequency dependent scaling matrix is used to plot a possible response function. This could imitate measurement noise. As well as in fig. 5.10 this special polluted response function is chosen in a way that it causes a peak at 42 Hz. The latter function is fluctuating around the reference curve. High differences to the reference curve can be seen at 42 Hz. This fluctuation (pseudo resonance) is so high that it could be false interpreted as a natural frequency [21]. The noise corridor calculated this time from the polluted FRFs and response with a frequency dependent scaling matrix looks less smooth as the one in fig. 5.10. However similar borders are obtained. This is due to the fact that in both calculation a bunch of random scaled matrices have been used to calculate coupling results at a certain frequency.

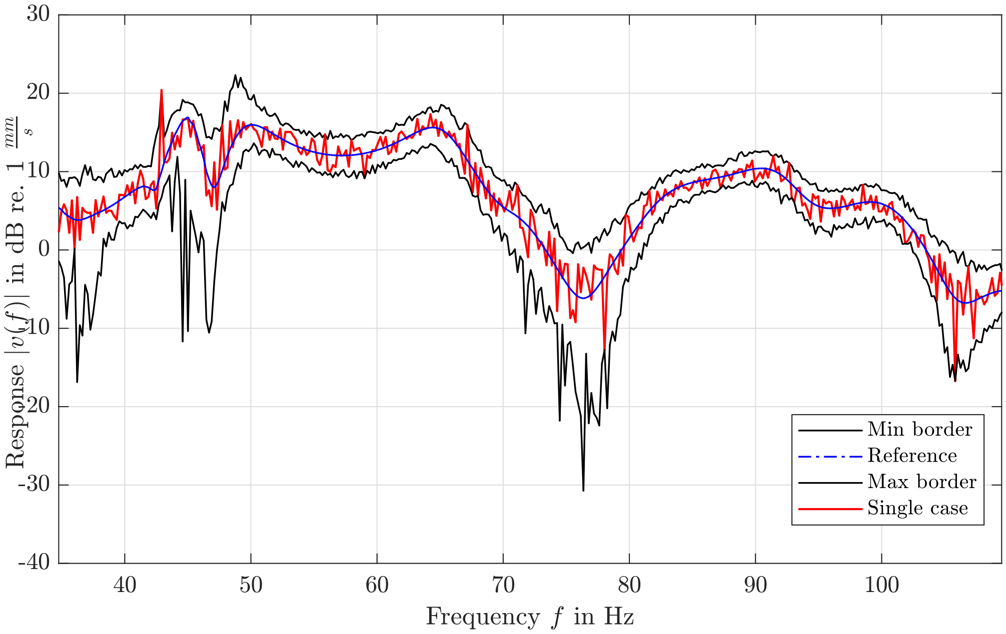

Figure 5.11: Possible prediction inside scatter band caused by frequency dependent scaled FRFs and response functions

6 Conclusion

By using the Receptance Coupling Method a modal tire model has been assembled in the frequency domain to the rear chassis model of a car to predict vibrations at a chosen node near a bushing due to an excitation at the tire path.

Seven different harmonic load cases have been used, that are imitating the roughness of a road surface. Two main questions have been under study. Modal truncation errors of the tire model have been investigated to find out how important higher order modes outside the considered frequency range are for the prediction of a tire vehicle assembly up to 160 Hz. Also a sensitivity study of how random errors in the subsystems tire and vehicle affect the coupling result has been conducted.

For the purpose of the modal truncation study of the tire model an error metric has been developed, which uses a floating frequency band and assesses the similarity between two FRFs by relating the power of mismatch to the power under the reference curve. This approach has found to be appropriate and was used for displaying the dependency of the number of modes needed for an accurate prediction of the coupled solution and the considered frequency for each of the seven harmonic excitation cases. The results reveal, that the influence of higher order modes depends strongly on the excitation case, which itself is a function of frequency and vehicle speed. In addition the spatial distribution of the force at the tire patch might also influence the number of modes, that are required for accurate predictions. This might be a reason why modes with eigenfrequencies of 573 Hz are needed for predictions up to 160 Hz.

In order to investigate what influence errors in the subsystems tire and vehicle have on the coupled solution, a statistical approach has been chosen, in which the transfer and response function were scaled with random noise between ± 10 %. Thereby a noise corridor (or scatter band) has been obtained for a chosen excitation case and response degree of freedom at the bushing. The results show a noise corridor, which upper and lower boarders have a difference of about $\pm$ 5 dB for the major part of the frequency range. Deviations of about 20 dB from the non-polluted reference have been spotted close to minima and natural frequencies.

7

Suggestions of future studies

In this Master's thesis one tire has been coupled to vehicle chassis. In the next step all tires could be taken into account. The provided theory about the Generalized Receptance Coupling Method might be of great help for this. The predictions could then be validated with measurement data. It would also be beneficial to visualize the mode-shapes of the coupled structure by using a Component Mode Synthesis coupling technique or apply a parameter estimation to the coupled FRFs.

With respect to the two sensitivity studies that were performed, the following future work can be suggested. With the modal truncation investigations of the tire model an overview has been given for the importance of high order modes. However one could look more in detail to a chosen excitation case and response degree of freedom and find out, which modes are important for this specific case. Furthermore, the modal truncation investigation can be also performed in a similar way with the vehicle data. With respect to the investigation of errors in the subsystems tire and vehicle, further studies can be performed. Since it has been shown that the coupled system can be very sensitive one need to find out if and under which circumstances numerical errors cause problems during the matrix inversion. By a further literature study and awareness of the used algorithm in Matlab a threshold for round of errors could be defined. Apart from that, simultaneous change of physical properties such as mass and stiffness or geometry of components could be next field of investigation, in which a noise corridor for systematic errors could be obtained.

Bibliography

[1] T. J. S. Abrahamsson et al. "Calibration and Validation of a Car Subframe Finite Element Model Using Frequency Responses". In: *Topics in Modal Analysis, Volume 10*. Ed. by Michael Mains. DOI: 10.1007/978-3-319-15251-6_2. Cham: Springer International Publishing, 2015, pp. 9–22. ISBN: 978-3-319-15250-9 978-3-319-15251-6.

[2] Randall J. Allemang and David L. Brown. "A correlation coefficient for modal vector analysis". In: *Proceedings of the 1st international modal analysis conference*. Vol. 1. Orlando: Union College Press, 1982, pp. 110–116.

[3] H. Sezer Atamturktur et al., eds. *Model Validation and Uncertainty Quantification, Volume 3*. Conference Proceedings of the Society for Experimental Mechanics Series. DOI: 10.1007/978-3-319-15224-0. Cham: Springer International Publishing, 2015. ISBN: 978-3-319-15223-3 978-3-319-15224-0.

[4] R. L. Campbell and S. A. Hambric. *Application of Frequency Domain Substructure Synthesis Technique for Plates Loaded with Complex Attachments*. Tech. rep. DTIC Document, 2004.

[5] Robert L. Campbell and Carl M. Pray. *Substructure Synthesis Methods and Their Application to Structural-Acoustic Simulations*. Tech. rep. DTIC Document, 2005.

[6] Brian Y. Cho. *Spindle Load Application for NVH CAE Models by Using Principal Vector Approach*. Tech. rep. SAE Technical Paper, 2005.

[7] T. Clarke, S. J. Griffin, and J. Ensor. "Output Feedback Eigenstructure Assignment Using a New Reduced Orthogonality Condition". In: *International Journal of Control* 76.4 (2003), pp. 390–402.

[8] K. Cuppens, Paul Sas, and L. Hermans. "Evaluation of the FRF Based Substructuring and Modal Synthesis Technique Applied to Vehicle FE Data". In: *Proceedings of The International Seminar on Modal Analysis*. Vol. 3. KU Leuven; 1998, 2001, pp. 1143–1150. (Visited on 01/20/2017).

[9] Brian H. Dalton and David G. Behm. "Effects of noise and music on human and task performance: A systematic review". In: *Occupational Ergonomics* 7.3 (2007), pp. 143–152.

[10] Dennis de Klerk, Daniel J. Rixen, and Jasper de Jong. "Frequency Based Substructuring (FBS) Method Reformulated According to the Dual Domain Decomposition Method". English. In: St. Louis, MO: Delft University of Technology, 2006.

[11] D. J. Ewins. *Modal Testing: Theory, Practice, and Application*. 2nd ed. Mechanical engineering research studies 10. Baldock, Hertfordshire, England ; Philadelphia, PA: Research Studies Press, 2000. ISBN: 978-0-86380-218-8.

[12] L. R. Hartley and T. Williams. "Steady State Noise and Music and Vigilance". en. In: *Ergonomics* 20.3 (May 1977), pp. 277–285. ISSN: 0014-0139, 1366-5847. DOI: 10.1080/00140137708931627.

[13] Bjorn Jetmundsen, Richard L. Bielawa, and William G. Flannelly. "Generalized Frequency Domain Substructure Synthesis". In: *Journal of the American Helicopter Society* 33.1 (1988), pp. 55–64. ISSN: 2161-6027. DOI: 10.4050/JAHS.33.55.

[14] Bjorn Jetmundsen, Richard L. Bielawa, and William G. Flannelly. "Generalized Frequency Domain Substructure Synthesis". In: *Journal of the American Helicopter Society* 33.1 (1988), pp. 55–64.

[15] Anders T. Johansson, Thomas JS Abrahamsson, and F. V. Keulen. "Comparison of Several Error Metrics for FE Model Updating". In: *Proceedings of the 25th International Modal Analysis Conference (IMAC-XXV), Orlando, FL, Feb.* 2007, pp. 19–22.

[16] Genuit Klaus. "The sound of quality of vehicle interior noise: a challange for the NVH-engineers". In: *Int. J. Vehicle Noise and Vibration, Vol.1, Nos. 1/2, 2004* (2004).

[17] D. De Klerk, D. J. Rixen, and S. N. Voormeeren. "General Framework for Dynamic Substructuring: History, Review and Classification of Techniques". en. In: *AIAA Journal* 46.5 (May 2008), pp. 1169–1181. ISSN: 0001-1452, 1533-385X. DOI: 10.2514/1.33274.

[18] D. De Klerk, D. J. Rixen, and S. N. Voormeeren. "General Framework for Dynamic Substructuring: History, Review and Classification of Techniques". en. In: *AIAA Journal* 46.5 (May 2008), pp. 1169–1181. ISSN: 0001-1452, 1533-385X. DOI: 10.2514/1.33274.

[19] Y. Ren and C. F. Beards. "On Substructure Synthesis with FRF Data". In: *Journal of Sound and Vibration* 185.5 (1995), pp. 845–866.

[20] MAREN Scheel. "State-Space Experimental-Analytical Dynamic Substructuring Using the Transmission Simulator". PhD thesis. M. Sc. thesis, University of Stuttgart, 2015.

[21] Antonio Paulo Vale Urgueira. "Dynamic Analysis of Coupled Structures Using Experimental Data". PhD thesis. University of London, 1989.

[22] Peter Zeller, ed. *Handbuch Fahrzeugakustik: Grundlagen, Auslegung, Berechnung, Versuch ; mit 85 Tabellen*. ger. 2., überarb. Aufl. ATZ/MTZ-Fachbuch. OCLC: 844947056. Wiesbaden: Vieweg + Teubner, 2012. ISBN: 978-3-8348-1443-2.

A

Prediction of vibrations at the bushing - Reference

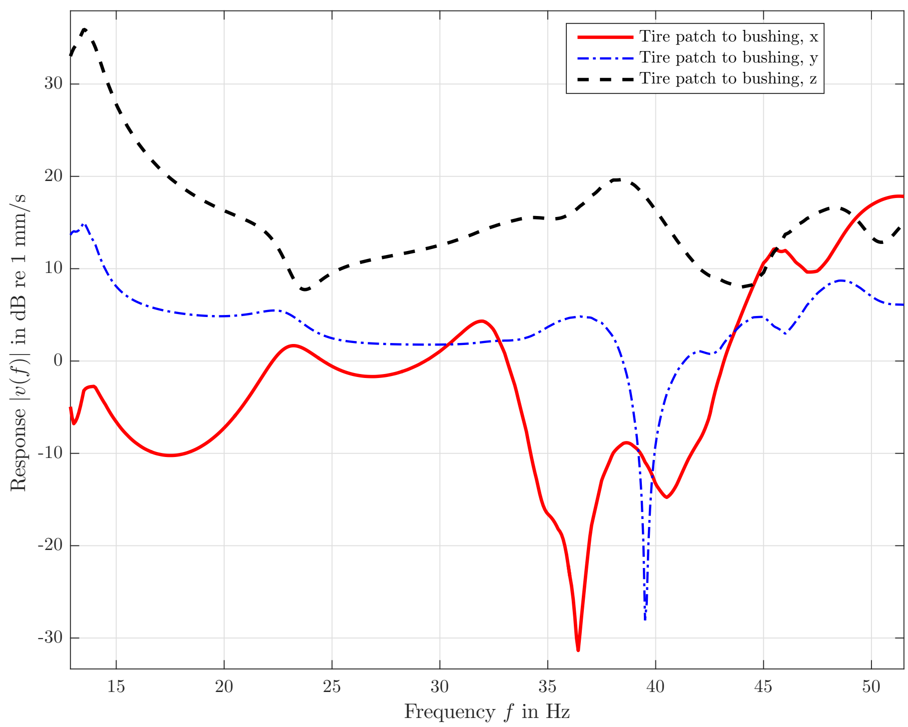

Figure A.1: Translational response at the bushing, 1st harmonic

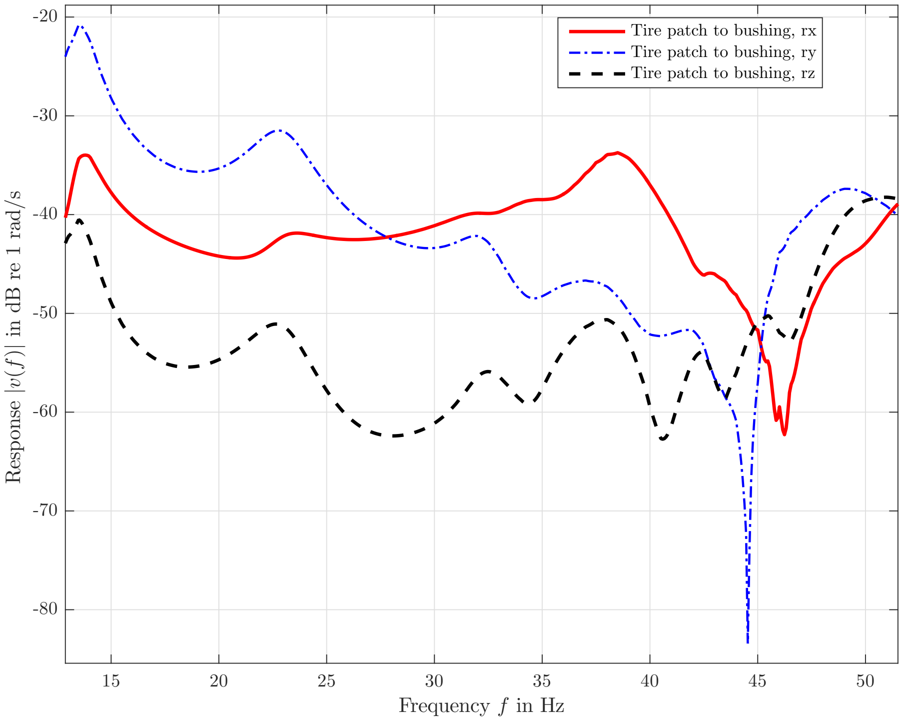

Figure A.2: Rotational response at the bushing, 1st harmonic

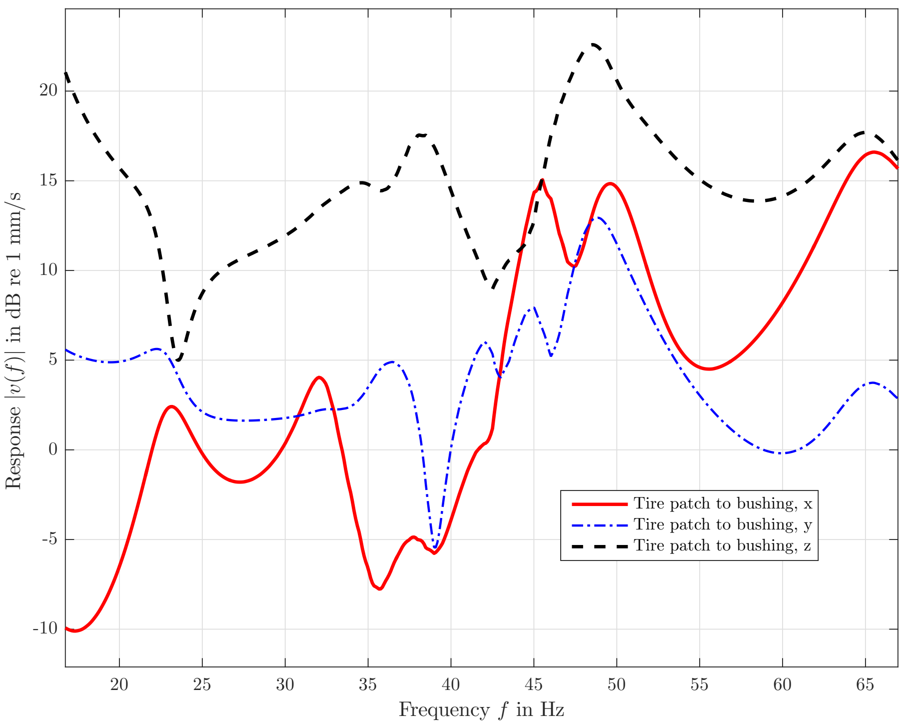

Figure A.3: Translational response at the bushing, 2nd harmonic

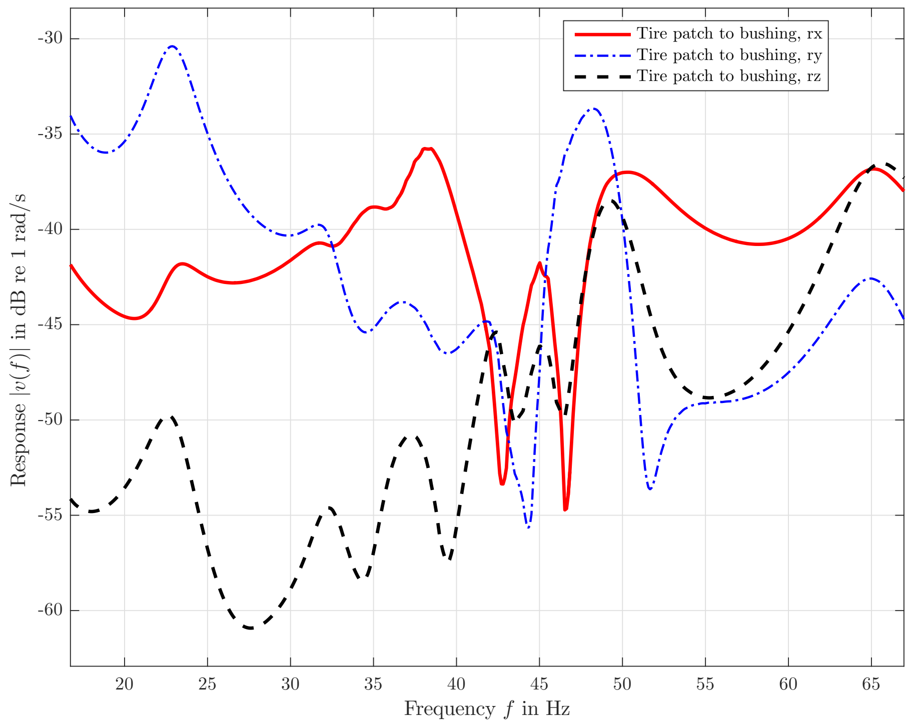

Figure A.4: Rotational response at the bushing, 2nd harmonic

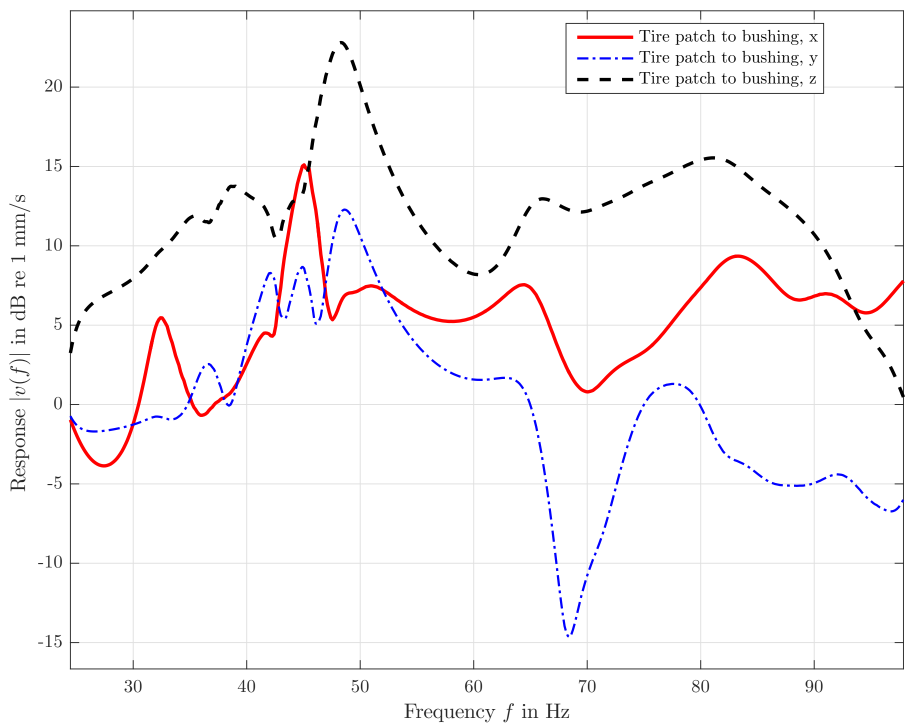

Figure A.5: Translational response at the bushing, 3rd harmonic

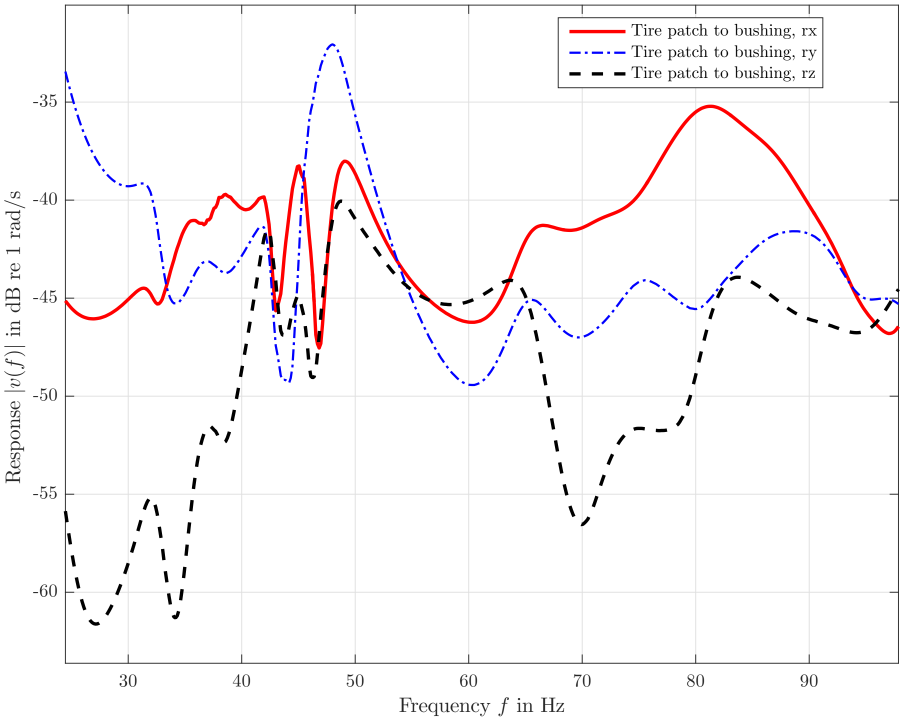

Figure A.6: Rotational response at the bushing, 3rd harmonic

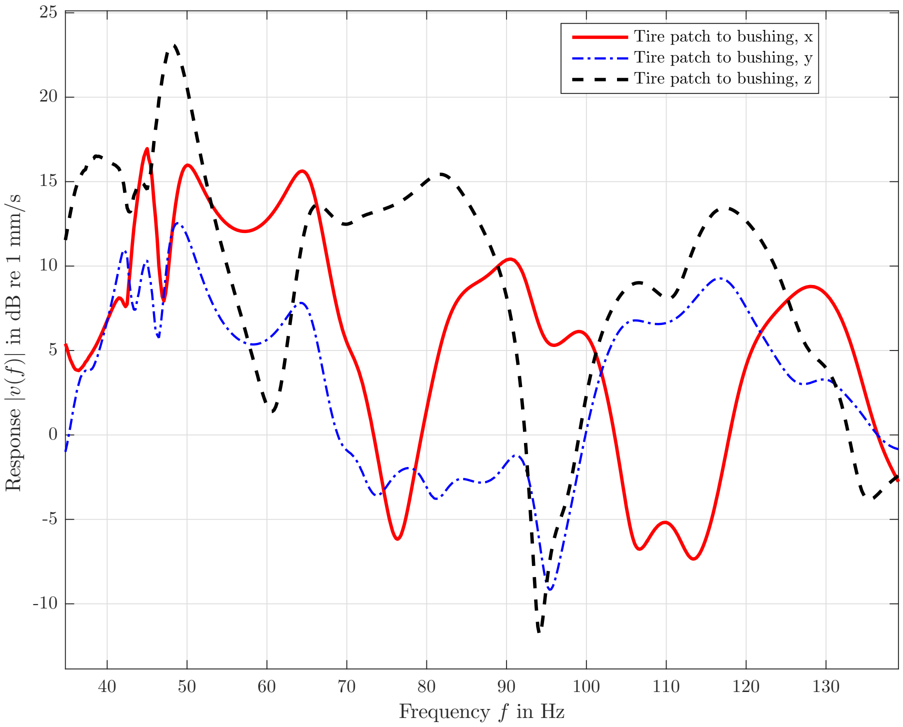

Figure A.7: Translational response at the bushing, 4th harmonic

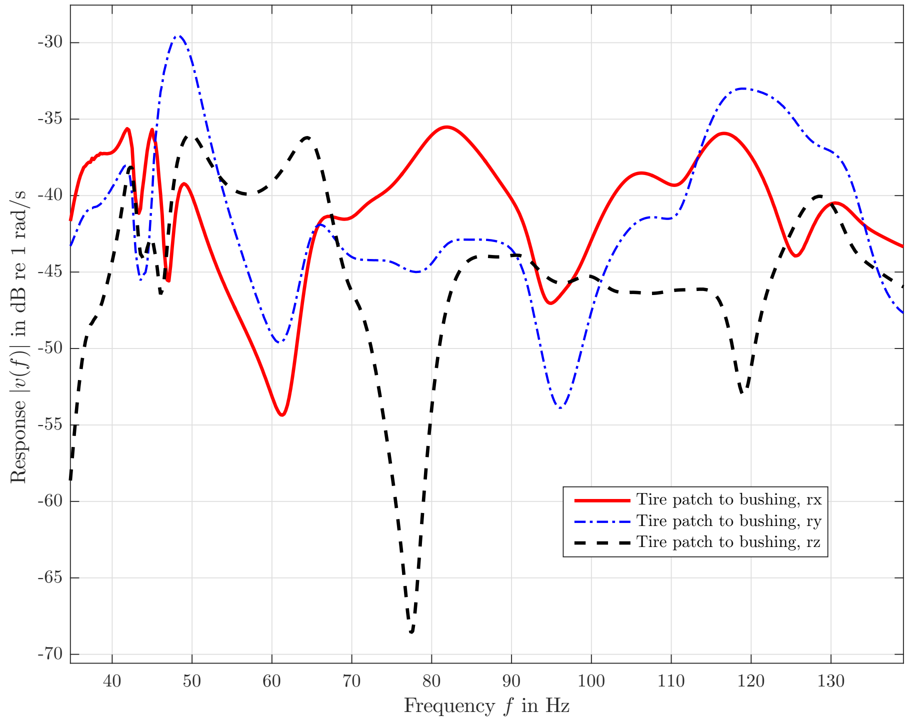

Figure A.8: Rotational response at the bushing, 4th harmonic

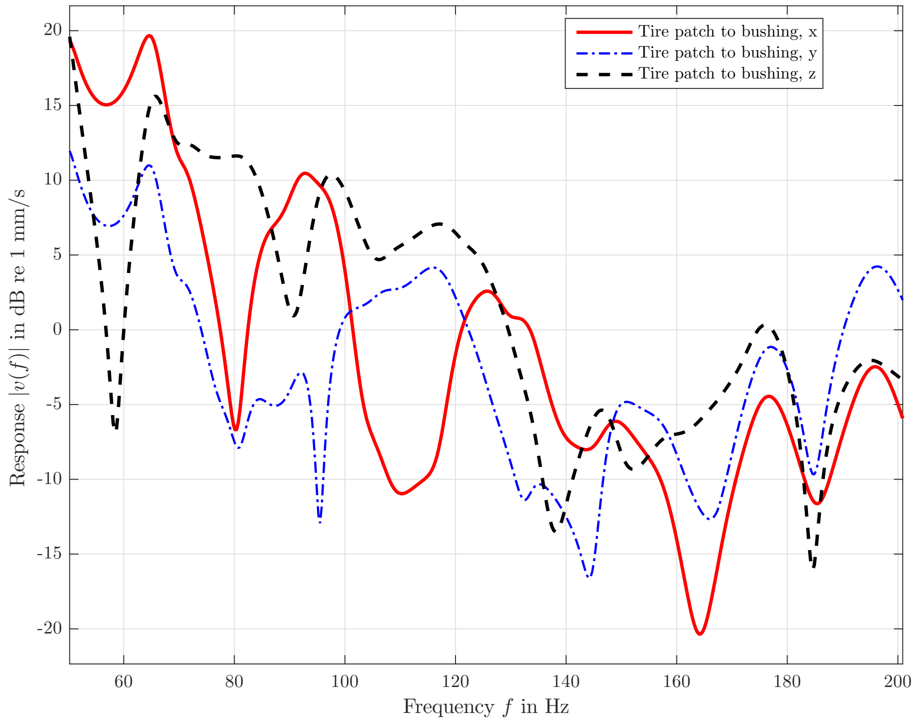

Figure A.9: Translational response at the bushing, 5th harmonic

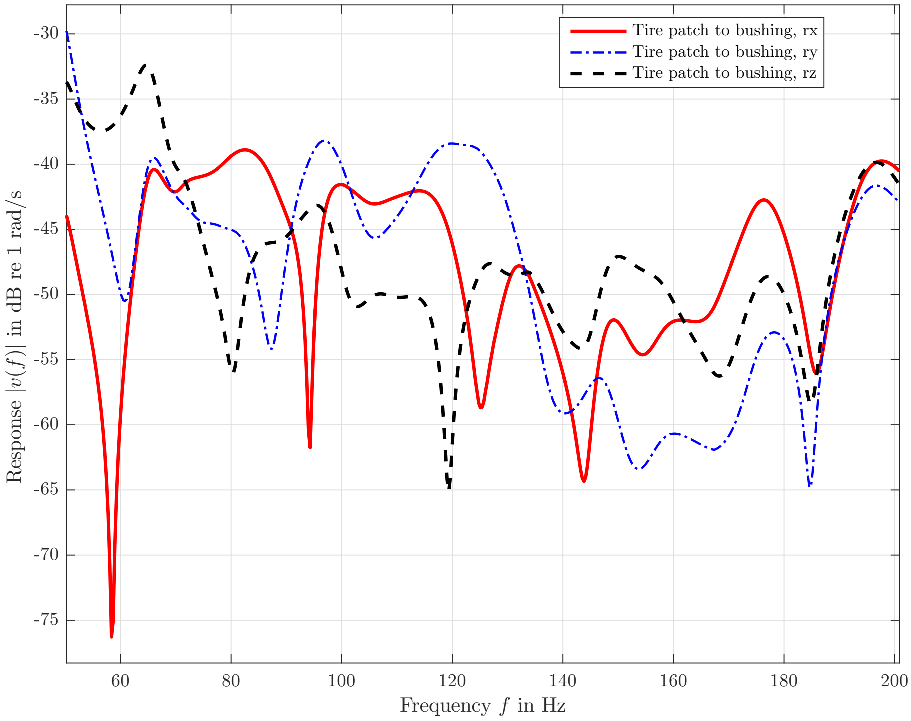

Figure A.10: Rotational response at the bushing, 5th harmonic

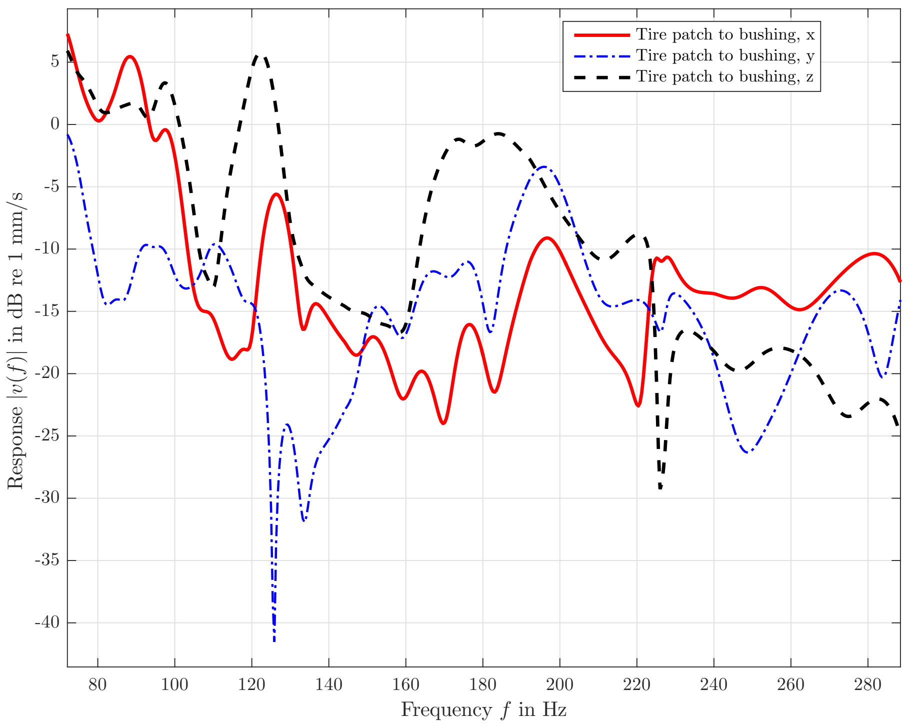

Figure A.11: Translational response at the bushing, 6th harmonic

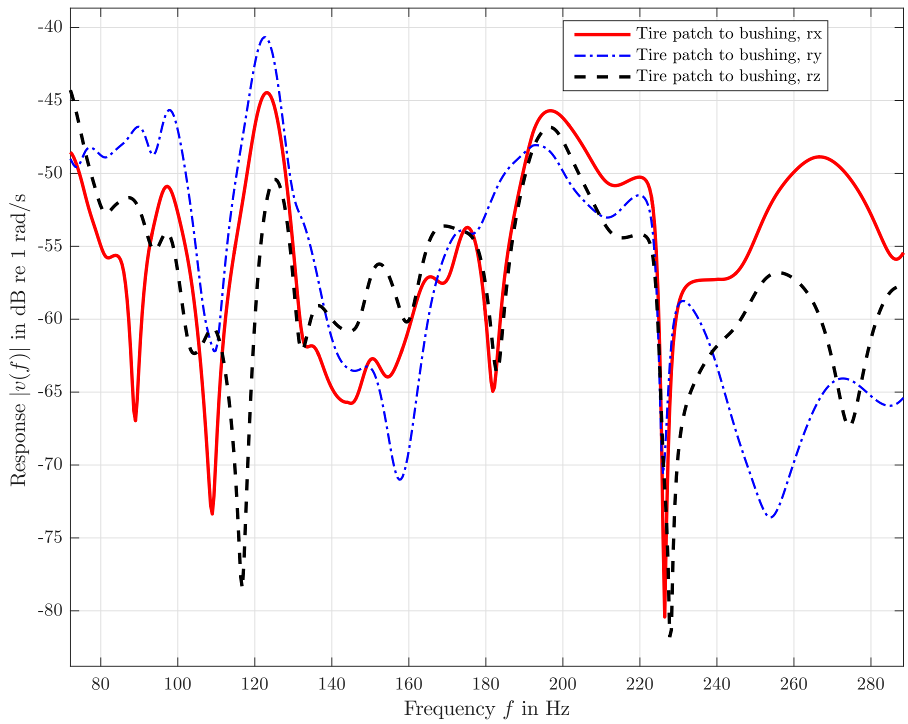

Figure A.12: Rotational response at the bushing, 6th harmonic

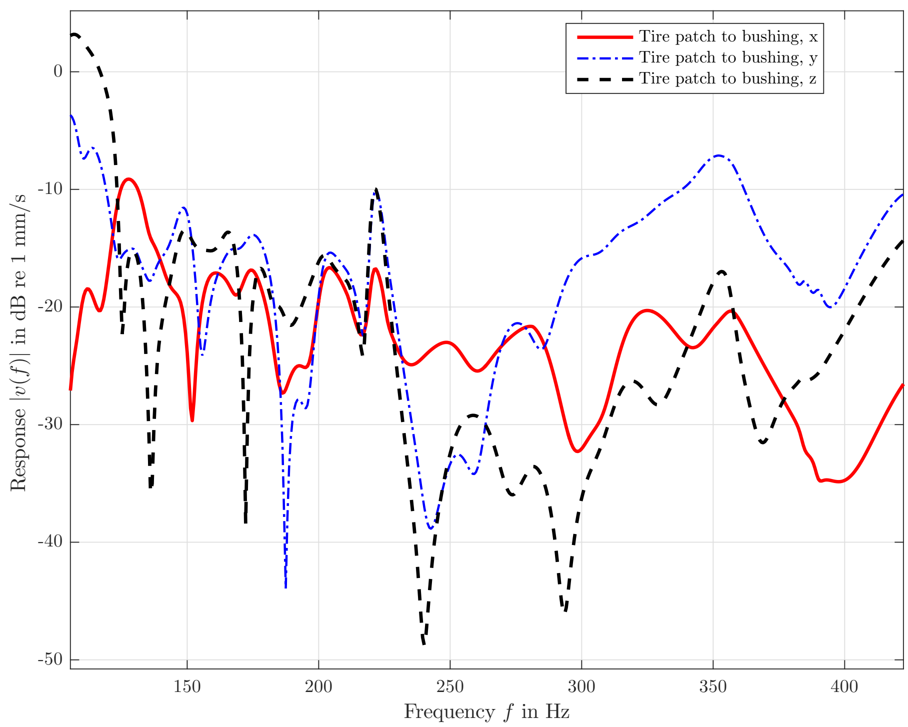

Figure A.13: Translational response at the bushing, 7th harmonic

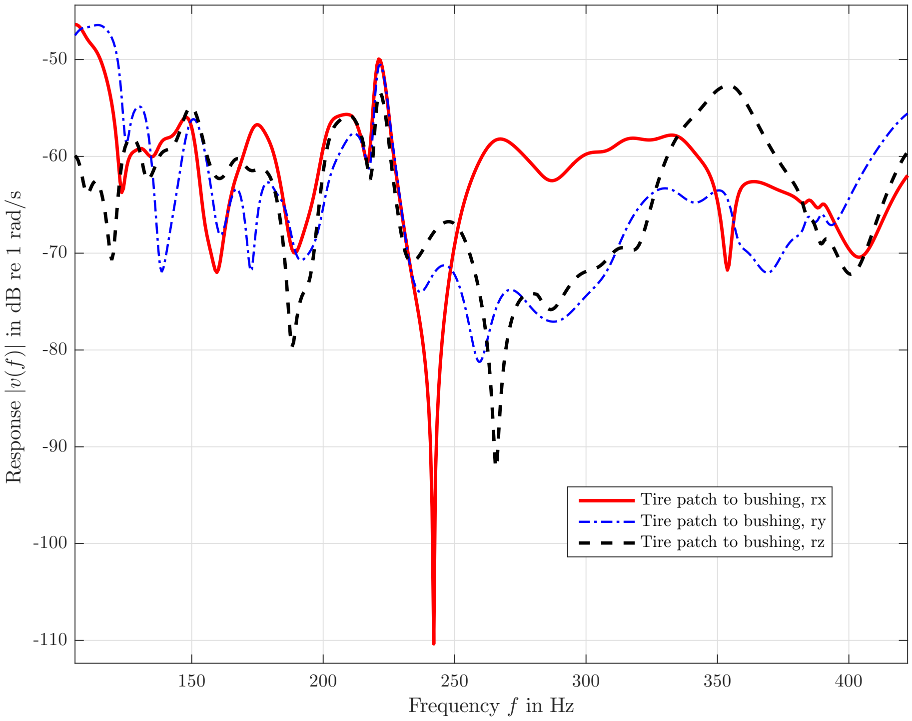

Figure A.14: Rotational response at the bushing, 7th harmonic

B

Sensitivity study - Modal truncation error introduced in the tire model

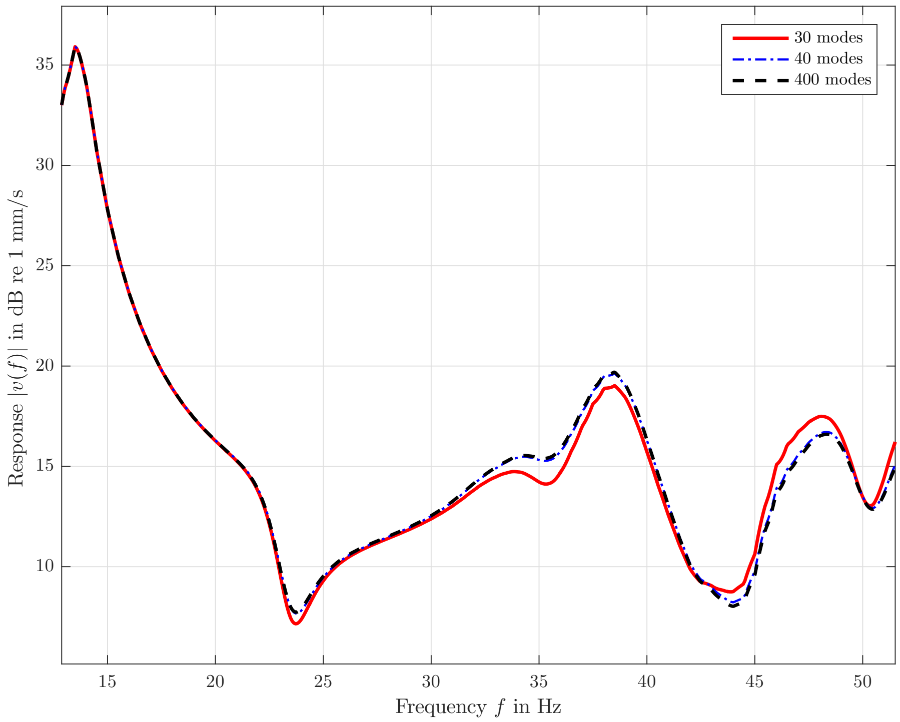

Figure B.1: Response in z direction at the bushing for different modes included, 1st harmonic

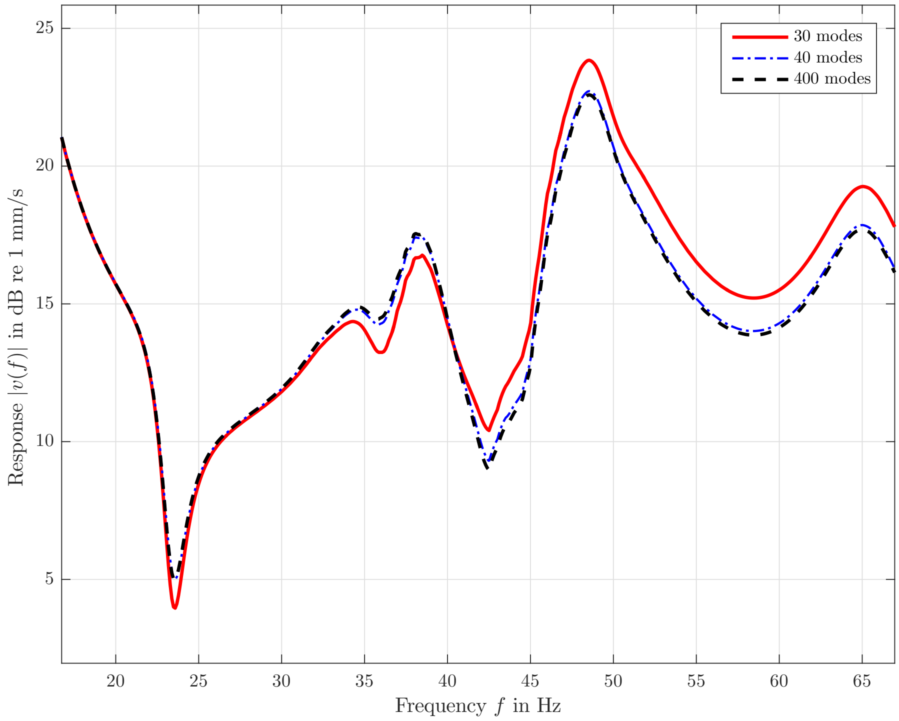

Figure B.2: Response in z direction at the bushing for different modes included, 2nd harmonic

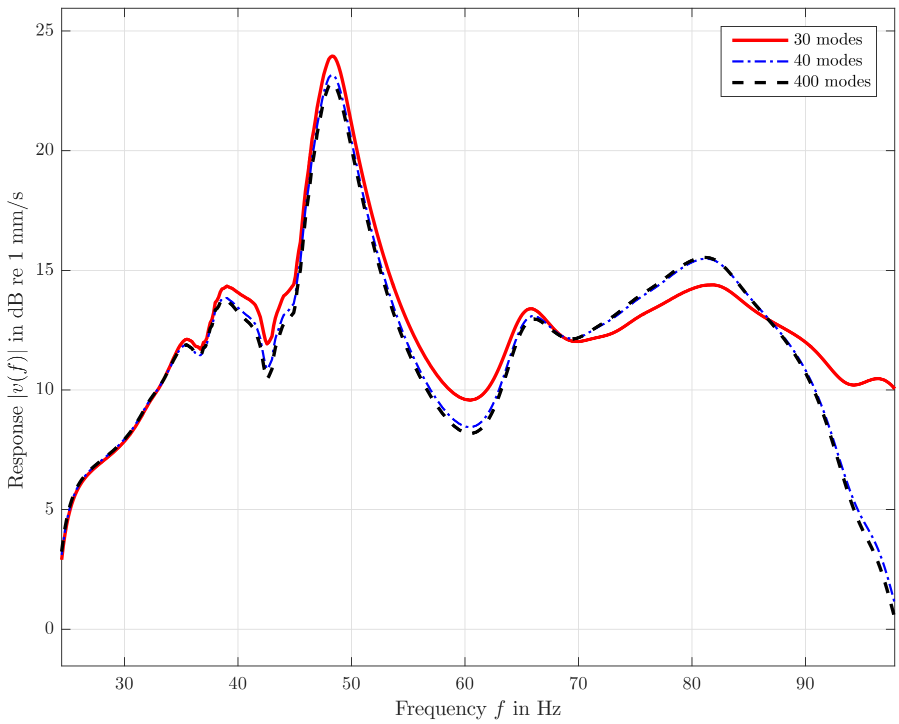

Figure B.3: Response in z direction at the bushing for different modes included, 3rd harmonic

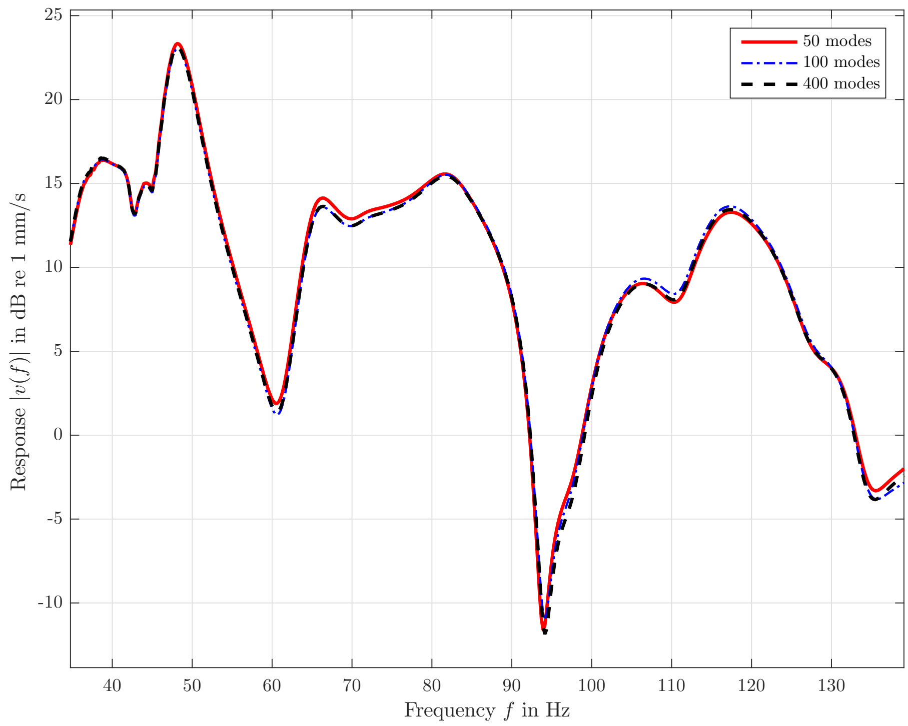

Figure B.4: Response in z direction at the bushing for different modes included, 4th harmonic

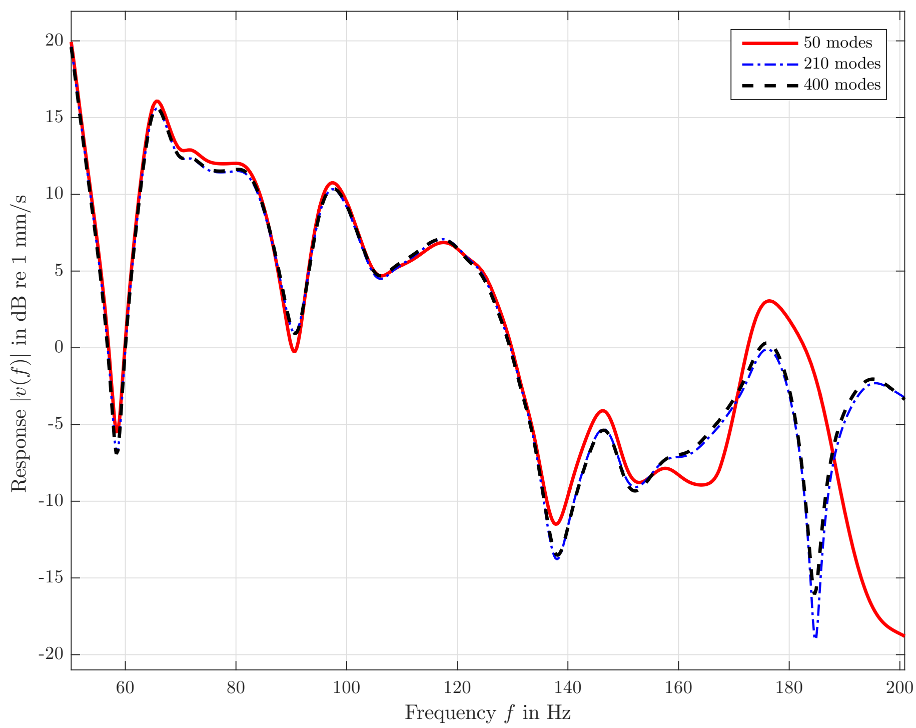

Figure B.5: Response in z direction at the bushing for different modes included, 5th harmonic

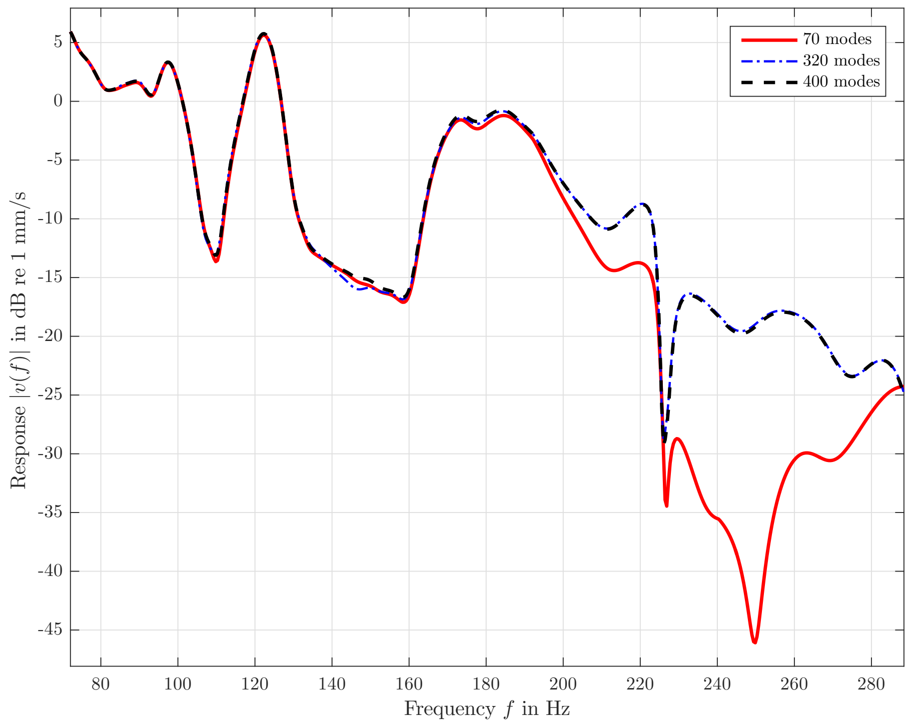

Figure B.6: Response in z direction at the bushing for different modes included, 6th harmonic

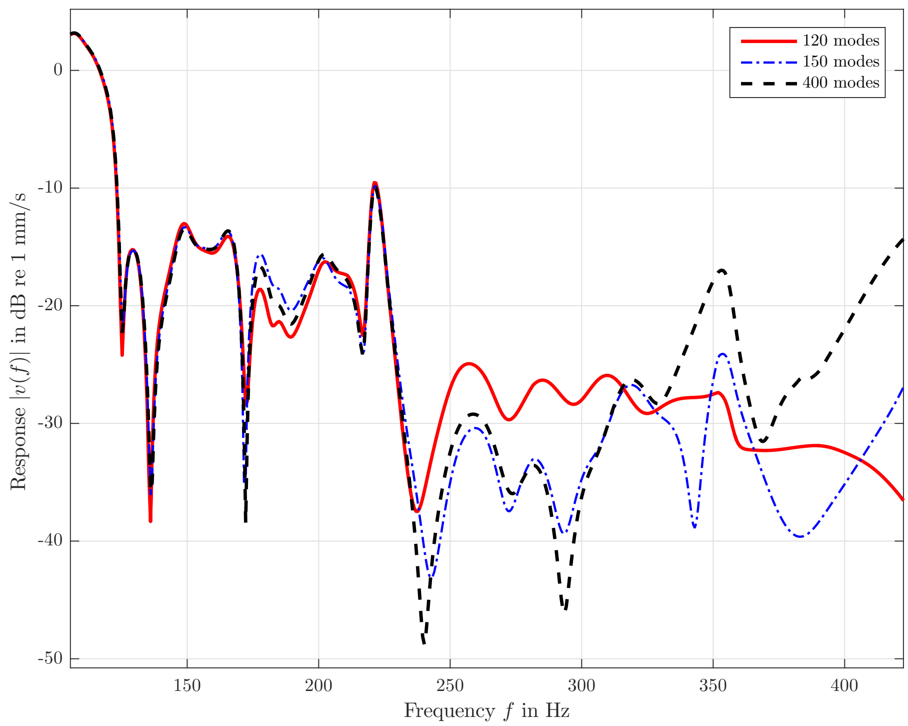

Figure B.7: Response in z direction at the bushing for different modes included, 7th harmonic

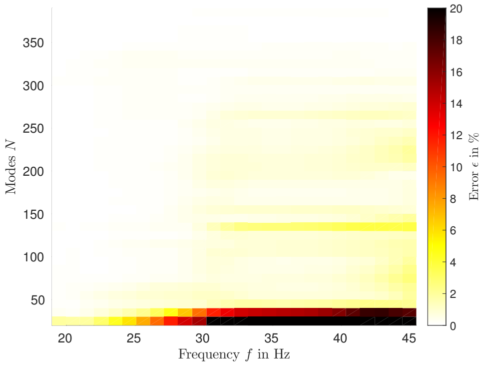

(a) 1st harmonic

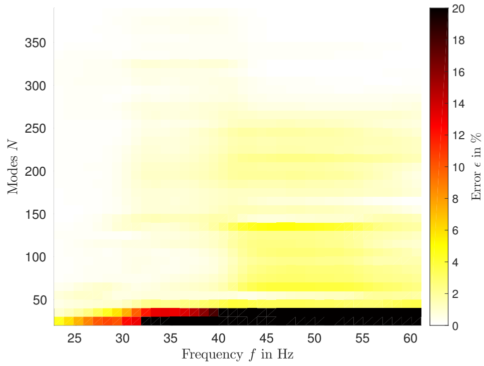

(b) 2nd harmonic

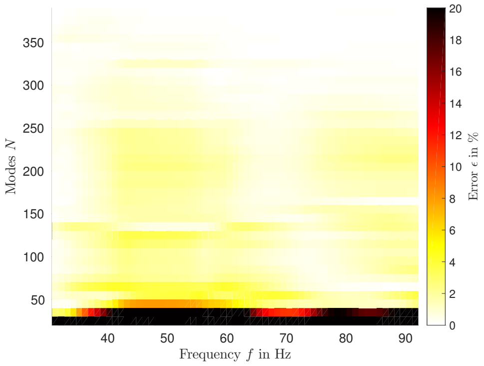

(c) 3rd harmonic

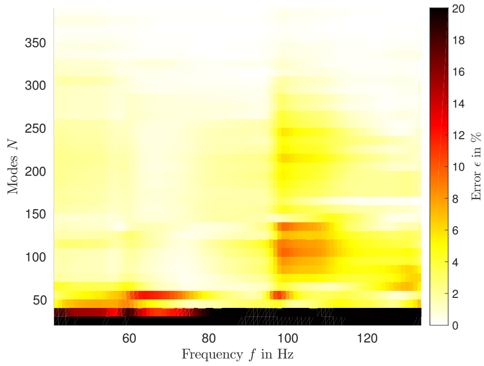

(d) 4th harmonic

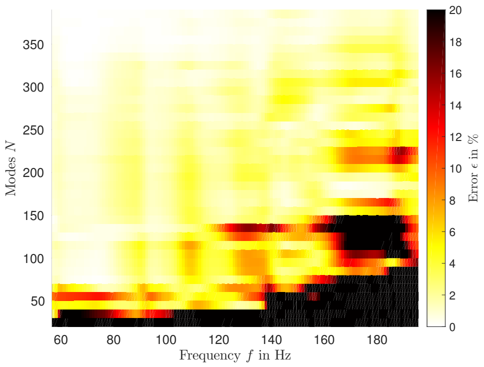

(e) 5th harmonic

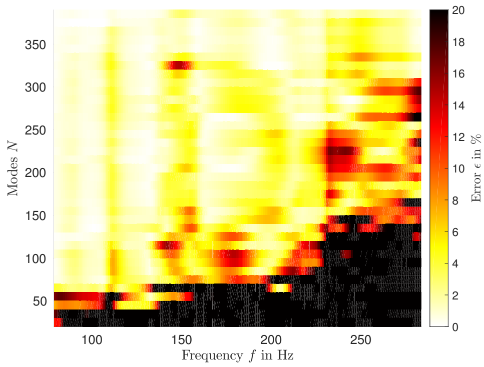

(f) 6th harmonic

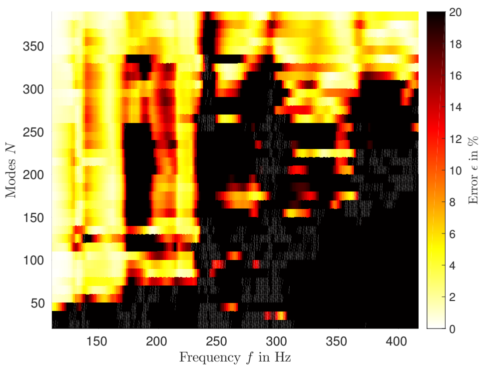

(g) 7th harmonic

Figure B.8: Truncation error for z DOF in $\mathbf{v}^*_{\mathrm{ea}}$

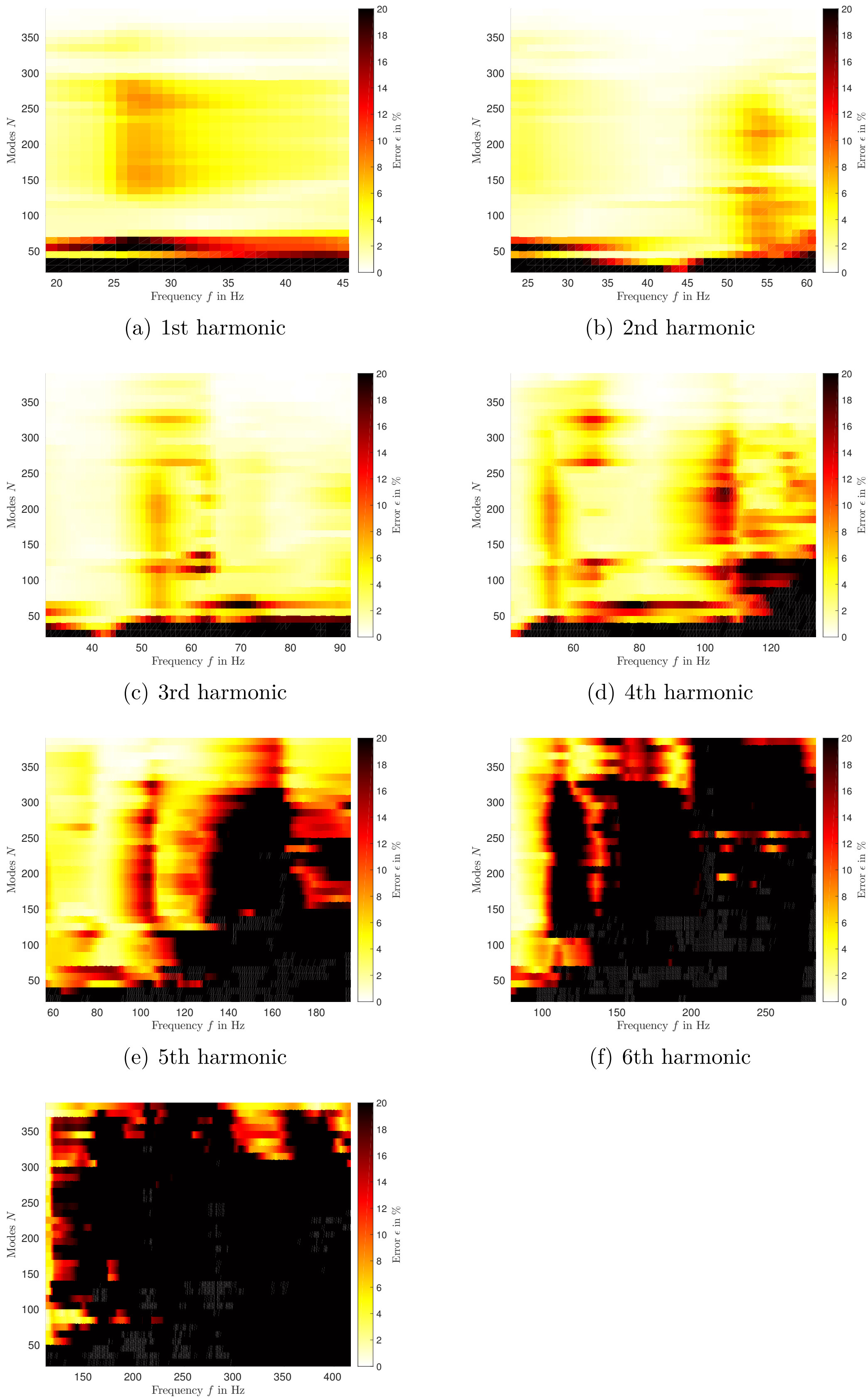

(a) 1st harmonic

(b) 2nd harmonic

(c) 3rd harmonic

(d) 4th harmonic

(e) 5th harmonic

(f) 6th harmonic

(g) 7th harmonic

Figure B.9: Maximum truncation error in $\mathbf{Y}^{\mathrm{A}}_{\mathrm{ja}}\mathbf{F}^{\mathrm{A}}_{\mathrm{a}}$, tire uncoupled

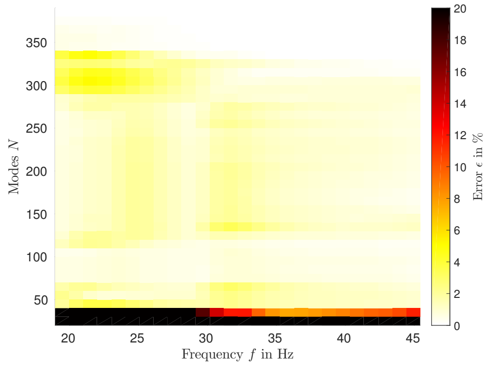

(a) 1st harmonic

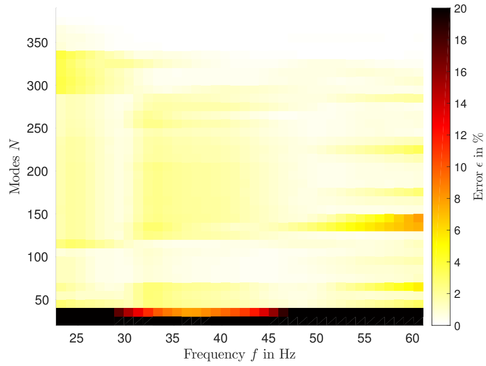

(b) 2nd harmonic

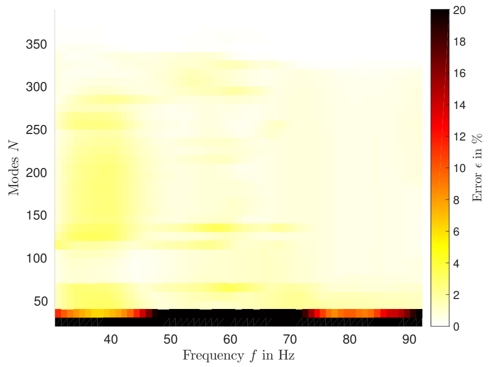

(c) 3rd harmonic

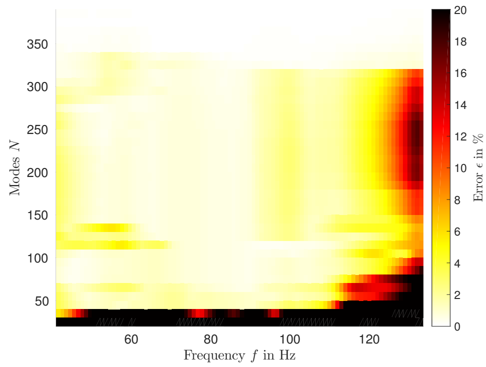

(d) 4th harmonic

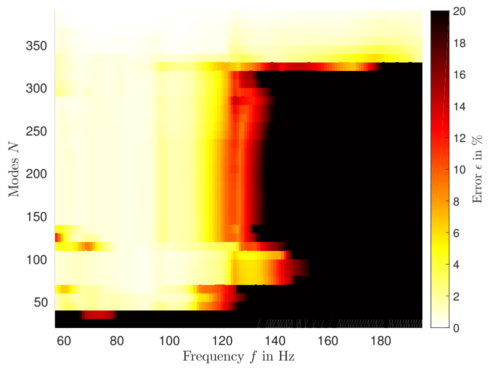

(e) 5th harmonic

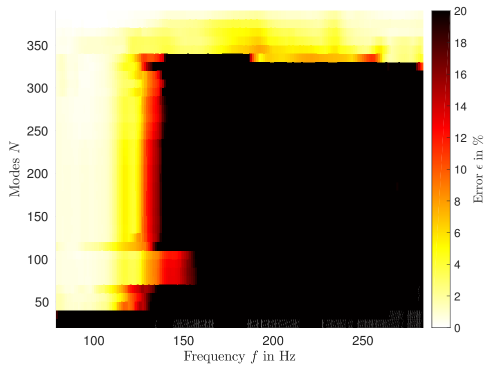

(f) 6th harmonic

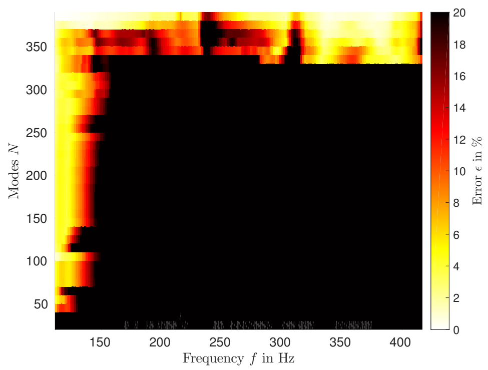

(g) 7th harmonic

Figure B.10: Maximum truncation error in $\mathbf{Y}_{\mathrm{jj}}^{\mathrm{A}}$, tire uncoupled

C

Sensitivity study - Random noise

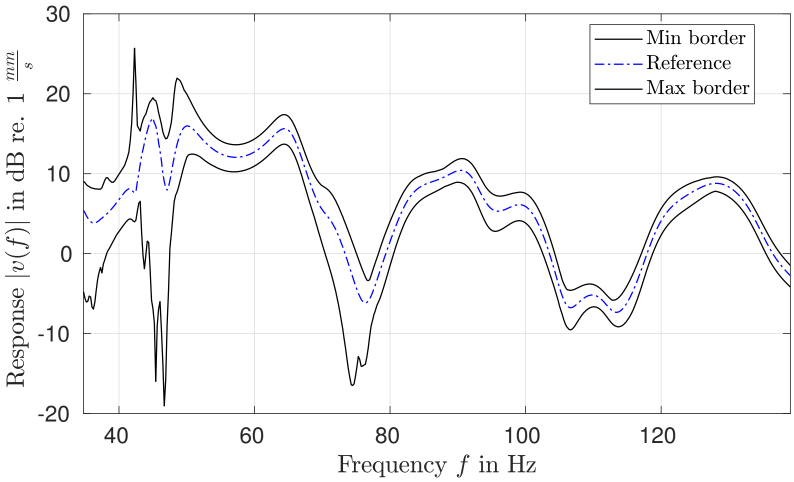

Figure C.1: Response in z direciton at the bushing, 4th harmonic, noise introduced to tire model, 2000 calculation rounds.

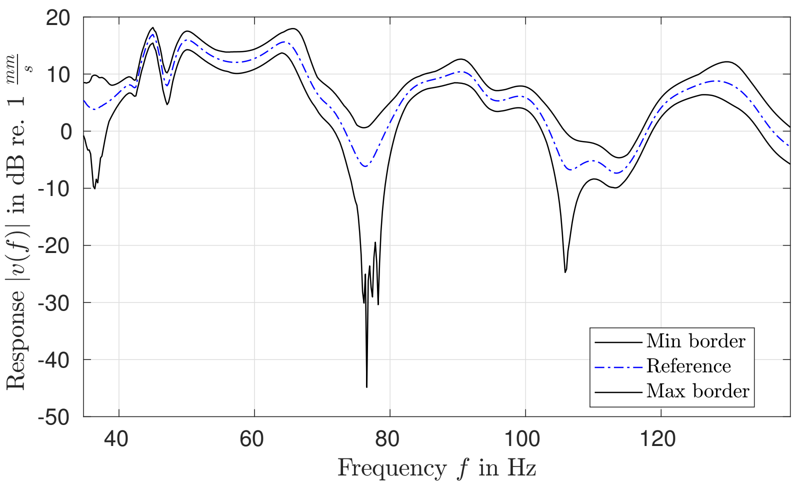

Figure C.2: Response in z direction at the bushing, 4th harmonic, noise introduce to chassis model, 2000 calculations rounds.